Title	Development and application of parameterization techniques for next-generation Southern Ocean oceanographic observations
Author(s)	潘, 先亮
Degree Grantor	北海道大学
Degree Name	博士(環境科学)
Dissertation Number	甲第15261号
Issue Date	2023-03-23
DOI	https://doi.org/10.14943/doctoral.k15261
Doc URL	https://hdl.handle.net/2115/89474
Type	doctoral thesis
File Information	Pan_Xianliang.pdf

学位論文

Development and application of parameterization techniques for next-generation Southern Ocean oceanographic observations

(次世代南大洋海洋観測に対するパラメタリゼーション技術の開発と展開)

Division of Earth System Science,

Graduate School of Environmental Science,

Hokkaido University

Xianliang Pan

潘　先亮

February 2023

Abstract

The carbon and nutrient cycles in the Southern Ocean (SO) have a great potential for controlling global climate and ecosystem changes. However, the spatiotemporal sparseness of observational data due to severe meteorological and oceanographic conditions in the seasonal sea ice area of the SO has led to significant uncertainties in the studies of the ocean dynamics in the SO. To quantitatively clarify carbon and nutrient cycles and their variations in the entire SO, it is essential to acquire the spatiotemporal high-resolution data for these materials.

Here I have been working on the development of high-precision parameterizations with linear regression and neural network model for carbon and nutrient over the SO and have demonstrated their usefulness for the spatiotemporal complementation of observational data. For example, I developed parameterizations for nitrate, dissolved inorganic carbon, and pH over the SO, applying these parameterizations to the SO to determine the oceanic external nitrogen uptake and anthropogenic pH variability there during the period 1990s-2010s. Furthermore, I have attempted to estimate the seawater freshening around the Antarctica and found a rapid freshwater input during the early 21st century by constructing parameterizations of DIC in the open SO and the coastal SO. The parameterization technique will dramatically advance the detailed understanding of the ocean dynamics in the SO, and the application of this technique to the sensor-equipped observation instruments, such as Argo float and CTD, must be promising in the future

studies of the ocean dynamics in the SO.

My study aims to promote future studies of spatiotemporal high-resolution ocean dynamics in the SO, and sets the following subjects:

1. To estimate the anthropogenic materials uptake over the SO.
2. To estimate the glacier-derived seawater freshening around Antarctica.
3. To estimate the carbon biological production over the SO.
4. To estimate the decoupling between silica and nitrogen from SO to a global scale.

Subject 1: To comprehend the dynamics of oceanic external nitrogen (N_{ex}) in the SO, I developed a new method to assess the change in the oceanic uptake of N_{ex} (ΔN_{ex}) in the entire SO. I obtained the spatiotemporal distribution of ΔN_{ex} in the SO by applying this method to a high-resolution grid data constructed using ship-based observations. During the 1990s to the 2010s, N_{ex} increased significantly by 67±1 Tg-N year^{-1} in the SO. By comparing this value with the rate of N_{ex} deposition to the ocean, the SO has received ~ 70% of N_{ex} deposition to the global ocean, indicating that it is the largest uptake region of anthropogenic nitrogen into the ocean interior.

Subject 2: I developed a method that first provided us with an expansive understanding of glacier-derived freshening progress over the SO coastal regions (SOc). Applying this method to the observational data in the SOc from 1926 to 2016, revealed that the rate of glacier-derived freshwater input reached a maximum of 268 ± 134 Gt year^{-1} during the early 21st century. My results indicate that during the same period, glacier melting accounted for 63%, 28%, and 92% of the total freshening occurred in the Atlantic, Indian, and Pacific sectors of the SOc, respectively. This suggests that the ice shelf basal melt in West Antarctica and the Antarctic Peninsula plays a dominant role in the freshening of the surrounding seas.

Subject 3: My new idea of combining neural network parameterization and Biogeochemical Argo floats (BGC-Argo) allowed me to obtain the detailed spatiotemporal distribution of downward export (DE) from the surface ocean to the ocean interior ocean biological production in the modern SO, indicating the total DE of DIC, N and Si of 340.9 ± 22.2 Tmol $year^{-1}$ (Tmol = 10^{12} mol), 39.7 ± 2.6 Tmol $year^{-1}$ and 79.8 ± 5.2 Tmol $year^{-1}$, which accounts for about 33%, 26% and 62% of the global ocean export given by the previous studies, respectively. Furthermore, the DE of DIC and N in the SO was significantly decreasing at a rate of 0.8% and 2.5% per year during 2007 to 2017, indicating that it may be contributing as positive feedback to the increase in atmospheric CO_2.

Subject 4: I here attempt to quantify the seasonal downward export fluxes of Si and N from surface as well as the upward resupply fluxes by using neural network parameterizations and BGC-Argo, and to directly estimate this decoupling between Si and N over the global surface ocean. I found a contrast downward export ratio of Si and N (Si/N) between the SO of 8:1 and the subarctic Atlantic of 0.1:1. IW-derived water masses with Si/N ≥ 1 are found in the major global upwelling regions, such as the equatorial Pacific and the subarctic Pacific. Lower Si/N in these regions (~2:1) than that in the SO is probably due to the deficiency of Si or the supply of terrestrial-origin iron. The imbalance between the downward export and the upward resupply allows us to identify the main regions of Si removal from the surface that result in the meridional descending gradient of Si in the global ocean.

Contents

Chapter 1 General introduction

1.1 The Southern Ocean and the global climate

The Southern Ocean (SO, defined as the ocean south of 30°S in this study) plays a key role in influencing the Earth's climate as one of the starting points of the meridional ocean circulation (MOC) and as an important entrance and exit point for heat as well as chemical materials[1]. The SO is the only ocean in the world that circles the Earth in the east-west direction. The strong westerly winds prevail in the SO, which leads to the existence of the Antarctic Circumpolar Current (ACC) that surrounds the SO. Due to the existence of the ACC, warm currents transported southward from the equator cannot enter the SO, making the sea water there at a very low temperature all year round.

On the other hand, the SO surrounds the Antarctic continent, which is covered by the Antarctic ice sheet. As the seawater freezes, the salt in the seawater gradually precipitates out, which leads to the high salinity of the seawater around the Antarctic continent[2]. This low temperature and high salinity seawater gradually sinks into the deep ocean due to its increasing density, forming the Antarctic bottom water (AABW) and spreading northward. In addition, the deep water transported southward from the northern hemisphere meets the AABW when it enters the southern hemisphere, and because its density is lower than that of the AABW, this deep water gradually upwelling and flows clockwise around the SO, which is called circumpolar deep water (CDW). Part of the CDW that upwelling to the surface flows southward and sinks to the bottom around the Antarctic continent again; the other part flows northward, and at about 50˚s, as its density is higher than that of the surrounding seawater again, it sinks to the ocean interior. the ocean and continues to flow northward, thus forming Antarctic intermediate water (AAIW) (Fig. 1.1).

The SO is also a region where vulnerable to the external processes. Since the industrial revolution, the input of anthropogenic CO_2 and nitrogen oxides to the oceans has gradually increased[3]. Models estimate that the oceans absorb about 25% of the anthropogenic CO_2, with the SO accounting for about 40%[4,5]. As the world's population increases, the demand for food is gradually increasing, which has led to the use of chemical fertilizers and the release of large amounts of nitrogen oxides in agricultural activities. The formation of the Subantarctic mode water (SAMW) redistributes this anthropogenic CO_2 and anthropogenic nitrogen to the rest of global ocean[6,7], which leads to the acidification of the global ocean and has a significant impact on marine ecosystems. Bottom waters transport this absorbed anthropogenic materials to the deep ocean, creating long-term storage for them[7].

The Antarctic ice sheet is melting at an accelerated rate due to the progress of global warming[8]. The common perception is that rising temperatures are causing the melting of the Antarctic ice sheet[9]. But the ocean also plays a key role in the melting of the ice sheet[10-12]. As mentioned earlier, during the movement of water masses in the SO, warmer CDW rises in the SO and some of it enters the Antarctic shelf and mixes with the seawater there to form modified CDW (mCDW). The warm mCDW flows with the topography to the base of the Antarctic ice sheet, thus causing the basal Antarctic ice sheet to melt[11,12]. This process is thought to cause the loss of more than half of the mass of the Antarctic ice sheet and the release of large amounts of freshwater into the Antarctic coastal waters, leading to enhanced stratification of seawater and even weakening of the MOC[10].

The SO, as the largest HNLC sea area in the world, has a high potential for biological production[2]. It is now widely believed that the biological production in the SO is limited by the lack of iron[13]. Biological production processes in the SO surface layer also act as a sink for increased anthropogenic CO_2 in the atmosphere[2]. Diatoms, which are abundant in the surface SO, can also fix atmospheric CO_2 into the ocean interior through their biological production as well as their sedimentation[2]. The last ice age decline in global atmospheric CO_2 concentration of about 80 ppm is thought to have been caused by enhanced global marine biological production[2]. In summary, the SO plays an important role in controlling atmospheric CO_2 levels as well as global marine ecology and global climate. The SO is vulnerable to anthropogenic sources and to the melting of the Antarctic ice sheet[4,5,10,14,15]. These make understanding the mechanisms and processes of biological production in the SO one of the most important topics today.

1.2 Challenges in in-situ observation in the SO

Observational data are essential if we are to understand the material cycle changes and biological production in the SO. Currently, data observations in the SO are made in several ways. The first is based on in situ observations from survey vessels[11,16]. Because the SO is far from the human-inhabited continent and its harsh climate, in situ observations are often very restricted[17], which makes the data obtained by this method often have great spatial as well as temporal inhomogeneity. Second, the observation technique based on remote sensing satellites[10,18]. Through satellites, we can obtain a wide and continuous data on the physical and biological parameters of the ocean surface. However, this approach can only observe the surface of the ocean and cannot help us to obtain information about the interior of the ocean. Third, the observation method based on the automatic observation instrument (Argo float), which is an observation instrument that can automatically measure various parameters in the ocean at 10-day intervals for a maximum of six consecutive years[19,20]. Currently, the main parameters that can be observed are water pressure, water temperature, salinity, and partially dissolved oxygen, nitrate, and chlorophyll. However, the number of Argo float that can observe nitrate and chlorophyll is very limited due to the different sensors they carry. This limits to some extent the usefulness of this method. Recent studies have indirectly estimated the biological production in the ocean by combining dissolved oxygen measured by Argo float with chemical stoichiometry ratios[21]. However, the variability of such chemical stoichiometry ratios has brought some influence on these estimations.

1.3 Parameterization technique for the next generation SO observation

To overcome this problem, I proposed a parameterization technique for use in the oceanic material cycle[22,23]. The parameterization technique is a method to construct an equation in a statistical model that relates nutrients and carbonates, for which the number of observed data is limited, to basic hydrological data, for which the number of data is relatively abundant. This parameterization technique has the following two main features. The first is data expansion. Within the spatiotemporal scope of parameterization, the concentration of a target substance can be predicted as long as basic hydraulic data are available.

Another thing that parameterization techniques can do is to capture the effects of external ocean processes on the ocean[7,24]. In the parameterization of a substance A, there is a constant value of A_{ex}, the import of the substance from outside the ocean, while A_{in}, the concentration of A originally present in the ocean, is controlled by physical and biological processes in the ocean and can be expressed through changes in hydrographic parameters. Based on this property, parameterization can be used to separate internal and external ocean processes.

There are two main types of statistical models used in this study when constructing parameterizations. First, the multiple linear regression model (MLR), which uses the least squares method to construct a linear prediction equation between each parameter and a substance A[22,23]. Its advantage is twofold: it is easy to evaluate the appropriateness of the chosen parameters, and it is easy to determine the relationship between the parameters and the output values. However, MLR has the disadvantage of introducing large errors when dealing with nonlinear relationships, since there are no absolute linear relationships in the real ocean.

To solve this problem, Neural Network model (NN) comes into play[25-27]. In simple terms, the NN model is a model that puts one or several hidden layers between the input parameters and the output and expresses the nonlinear relationship between the parameters and the output through a nonlinear activation function. However, the prediction equation obtained by the NN model is difficult to display as easily as the MLR model, so the relationship between the parameters and output values is relatively difficult to understand. In this study, I use a hybrid of MLR and NN.

This study aims to use the features of this parameterization technique to elucidate the relationship between the SO and climate change, and to achieve the following three goals: First, to estimate the amount of uptake into the external material in the SO. Second, to assess the impact of freshwater inflows from the melting of the Antarctic ice sheet on the Antarctic marginal seas. Third, to elucidate the relationship between different material cycles due to biological production in the ocean surface layer.

Chapter 2 Estimation of the anthropogenic materials uptake over the SO

2.1 External nitrogen (N_{ex}) and the ocean

The reactive nitrogen (N_r, i.e. NO_x, NH_y, and dissolved organic nitrogen) input to the open ocean has increased significantly since 1860, especially in the last two decades[28]. Such consistent increase in the reactive nitrogen input could lead to changes in the ocean nitrogen and carbon cycles apart from affecting the marine biological productivity. Anthropogenic nitrogen released by human activities such as industrial nitrogen fixation and combustion of fossil fuel has contributed the most towards this increase. Nearly 70% of oceanic external nitrogen (N_{ex}), which is defined as the input of fluvial and atmospheric N_r in this study, is anthropogenic N_r[29]. Considering that the turnover time of natural N_r in the ocean is approximately 3,000 years[30], the change in N_{ex} (ΔN_{ex}) on the decadal timescale can closely reflect the change in the anthropogenic uptake in the ocean. The distribution of ΔN_{ex} in the surface ocean has been reported by several studies[28,31,32]. However, the spatiotemporal distribution of ΔN_{ex} in the ocean interior is yet to be revealed clearly; consequently, we lack the comprehension of the amount and storage of anthropogenic nitrogen received by the ocean as well as the variation in the oceanic uptake of anthropogenic nitrogen with time.

The SO covers approximately 30% of the global ocean surface area, and it is an important pathway that drives external influences such as anthropogenic impact into the global ocean interior owing to the strong movement of water masses (e.g. meridional overturning circulation)[1]. The SO is also very susceptible to anthropogenic materials because much of the sea surface water flowing into the SO touches the borders of several developing countries such as China, India, and South-East Asian countries. Therefore, clarifying the ocean dynamics of N_{ex} in the SO is crucial for gaining a deep understanding of the human impact on the ocean.

2.2 Limitations of the previous studies

However, there are two challenges in exploring the presence of N_{ex} in the SO. One is the difficulty in acquiring ocean observations owing to the severe environmental condition of the SO. Ship-based observational data of the SO are considerably deficient compared with those of other oceans in the Northern Hemisphere. Recent studies on climate change in the SO have mainly focused on multiple repeated ship-based observations along the same lines every decade; the data collected is sparse owing to the difficulty in collecting data from the entire SO[33,34]. The other challenge is difficulty in separating N_{ex} from the internal nitrogen (recycled nitrogen, N_{in}). Kim et al. (2014) reported the impact of anthropogenic nitrogen on the western North Pacific using N^* and the water mass age[32]. Their approach could not remove the effect of nitrogen fixation and denitrification; consequently, it was difficult to estimate the anthropogenic nitrogen in the ocean accurately and apply it to the global ocean.

Recently, a new method capable of estimating the change in anthropogenic CO_2 impact on the ocean interior across decadal time intervals using parameterization techniques was proposed[35], which makes it possible to overcome the two abovementioned difficulties related to the SO. Here, I have extended this method to N_{ex} and proposed a new concept for obtaining the spatiotemporal distribution of ΔN_{ex} in the entire SO.

2.3 Separation of N_{ex} with the parameterization technique

Observational hydrographic data used in this study

All the hydrographic observational data for nitrate (N), dissolved oxygen (DO), temperature (T), salinity (S), and pressure (Pr) were sourced from GLODAP v2 and CCHDO (https://cchdo.ucsd.edu/)[36,37]. The quality flags of the World Ocean Circulation Experiment (WOCE) were used to check the quality of these data. In this study, I only used data with a quality flag of 2 (i.e. data value is acceptable). I used 65,257 data from 69 cruises from 2000 to 2016 for constructing the parameterization of N_p, and 135,458 data from 101 cruises from 1990 to 2017 for estimating ΔN_{ex} (Fig. 2.1).

Parameterization of reactive nitrogen

I use nitrate (N) to represent N_r because nitrate accounts for more than 90% of N_r and it is the most stable dissolved form of nitrogen in the interior ocean (where most of ammonium and organic nitrogen are already conversed into N through nitrification or remineralization)[30]. The parameterization technique allows us to reconstruct the nitrate concentration spatiotemporally in the SO by using other hydrographic properties[22]. I used the hydrographic data for dissolved oxygen (DO), water temperature (T), salinity (S), and pressure (Pr) along with the observed N

(N_{obs}) to perform the parameterization of N in the SO. All the data I used were sourced from Global Ocean Data Analysis Project version 2 (GLODAP v2), Climate and Ocean: Variability, Predictability and Change (CLIVAR), and Carbon Hydrographic Data Office (CCHDO) [36,37]. By giving several data constraints in obtaining an optimal parameterization (Table 2.1), I obtained the predicted concentration of N (N_p) in the SO, as follows:

$$N_p = 394.3 - 9.208\times10^{-2}\cdot DO - 1.534\cdot T - 9.862\cdot S + 2.029\times10^{-4}\cdot Pr \qquad (2.1)$$

(Number of data points (n) = 65,257; Coefficient of determination (R^2) = 0.97;

Root-mean-square error (RMSE) = 0.80 μmol kg^{-1})

Here, I used MLR to construct the parameterization because I focus on the ocean interior and MLR is sufficient for me to achieve this. More details of our parameterization method are presented in Figs. 2.2, 2.3 and Table 2.2. Several statistical tests and an independent dataset were used to confirm the accuracy of our parameterization method. Additionally, I compared the spatial distributions of N_{obs} and N_p in the SO of 30°S south at surface, 500m, 1,500m, 3,000m and 5,000m (Fig. 2.4); consequently, the distribution of N_p was in good agreement with that of N_{obs}, demonstrating that our parameterization has high accuracy and applicability to the reconstruction of N in the entire SO.

Constraints and examination of parameterization of N_p

Data constraints for enhancing the accuracy of our parameterization are shown in Table 2.1. Here, I defined the Southern Ocean (SO) as the region south of 30 °S. My study mainly focused on atmospheric nitrogen deposition in the open ocean because the fluvial input process is very complicated[31]. In addition, I defined the regions with bottom depths of less than 1500 m as the continental shelf and did not use these data in my parameterization. Considering that the lower limit of the current detection accuracy of nitrate is ~ 0.2 μmol kg^{-1}, I only used N_{obs} data higher than this value. Although I used DO as a parameter to reflect the biological processes, DO in the surface mixed layer is directly affected by rapid air-sea exchange, which will have a significant impact on the regression; therefore, the observational data corresponding to the surface mixed layer were also removed. I defined the surface mixed layer as the water depth within a temperature difference of 0.5 ºC from the surface temperature ($\Delta T \leq 0.5$ ºC)[38]. In my study, the surface mixed layer had an average depth of ~60m in the region of 30˚S south during 2000 to 2016, along with a few values deeper than 100m encircled the Antarctic coastal region. The complex water mass composition of the SO posed great challenges to the parameterization construction. Through a series of comparative analyses, I found that the North Atlantic Deep Water (NADW) in the Northern Hemisphere and the Subantarctic Surface Water (SASW) north of 45 °S showed significantly different characteristics of T and S when compared with the water masses formed in the Antarctic[39]. To improve the accuracy of the regression, these two water masses were also not considered for constructing the parameterization.

The *F*-test is generally employed to determine the usefulness of each parameter in a multiple linear regression. A parameter is considered significant if its *F* value is greater than 2.4. By constructing the predicted concentration of N (N_p) in the SO (Fig. 2.2), T and S have *F* values of 1,426,953 and 213,532, respectively (Table 2.2). The increase in T and S results in decrease in N_p in Equation (2.1), which is consistent with the relationship among N, T and S in seawater[40], indicating that T and S are significant for our regression. DO (O_2), which has an *F* value of 903,917, also shows a negative correlation with N, reflecting the formation and consumption of N by primary production and respiration[41]. At depths below 400 m, the N/–O_2 ratios of remineralization appear to be constant at 16 ± 1/170 ± 10 (= 16/170 = 0.09) without considering denitrification (this ratio decreases to approximately 12 ± 2/170 ± 10 (= 12/170 = 0.07) when denitrification is considered)[42]. In this study, the N/–O_2 ratio was 0.09, indicating that denitrification was not included in our prediction. Standardized regression coefficients (β) were given to compare the contribution to N_p of each parameter. The closer the absolute value is to 1, the greater the contribution of the parameter is. Therefore, N_p was mainly controlled by T and DO in this study. I also investigated the presence of multicollinearity between variables by the variance inflation factor (VIF) (Table 2.2) and found that there was no multicollinearity in our parameterization. Generally, the variable is independent when the VIF is lower than 10.

I used independent datasets to confirm the accuracy of my parameterization. I chose WOCE lines P16 (2014), I08 (2007), and A12 (2014), which covered the three main sectors of the SO. Differences between N_{obs} and N_p for each sector (Fig. 2.3 and Table 2.3) showed good agreements in the Pacific sector and the Indian sector below the mixed layer. Deep water of the Atlantic Ocean (~2000 m) showed an obvious difference, which was probably caused by the movement of the anoxic water mass in the eastern tropical South Atlantic into the SO as North Atlantic Deep Water (NADW)[43]. The mean absolute deviations (MAD) of the differences in the Pacific, Indian, and Atlantic sectors were 0.37, 0.47, and 0.64 μmol kg^{-1}, respectively (Table 2.3). On comparing with the RMSE of our parameterization, these errors are acceptable in these three independent datasets.

Separation of N_{ex} from oceanic N

N_{obs} comprises an internal term (N_{in}) and an external term (N_{ex}) because the modern hydrographic data I used were already influenced by changes in the external matter. Heretofore, the separation of these two terms of N_{obs} was challenging. A method to estimate the variation in the external term of the observed ocean carbon species across different arbitrary years was proposed recently[35]. This method could be extended to distinguish N_{in} and N_{ex}. Fig. 2.5 and Equations (2.2-2.5) explain the method to estimate ΔN_{ex} based on the method proposed by Watanabe et al. (2018). N_{obs} always contains both the internal term (N_{in}) and the external term

(N_{ex}) (Equation (2.2)).

$$N_{obs} = N_{ex} + N_{in} \qquad (2.2)$$

Thus, N_p predicted from our parameterization was already influenced by the external term due to use of modern observational data for constructing our parameterization. I defined N_{ex} contained in N_p as the average for the years 2000–2016 (N_{ex2008}) because our parameterization is based on the observational data from 2000 to 2016 (Equation (2.3)).

$$N_p = N_{ex2008} + N_{in} \qquad (2.3)$$

Arranging Equation (2.2) in the expression for N_{ex} and substituting Equation (2.3) into Equation (2.2), N_{ex} for an arbitrary year can be expressed by N_{obs}, N_p, and N_{ex2008} (Equation (2.4)).

$$\begin{aligned} N_{ex} &= N_{obs} - N_{in} \\ &= N_{obs} - (N_p - N_{ex2008}) \qquad (2.4) \end{aligned}$$

The only unknown term now is N_{ex2008}, which is difficult to evaluate. Therefore, I made the key assumption that N_{ex2008} is constant with time, which makes it possible to cancel N_{ex2008} by calculating the time changes in the right and left sides of Equation (2.4) between two arbitrary different times (e.g. time 't1' and time 't2'). I can estimate the change in N_{ex} (ΔN_{ex}) by the following equation;

$$\begin{aligned}\Delta N_{ex} &= N_{ex(t2)} - N_{ex(t1)} \\ &= N_{obs(t2)} - N_{obs(t1)} - [(N_{p(t2)} - N_{p(t1)}) - (N_{ex2008} - N_{ex2008})] \\ &= \Delta N_{obs} - \Delta N_{p} \qquad (2.5)\end{aligned}$$

In summary, Equation (2.5) allows me to clarify ΔN_{ex} in the case where the observational data of N, DO, T, S, and Pr are repeatedly acquired for the same region. Here, N_{in} includes the nitrate originating from the processes associated with DO, T, S, and Pr in the ocean, such as biological nitrogen fixation and remineralization; N_{ex} represents only the effects of atmospheric deposition and riverine nitrogen.

Gridding of data

I used the weighted-average method provided by the Ocean Data View (ODV) software to interpolate our data onto a common grid (*c.f. Ocean Data View User's Guide Version 5.2.0, 16.6.1*)[44]. To achieve this, I first constructed grids over the SO. The resolution of the grid can be assigned as per the requirement. In this study, the two-dimensional (2D) grid of cross sections was assigned a resolution of 0.5° × 10 m (latitude × depth). The three-dimensional (3D) grid of the entire SO was constructed with a horizontal resolution of 1° × 1° (latitude × longitude) and 43 layers with vertical resolution having 50-m thickness from the surface to 500 m, 100-m thickness from 600 m to 1500 m, and 200-m thickness from 1700 m to the sea floor.

After construction of the grid over the SO, the ODV allows me to use a simple weighted-averaging scheme to calculate the property estimation at every grid point (Fig. 2.6; Equation (2.6)).

$$c_e = \sum_i \alpha_i \cdot d_i / \sum_i \alpha_i \qquad (2.6)$$

The weights of the data points α_i decrease exponentially with increasing distance between the data point and grid point: $\alpha_i = e^{-r}$, with $r = (\Delta x/L_x)^2 + (\Delta y/L_y)^2$, where Δx and Δy are the distances between the data point and grid point in the X and Y directions, respectively, and L_x and L_y are the separate averaging length-scales in the X and Y directions, respectively. The length scales of the X and Y directions in the 2D grid of the repeat-line estimation were both 50 permille. The length scale of the latitude and longitude in the 3D grid of the overall estimation was 50 permille, and the depth scale was 50 m.

2.4 Results and discussion

Through this method, I noticed that I could estimate ΔN_{ex} for a particular place by using

ΔN_p along with the data for ΔN_{obs} of that place for different years (Fig. 2.5(b)). In order to draw the cross sections of ΔN_{ex} in the SO, I selected three repeated observations from the 1990s to the 2010s along the lines SR03, I08, and A12 as the representative data for the Pacific, Indian, and Atlantic basins (Fig. 2.7). Considering the uncertainty of the N_p parameterization (RMSE = 0.80 μmol kg^{-1}) and the propagation of uncertainty from the calculation, ΔN_{ex} has an uncertainty of 1.13 μmol kg^{-1}, which means that ΔN_{ex} larger than this value must be significant. I estimated the meridional distributions of total water column inventory of ΔN_{ex} along each section (Fig. 2.8) by integrating ΔN_{ex} from the surface to the sea floor. Both SR03 and A12 have high water column inventories of ΔN_{ex} between the Antarctic Polar Front and the Subantarctic Front (50°S to 55°S), and both I08 and A12 near the Antarctic continent (60°S) also show high water column inventories of ΔN_{ex}. Considering the low primary production on the surface of the SO[45], the N_{ex} deposited on the surface must mainly enter the ocean interior through the formation of intermediate and deep waters and the penetration of surface water mass in the SO[46]. The Antarctic Circumpolar Current has become more active due to the strengthening of the westerly winds caused by the Southern Annular Mode, which has been increasing in the past two decades[47]. This phenomenon has strengthened the vertical exchanges of water masses in the SO, which supports the inference that there were remarkable increases in N_{ex} during the past 20 years in the Antarctic Intermediate Water and the Antarctic Bottom Water (Fig. 2.7).

Spatiotemporal distributions of ΔN_p and ΔN_{ex} over the Southern Ocean

Here, I used the same method as the previous sub-section to understand the distributions of ΔN_p (variation in internal N) and ΔN_{ex} over the entire SO. Considering the lack of observational data in the SO and the necessity for repeated observational data for the same location, I selected the observational data corresponding to the period 1990–1999 to represent the 1990s, 2000–2009 to represent the 2000s, and 2010–2017 to represent the 2010s. The data of each period were interpolated onto a common grid. I used a grid with horizontal resolution of 1° × 1°, and 43 vertical layers with 50-m thickness from the surface to 500 m, 100-m thickness from 600 m to 1,500 m, and 200-m thickness from 1,700 m to the sea floor.

Seasonal differences between different cruises may affect our estimation. Owing to the severe environment of the SO, most of my observed data were collected in the warm period. In order to verify whether there was a significant difference between the data for cold period (for convenience, I call it wintertime) and warm period (for convenience, I call it summertime), I used the data of wintertime (April to October) and summertime (January to March) and calculated the average N_{obs} and N_p at each depth for these two durations (Fig. 2.9). I found that above the depth of 500m the differences of both N_{obs} and N_p between the two seasons were ~ 3 µmol kg^{-1} as maximum; the corresponding differences at the depth of around 200 m became ~ 0.80 µmol kg^{-1}, which was equal to the RMSE of my parameterization. These two periods did not show an obvious difference below the depth of 500 m. Thus, I concluded that the seasonal difference in the observational data does not significantly affect the spatiotemporal distributions of ΔN_{ex} along with the total water column inventory.

The spatiotemporal distributions of ΔN_p and ΔN_{ex} are shown in Fig. 2.10 and Fig. 2.11(a), respectively. The spatiotemporal distribution of ΔN_p (Fig. 2.10) showed a large variation in the upper 1,000m water column and it revolved around the Antarctic continent along with the Antarctic Circumpolar Current in the different time periods. This phenomenon may be due to the continuing enhanced nutrient-rich Circumpolar Deep Water upwelling derived from the strengthening of the Southern Hemisphere westerlies in recent decades[48,49].Furthermore, ΔN_p became zero gradually with the increase of depth, implying that there is almost no nature-derived variation of N in the deeper water column. The distribution of ΔN_p showed no obvious difference between the Pacific, the Indian and the Atlantic sector of the SO.

In Fig. 2.11(a), the spatial distribution of ΔN_{ex} in the surface layer shows a tendency to diffuse along the continental coastal area to the open ocean (e.g. west coast of South America, southwest coast of South Africa, and south of Tasmania, Australia). The data for the continental shelf were removed to eliminate the uncertainty of river input in my parameterization construction based on the assumption that the riverine N_{ex} has little effect on the open ocean[28]. Jickells et al. (2017) found that approximately 75% of riverine N escapes beyond the shelf break and enters the open ocean, which may partly explain the significant rise in N_{ex} in the coastal region in my study[31].

In terms of the temporal distribution of ΔN_{ex}, the Indian sector has shown a remarkable growth in N_{ex} from the surface to the abyss during the period from the 2000s to the 2010s. By analyzing the spatiotemporal distribution, the reason for this can be attributed to the increase in anthropogenic nitrogen emission in developing countries such as India, China, and Southern Africa in the past decade[31,50,51]. According to the evaluation of the global meridional overturning circulation, the upwelling water in the surface North Pacific Ocean passes through the Strait of Malacca and reaches the northern Indian Ocean. Then, it goes south and flows into the Southern Ocean[1]. Meanwhile, the surface anthropogenic N is loaded on these waters along the coastal regions and brought to the Southern Ocean. Additionally, the enhancement of the Southern Annular Mode mentioned in the previous section can explain the increase in N_{ex} in the ocean interior.

I also estimated the total water column inventory of ΔN_{ex} from the surface to the sea floor in the SO (Fig. 2.11(b) and Table 2.4). During the 1990s to the 2010s, N_{ex} in the Pacific, Indian, and Atlantic sectors grew at the rate of 24 ± 1, 42 ± 1, and 0.02 ± 0 Tg-N year^{-1}, respectively, and that for the entire SO grew at the rate of 67 ± 1 Tg-N year^{-1}. Uncertainties were given by the standard error of gridding estimation (Table 2.5). The ΔN_{ex} in the Indian sector accounted for 63% of the increase in N_{ex} in the SO. I also found that the Atlantic Sector, which has the most active vertical circulation in the world, did not show a high ΔN_{ex}. This may be because of the following two reasons: (1) the deviation caused by the seasonal differences in the surface data (Fig. 2.9); (2) the inflow of the deposition of N_{ex} from the Atlantic sector into the Indian sector due to the Antarctic Circumpolar Current, which also explains why ΔN_{ex} in the Indian sector is extremely high. In the Pacific Ocean, I mainly observed the accumulation of ΔN_{ex} in the surface layer (Fig. 2.11) due to the upwelling area with relatively old water age in the deep Pacific[2]. These results can be considered reasonable compared with the previous model predictions [1,5].

In an early study[28], the deposition rate of N_{ex} to the global ocean was predicted as 67 ± 30 Tg-N $year^{-1}$ in the 2000s, the upper limit of which was 96 Tg-N $year^{-1}$ considering the potential impact of riverine input. By comparing the deposition rate with our data, I found that the SO had received 69% of the global oceanic N_{ex} input despite the SO covering only 29% of the global ocean surface area, which emphasizes the important role of the SO in integrating anthropogenic impacts in the global ocean.

Chapter 3 Ocean freshening around the Antarctica

3.1 Interactions between the Southern Ocean coastal regions and the Antarctic ice sheet

The Antarctic ice sheet accounts for ~70% of the freshwater on Earth, equivalent to ~60 m of the global sea-level height[8]. With ongoing global warming, the Antarctic ice sheet is losing its mass at a remarkable rate[8,52]. Continuous freshwater input derived from glacier melting would lead to ocean freshening and sea-level rise, which significantly influences the global climate system and long-term climate change[18,53]. In recent years, many studies have demonstrated that the basal melt of the Antarctic ice shelf could explain more than half of the Antarctic ice sheet mass loss[10,52,54,55]. Because of the emission of anthropogenic materials and the resulting positive trend of the Southern Annular Mode (SAM), the poleward shift of westerly winds and large-scale cyclonic eddies are bringing more and warmer modified Circumpolar Deep Water (mCDW) into Antarctic ice cavities[56-58], accelerating the basal melt of the Antarctic ice shelf and freshwater export to the ocean[10,52,55,59]. Several studies have found that Antarctic Bottom Water (AABW) has become warmer and fresher, and the formation of AABW has been reduced, which may eventually weaken the meridional overturning circulation of the global ocean[60-63]. Therefore, clarifying the impact of glacier melting on the progress of ocean freshening is important for understanding future climate change.

3.2 Current method for understanding ice sheet melting and ocean freshening

At present, the correct and expansive estimation of glacier-derived freshening remains bottlenecked due to the severe weather conditions of the Southern Ocean coastal regions (SOc) and limitations of observational techniques. Studies on Antarctic glacier melting and freshening occurring around Antarctica have been primarily based on the following methods. The first method is satellite-based observations[10,18,52,64]. Satellite remote sensing techniques are widely used to monitor Antarctic ice sheet mass balance and sea-level change. The basal melt rate of the Antarctic ice shelf can be directly estimated by subtracting the surface ice discharge from the total mass change of the Antarctic ice sheet. However, this method cannot estimate the effect of glacial melting on ocean freshening. Furthermore, only satellite data from 1979 onward are considered reliable because of the introduction of the multifrequency passive microwave technique[8]. The second method is numerical simulation based on the ocean-sea ice-ice shelf coupled model[57,65]. Numerical simulations can elucidate the physical processes between the ocean and the ice shelf, providing a comprehensive understanding of the current state of Antarctic ice shelf melting based on ice-ocean interactions. However, it is difficult for models to completely reconstruct the complex processes around Antarctica without sufficient physical and chemical parameter observations. The third type of method is *in-situ* observation. Long-term changes in seawater salinity can describe overall freshening which includes all freshwater sources[16,66-68]. Setting endmembers (e.g. $\delta^{18}O$ and salinity) to characterise each water component is a common way to distinguish different sources of freshwater input[55,69]. However, it is difficult to apply this method on a wide scale because the endmembers of water always change spatiotemporally.

To overcome these limitations and obtain a more comprehensive understanding of Antarctic glacier melting and SOc freshening, parameterization technique has come into our view recently [22,23,70,71]. On the one hand, high-accuracy observations of basic hydrographic parameters such as seawater temperature (T), salinity (S), dissolved oxygen (DO), and pressure (Pr) have been conducted for nearly 100 years over the SO with a relatively higher spatiotemporal resolution. Hence, the parameterization constructed by these basic hydrographic parameters enables us to obtain more available data on various chemicals in the SO[70]. On the other hand, if T, S, DO, and Pr are used in the parameterization function, a relationship reflecting the physical (e.g. water mass transportation) and biological (e.g. remineralization) processes can be obtained that relate to the chemical concentration in a specific region. This functional relationship does not change unless it is influenced by any external process. This suggests that for a parameterization of chemical A, the predicted concentration of A (A_{pre}) contains a component of the ocean internal processes (A_{in}) and a component of the average external process (A_{ex}) within the spatiotemporal range of the observed dataset used (equation 3.1). Based on the above two properties, parameterization is often applied to the estimation of external material input in the ocean[70,71].

$$A_{pre}(T, S, DO\ldots) = A_{in}(T, S, DO) + A_{ex} \qquad (3.1)$$

In this study, I propose a new method based on the interactions between Antarctic glacier and seawater and the oceanic parameterization technique (hereafter referred to as "parameterization method" in this chapter) that allows me to estimate the glacier-derived freshening without setting any endmember so long as basic ocean hydrographic data (T, S, DO, and Pr) are available. Applying this method to the Southern Ocean coastal oceans (SOc, seas around Antarctica, here defined as the region where the seafloor is shallower than 1,500 m, south of 60°S) using ocean hydrographic data set from 1926 to 2016 were collected from the Global Ocean Data Analysis Project version 2 (GLODAP_v2) and Southern Ocean Atlas (SOA)[17,72], I obtained spatial distributions and multi-decadal time series of the glacier-derived freshening over the SOc.

3.3 Estimation of freshwater input with the parameterization technique

Data used in this study

The observational data used for constructing the parameterizations of DIC (DIC, T, S, DO, and Pr) were sourced from GLODAPv2 of the SO from 2000 to 2017[17]. The quality of data on chemicals such as carbon species and nutrients after 2000 was controlled using certified reference materials[73]. Therefore, high-accuracy data for these chemicals began to be obtained mainly after 2000. Basic hydrographic data (T, S, DO, Pr) used to estimate the time series of freshening over the SOc were sourced from GLODAPv2_2019 from 1979 to 2016 and SOA from 1926 to 1984 (south of 60 ° S, bottom depth shallower than 1,500 m)[17,72]. To construct the DIC parameterizations, I used 46,753 data points for DIC_{open} and 2,059 data points for $DIC_{coastal}$ from 2000 to 2017 (Fig. 3.1). To estimate the time series of freshening, I used 23,449 data points from 1926 to 2016 (Fig. 3.2).

Construction of DIC parameterizations and its quality validation

Here, I used MLR to construct the parameterizations of DIC in the SO, and I established for the first time DIC parameterizations that can be applied to the entire SO from the surface ocean to the seafloor using T, S, AOU, and Pr (Fig. 3.3). AOU was calculated from DO and saturated oxygen concentration[74]. Several constraints were set for the raw data (Table 3.1).

The *F*-test was used to examine the significance of each parameter in my parameterizations (Table 3.2). A parameter with an *F*-value greater than 2.4, was considered to have a significant effect. After a stepwise regression, I selected AOU, T, S, and Pr for the DIC_{open}; the *F*-values of each were 375,574, 464,617, 29,712, and 5,505, respectively. Conversely, I used AOU, T, and S for the $DIC_{coastal}$, and the *F*-values of each were 4,964, 722, and 4,080, respectively. The variance inflation factor (VIF) was used to investigate the presence of multicollinearity between each parameter. Standardised regression coefficients (β) were used to compare the contribution of each parameter to DIC (Table 3.2). The closer the absolute value is to 1, the greater the contribution of the parameter. AOU was the most significant parameter in both the open SO and SOc. However, for the significance of T and S, DIC_{open} and $DIC_{coastal}$ show the opposite pattern.

The DIC_{open} is mainly controlled by T, while the key parameter becomes S for the $DIC_{coastal}$, partly proving that DIC in the SOc might have been affected by the input of melting freshwater.

I tested the accuracy of my parameterizations by conducting self-validation and cross-validation. First, I used the dataset that was used in the construction of my parameterizations to perform self-validation. Figures 3.4 and 3.5 show the spatial distributions of the difference between the observed and predicted DIC in the open SO and SOc, respectively. Most circumpolar regions (south of 50° S) showed no significant difference, implying that there are no "blind spots" where our parameterization cannot be applied.

I conducted cross-validation using an independent testing dataset to further verify the reliability of our parameterizations. For DIC parameterization in the open SO (DIC_{open}), I selected one independent cruise for each of the three sectors (Atlantic, Indian, and Pacific) that were not used in the construction of parameterization as the testing data set (Fig. 3.6). To quantify the extent of differences in DIC between the independent observed data and DIC_{open}, I used the mean absolute deviations (MADs) as follows:

$$MAD_{open} = \frac{1}{n}\sum_{i=1}^{n}\left|DIC_{obs\_i} - DIC_{open\_i}\right| \quad (3.2)$$

where MAD_{open} indicates the MAD of DIC_{open}, and n is the data amount of each independent testing dataset. MAD_{open} in the Pacific, Indian, and Atlantic sectors were 3.24, 2.48, and 5.06 μmol kg^{-1}, respectively (Table 3.3). These MAD values are smaller than the RMSE of DIC_{open} (6.08

μmol kg^{-1}), implying that DIC_{open} has sufficient reliability. In contrast, for the parameterization of SOc ($DIC_{coastal}$), the sparseness of observational data makes it difficult to find additional independent testing datasets for accuracy validation. To check the reliability of $DIC_{coastal}$, I used the "*k*-fold cross-validation"[75,76]. The *k*-fold cross-validation uses part of the available data to construct the parameterization (training dataset) and uses the remaining part to test it (testing dataset). Here, I divided the observational data set into 10 roughly equal-sized groups by longitude (i.e. k =10), using one group as the testing dataset and the remaining nine groups as the training data set. I then exchanged other groups as the testing dataset and the remaining nine groups as the training dataset. I repeated the above process nine times. The MAD of $DIC_{coastal}$ ($MAD_{coastal}$) is similar to that in equation 3.2:

$$MAD_{coastal} = \frac{1}{n}\sum_{i=1}^{n}\left|DIC_{obs\_i} - DIC_{coastal\_i}\right| \tag{3.3}$$

The results of the *k*-fold cross-validation for the SOc are shown in Fig. 3.7 and Table 3.4.

In the surface layer of both the open SO and the SOc, the differences in DIC between the validation observed data and our parameterizations are relatively large, which is probably due to the air-sea exchange and the seasonal differences between the observational data used.

Quantification of glacier-derived freshwater input in the SOc

As discussed in the main text, for the parameterization of chemical A, the predicted value of A (A_{pre}) contains a term for the ocean internal processes (A_{in}) and a term of the average external process (A_{ex}) within the spatiotemporal range of the observed dataset used (equation 3.1). Therefore, when I construct parameterizations for DIC in the open SO and SOc, they also satisfy this property (equations 3.4.1 to 3.4.6).

$$DIC_{open} = DIC_{in\_o} + DIC_{ex\_o} \qquad (3.4.1)$$

$$DIC_{in\_o} = C_{bio\_o} + C_{phy\_o} \qquad (3.4.2)$$

$$DIC_{ex\_o} = C_{ep\_o} + C_{si\_o} + C_{air\_o} \qquad (3.4.3)$$

$$DIC_{coastal} = DIC_{in\_c} + DIC_{ex\_c} \qquad (3.4.4)$$

$$DIC_{in\_c} = C_{bio\_c} + C_{phy\_c} \qquad (3.4.5)$$

$$DIC_{ex\_c} = C_{ep\_c} + C_{si\_c} + C_{air\_c} + C_g \qquad (3.4.6)$$

where DIC_{open} is defined as the predicted DIC in the open SO; $DIC_{coastal}$ is defined as the predicted DIC in the SOc; subscripts ‘in’ and ‘ex’ indicates terms of DIC concentrations which are controlled by internal processes and external processes of the ocean, respectively; subscripts ‘o and ‘c’ indicates terms of the open SO and the SOc, respectively. DIC_{in} mainly includes two components: the biological components (C_{bio}) and the physical components (C_{phy}), which can be represented by the parameters (T, S, AOU, Pr). The DIC_{ex} includes the evaporation and precipitation components (C_{ep}), sea ice (i.e. floating ice, iceberg) components (C_{si}), and air-sea exchange components (C_{air}) in both the open SO and the SOc. It is worth noting that in the SOc, there is a unique external DIC component derived from the Antarctic glacier (C_g).

I quantified the fraction of glacier-derived freshwater in the SOc (F_g) based on the above parameterizations and processes shown in Fig. 3.8. The seawater in the SOc consists of two components: one is the seawater coming from the open SO (referred to as initial seawater, with DIC concentration of DIC_{int}), and the other is the external freshwater added into the SOc (with DIC concentration of DIC_{fw}). The relationship between these water components can be expressed by the following conservation equations:

$$F_{fw} + F_{open} = 1 \tag{3.5}$$

$$\begin{aligned} F_{fw} \cdot DIC_{fw} + F_{int} \cdot DIC_{int} &= F_{fw} \cdot 0 + F_{int} \cdot DIC_{int} \\ &= DIC_{coastal} \end{aligned} \tag{3.6}$$

where F_{int} is the fraction of the initial seawater. F_{fw} is the fraction of freshwater added to SOc. DIC_{fw} was assumed to be equal to zero.

Assuming that the initial seawater in the SOc comes entirely from the open SO, this allows me to calculate DIC_{int} by substituting the parameters of the SOc into the open ocean parameterization (DIC_{open}).

$$DIC_{int} = DIC_{open}\,(T_c, S_c, AOU_c, Pr_c) = DIC_{in\_c} + DIC_{ex\_o} \tag{3.7}$$

Note that here DIC_{in} is completely controlled by the parameters (T, S, AOU, Pr), so when I substitute the parameters of the SOc into DIC_{open}, DIC_{in} becomes DIC_{in_c}, whereas DIC_{ex} remains as DIC_{ex_o} because this term is binding to DIC_{open}. Combining equation 3.5 with equation 3.6, I obtain F_{fw} as follows.

$$F_{fw} = (DIC_{int} - DIC_{coastal}) / DIC_{int} \tag{3.8}$$

Then substituting equations 3.4 into equation 3.8, I obtain the following equation:

$$F_{fw} = [(DIC_{in\_c} + DIC_{ex\_o}) - (DIC_{in\_c} + DIC_{ex\_c})] / DIC_{int}.$$

$$= [(DIC_{in\_c} - DIC_{in\_c}) + (DIC_{ex\_o} - DIC_{ex\_c})] / DIC_{int}.$$

$$= [(C_{ep\_o} - C_{ep\_c}) + (C_{si\_o} - C_{si\_c}) + (C_{air\_o} - C_{air\_c}) - C_g] / DIC_{int}. \tag{3.9}$$

The external components C_{ep}, C_{si}, and C_{air} exist in both the open SO and SOc. Therefore, I assume that

$$C_{ep\_o} \approx C_{ep\_c} \tag{3.10.1}$$

$$C_{si\_o} \approx C_{si\_c} \tag{3.10.2}$$

$$C_{air\_o} \approx C_{air\_c} \tag{3.10.3}$$

Finally, by substituting equation 3.10 into equation 3.9, I obtain F_{fw} as equation 3.11:

$$F_{fw} = [-C_g] / DIC_{int} = F_g \tag{3.11}$$

I found that F_{fw} is only controlled by the glacier-derived term, implying that the freshwater estimated by this method can be considered as the freshwater derived from Antarctic glacier melting (F_g).

I attempted to use various oceanic chemicals, including DIC, nitrate, and phosphate, as indicators of freshwater input. The essential advantage of DIC compared with other chemicals is that it maintains a relatively good linear relationship with hydrographic parameters, even within the surface mixed layer. Especially in the open ocean, the concentration of nutrients in the surface mixed layer is almost zero, which makes it difficult to construct parameterizations. Therefore, DIC was chosen as the freshwater indicator.

The average F_g in each sector of the SOc shown in Fig. 3.9d were calculated after gridding the raw data shown in Fig. 3.9a. This is done to lower the impact of spatial bias in the raw data distribution. I interpolated the raw data onto a 1°x 1° grid with a scale-length of 5 degrees of longitude and 1 degree of latitude using the Ocean Data View software (Fig. 3.10)[48]. The area of each grid was also considered when calculating the average, since the area of the grid varies with latitude. The average F_g of the SOc is shown as the area weight average of the three sectors. I changed the fraction of freshwater into volume by multiplying the fraction by the seawater volume. The seawater volumes used here were calculated by multiplying the average depth of all data profiles by the ocean surface area of the SOc or the three sectors. The ocean surface areas are listed in Table 3.5.

Calculation of the rate of overall freshening in the SOc based on the salinity trend

To quantify the impact of glacier melting on the SOc, I calculated the rate of overall freshening in the SOc according to the following steps: It is impossible to estimate the fraction of freshwater at a given moment through the salinity. Thus, I simply estimated the rate of freshening based on the rate of salinity change.

$$R_{all} = (dS_{obs}/dt) / S_{ave} \qquad (3.12)$$

where R_{all} indicates the rate of overall freshening in the SOc; dS_{obs}/dt indicates the observed salinity trend, which is controlled by evaporation and precipitation, sea ice, and glaciers, and S_{ave} is the average salinity over our research region ($S_{ave} = 34.3$).

The rate of glacier-derived freshening (R_g) is calculated as follow:

$$R_g = dF_g/dt \qquad (3.13)$$

Freshwater derived from glacier melting

Processes such as glacier melting, sea ice melting, and precipitation release large amounts of freshwater into the SOc. I treated these freshwater inputs as external process which can change the dissolved inorganic carbon (DIC, used as the indicator of freshening here) concentration in seawater and assumed that this glacier melting is the only significant different external factor between the SOc and the open ocean of SO. Then, I constructed the parameterizations of DIC for open SO and SOc, respectively. Both parameterizations can reconstruct DIC using T, S, apparent oxygen utilisation (AOU), and Pr from 0m to the bottom depth (equations 3.14 and 3.15).

$$\begin{aligned} DIC_{open} &= a_1 + a_2 \cdot AOU_o + a_3 \cdot T_o + a_4 \cdot S_o + a_5 \cdot Pr_o \\ &= 1024 + 0.5857 \cdot AOU_o - 8.452 \cdot T_o + 33.38 \cdot S_o + 1.798\times10^{-3} \cdot Pr_o \qquad (3.14) \end{aligned}$$

(Number of data points (n) = 46,753; coefficient of determination (R^2) = 0.98.

Root-mean-square error (RMSE) = 6.08 μmol kg^{-1})

$$DIC_{coastal} = b_1 + b_2 \cdot AOU_c + b_3 \cdot T_c + b_4 \cdot S_c + b_5 \cdot Pr_c$$

$$= 43.75 + 0.3833 \cdot AOU_c - 4.817 \cdot T_c + 62.43 \cdot S_c \qquad (3.15)$$

(n = 2,059; R^2 = 0.95; RMSE = 4.84 μmol kg^{-1})

where DIC_{open} indicates the predicted DIC in the open SO; $DIC_{coastal}$ indicates the predicted DIC in the SOc; a and b indicate the regression coefficients for these two parameterizations; subscript 'o' indicates parameter of the open SO; subscript 'c' represents parameter of the SOc.

Based on the difference in DIC between these two parameterizations, I expressed the fraction of glacier-derived freshwater in the SOc (F_g), as shown in equation 3.16.

$$F_g = (DIC_{int} - DIC_{coastal}) / DIC_{int}$$

$$= [(a_1 - b_1) + (a_2 - b_2) \cdot AOU_c + (a_3 - b_3) \cdot T_c + (a_4 - b_4) \cdot S_c + (a_5 - b_5) \cdot Pr_c] /$$

$$(a_1 + a_2 \cdot AOU_c + a_3 \cdot T_c + a_4 \cdot S_c + a_5 \cdot Pr_c) \qquad (3.16)$$

where DIC_{int} indicates the initial DIC concentration in the SOc without any freshwater input from the Antarctic glacier (equation 3.7). A positive F_g indicates freshwater released from the Antarctic glacier to the SOc, leading to freshening. The propagation of error derived from the DIC parameterizations suggests uncertainty in F_g of ~36%.

3.4 Results and discussion

Multi-decadal time-series of seawater freshening over the entire SOc

I applied our abovementioned parameterization method, to the observational hydrographic data in the SOc during 1926–2016, which were collected from GLODAP_v2 and SOA (23,449 data, almost in summertime)[17,72], to estimate the time series of freshening (shown as F_g) over SOc. To obtain the decadal change in freshening, I divided the dataset into seven periods with approximately 10-year intervals (P1,1926–1955; P2,1956–1965; P3,1966–1975; P4, 1976–1985; P5,1986–1997; P6,1998–2006; P7,2007–2016). Regarding spatial division, I divided the SOc into the Atlantic, Indian, and Pacific sectors which are mainly controlled by the ice shelves of the Antarctic Peninsula, East Antarctica, and West Antarctica, respectively (Fig. 3.9b).

In both the Atlantic and Indian sectors, the averaged F_g values were generally near 0 during all periods (Fig. 3.9a). However, in the Shirase Glacier Tongue (SGT, ~38 ° E) and Totten Ice Shelf (TIS, ~116 ° E), high basal melt rates from the 2000s have been reported[54,55]. My estimate does show a positive F_g in these regions (Fig. 3.9c). Contrarily, in the Pacific sector, dramatic ice sheet mass loss and high basal melting have been reported to occur in most regions over the last few decades, particularly over the Amundsen and Bellingshausen Seas (ABS, ~90 ° W – 150 ° W)[10,77,78]. My estimate shows significant positive F_g over the Pacific sector, including ABS and Ross Sea, during the late 20th century to the early 21st century (Fig. 3.9a), which spatiotemporally agrees with the above ice losses. Table 3.5 shows the rates of glacier-derived freshening (R_g) in the three sectors during the seven periods. During P5 to P6, R_g in the Pacific sector reached 0.28 ± 0.14‰ $year^{-1}$, while that in the whole SOc was 0.14 ± 0.07‰ $year^{-1}$.

Fig. 3.9c shows the vertical profiles of F_g in several focused regions, which have been reported to have significant ice sheet mass loss. In the Pacific sector, the highest F_g was 11 ± 4.0‰ in both ABS and the Eastern Ross Sea (ERS) in the 2000s. In both the Indian and Atlantic sectors, I also found F_g reached 4.0 ± 1.5‰ at the surface in the TIS, the SGT, and the Eastern Weddell Sea (EWS). At the Cape Darnley of the Indian sector, which is an important region for sea ice and bottom water formations in East Antarctica[79], the mass balance of the Amery Ice Shelf (AIS) has recently attracted extensive concern (Fig. 3.9b)[16,80,81]. In both 1961 and 2006, F_g was almost negative (see AIS (1961) and AIS (2006) in Fig. 3.9c), implying that freshwater exchange is dominated by freshwater consumption due to ice shelf freezing. Comparing the F_g in the AIS in 1961 with that in 2006, I identified a positive trend in F_g (–6 ± 2.2‰ to –1 ± 0.4‰) from 1961 to 2006 (Fig. 3.9c), implying that ice shelf freezing has been weakened, which may be related to mCDW intrusion[80,81].

To quantify the impact of glacier-derived freshwater on the overall freshening in the SOc, I calculated the rate of overall freshening (R_{all}) in the SOc using the salinity trend divided by the average salinity of the research region (equation 3.12). The correlations between R_g and R_{all} in the three sectors of the SOc are shown in Fig. 3.11a. From the slopes of the correlation lines, I found that during 1960–2016, glacier melting accounted for ~63%, ~28%, and ~92% of the total freshening occurred in the Atlantic, Indian, and Pacific sectors of the SOc, respectively (Fig. 3.11b). This suggests that glacier melting in West Antarctica and the Antarctic Peninsula plays a dominant role in the freshening of the surrounding seas.

I obtained the rate of glacier-derived freshwater input into the SOc by multiplying the regional average R_g by the seawater volume. I found that the rate of glacier-derived freshwater input in the SOc reached a maximum of 268 ± 134 Gt $year^{-1}$ (74 ± 37 Gt $year^{-1}$ as the lower limit) during the late 20th to early 21st centuries (1 Gt = 10^9 t = 10^{12} kg). If I assume that the melting of ice floe has no significant variation on a decadal time scale, I can consider that the difference between R_g and R_{all} (R_{other} in Fig. 3.11b) represents the rate of freshwater added by precipitation and melting of newly formed icebergs derived from calving, which have the potential to raise the global sea-level by up to 0.7 ± 0.4 mm $year^{-1}$.

Discussion

The mass balance of the Antarctic ice sheet is controlled by a combination of several processes[82]. In the Pacific sector, particularly in the ABS, much stronger freshening was observed than in the other two sectors. There is evidence that teleconnections with tropics such as SAM and El Niño–Southern Oscillation (ENSO) contribute significantly to the warm mCDW intrusion and the ice sheet mass loss in the ABS[83]. ABS is located near the eastern limb of the Ross Gyre and is adjacent to the main stem of the Antarctic Circumpolar Current (ACC). This geographic location is very conducive to the intrusion of mCDW into Antarctic ice cavities[77]. The Amundsen Sea Low (low-pressure centre located over the southern Pacific) can also drive the transportation of warm air to West Antarctica, which causes melting of the surface ice sheet and thereby contributes to freshening[84].

For the Indian and Atlantic sectors, the basal melt rates are generally low because of the typical cold shelf in this region[9]. However, my estimate and several previous studies showed that there were freshening signals in specific regions such as TIS, AIS, and SGT (Fig. 3.9c)[54,55,80,85]. Except for the effect of the positive SAM, the location and topographical conditions of these areas also play an unneglectable role. For instance, the SGT, which is located at the eastern limb of the Weddell Gyre (Fig. 3.9b), the deep trough along the continental slope deep into the ice front allows the mCDW to readily touch the ice shelf[55].

I identified a significant positive correlation between F_g over SOc and the SAM index since 1955[86] (R = 0.82; Fig. 3.9d and Fig. 3.12), suggesting that a positive SAM is a possible contributor to the Antarctic ice sheet mass loss. Forced by anthropogenic greenhouse gas emissions and stratospheric ozone depletion, SAM has exhibited a positive trend since 1955, resulting in the intensification and southward shift of westerly winds[47,58,86,87].

With the development of autonomous ocean observation robotics (Biogeochemical-Argo-float), I can obtain more spatiotemporally complete basic hydrographic data in the SO.

Applying my parameterization method to the Bio-Argo-float dataset[88,89], it will be possible to perform quasi-real-time monitoring of interactions between SOc and Antarctic glaciers and their impacts on the global ocean, which can greatly help us in a deeper understanding of global climate change in the future.

3.5 Supplementary information for this chapter

Interactions among the open SO, SOc, and Antarctic ice sheet

Fig. 3.8 shows the interactions among the open SO, SOc, and Antarctic glaciers. Initially, without any freshwater input from the Antarctic glacier, the seawater in SOc is supplied by open SO, implying that the processes which control the DIC concentration in seawater are all included in the DIC parameterization of open SO (DIC_{open}). Therefore, the DIC in the SOc can be expressed by substituting the parameters of SOc into the DIC parameterization of the open SOc. The warm mCDW (~1 °C) inflows from the open SO into the ice cavity southward. The freezing point of seawater at a depth of 1000 m was at ca. –3 ˚C. The difference in temperature of approximately 4 °C between the mCDW and the freezing point near the deep ice shelves has the potential to cause rapid ice shelf basal melt and freshwater release. The buoyant plume of freshwater, together with the mCDW, rose upward. The mixture of freshwater and seawater flowed northward along the surface ice shelf. The mixture of freshwater and initial seawater causes the DIC concentration in the SOc to become $DIC_{coastal}$. Other external processes such as sea ice production and melting, evaporation and precipitation, and air exchange can also change the DIC content in seawater, but these processes occur in both open SO and SOc, so they will not cause significant differences between DIC_{open} and $DIC_{coastal}$.

I assumed DIC_{open} to be negligibly affected by the glacier melting effect, because it is necessary to consider a 1000-year time scale, at the least, for the coastal water to completely spread to the open ocean[2].

Lack of observational data in ABS before P6

When I estimated the rate of glacier-derived freshening (R_g) in the three sectors of SOc, I divided the observational dataset into seven periods with approximately 10-year intervals (P1:1926–1955; P2:1956–1965; P3:1966–1975; P4: 1976–1985; P5:1986–1997; P6:1998–2006; P7:2007–2016) and calculated the R_g between every two adjacent periods. I noted that data of ABS before P6 is quite limited, which could bring uncertainty to our estimate in the Pacific sector if only taking the difference between the adjacent two periods (e.g. Fig. 3.9d, P5 to P6). Taking this uncertainty into account, I provided a possible range of R_g for the Pacific sector, with a lower limit of the average R_g during P2 to P6, since ABS data do exist in these two periods. For example, from P5 to P6, R_g reached a maximum of 268 ± 134 Gt year^{-1} (calculated by the change in F_g from P5 to P6), with a lower limit of 74 ± 37 Gt year^{-1} (calculated by the average change in F_g from P2 to P6).

Rationality of assumptions in this study

In this section, I discuss the rationality of the main assumptions made in this study: (i) Glacier melting is the only significant external possess which can influence the DIC content in the seawater between SOc and the open ocean of SO. (ii) All freshwater derived from the Antarctic ice sheet can be included in the SOc (bottom depth is shallower than 1,500 m, south of 60 ° S). (iii) The absorption of anthropogenic DIC (DIC_{ant}) had no significant impact on our estimate of freshening; (iv) DIC concentration was negligible in the meltwater from the surface ice sheet. I explain the rationality of these assumptions in detail as follows:

(i) This is the fundamental assumption of this study. I derived this in detail in the methods section (equation 3.4 to equation 3.11) why the results obtained by our method represent the fraction of glacial meltwater. It is worth noting that the characteristics of the SO vary significantly in the meridional direction, as many of the parameters of SO are distributed in a ribbon pattern along several fronts (e.g. the polar front, between approximately 50° and 60°S). For instance, sea ice coverage and air-sea exchange are obviously different between the north and south of the polar front. This seems to challenge our assumptions. In this study, SOc is defined as the region south of 60 °S and bottom depth shallower than 1500 m. Except for the Drake Passage, the boundary between SOc and open SO is further south than the polar front (~65 °S to 70 °S). Thus, the parameterization of open SO can reflect most of the processes controlling DIC concentration in seawater south of the polar front (except for glacier melting).

(ii) I wanted to estimate, as accurately as possible, the discharge of all freshwater derived from the Antarctic ice sheet into SOc. Therefore, for the definition of the SOc domain, I chose a bottom depth of 1,500 m as the boundary. Fig. 3.13 shows four north-south vertical sections of the freshwater fraction (F_g) estimated in this study around the SOc. I can see that the F_g at the surface gradually decreases with increasing distance from the Antarctic ice sheet and decreases to nearly zero before reaching the boundary of SOc. I can therefore assume that all significant freshwater inputs were confined to the SOc defined in this study.

(iii) Regarding the influence of DIC_{ant} on the DIC concentration in the SO, recent studies have reported that anthropogenic DIC in the SO increased at an average rate of ~1 μmol kg^{-1} year^{-1} from 1994 to 2007[90]. Considering the RMSE of our parameterizations, the propagation of error, and the time scale, my estimate can only be influenced by processes which lead to DIC change > 1 μmol kg^{-1} year^{-1}. Furthermore, there are anthropogenic terms in both the parameterization of SOc and open SO. The effect of DIC_{ant} can be cancelled out to some extent when calculating the fraction of freshwater (equation 3.9). Therefore, even if there is an effect of DIC_{ant}, this is not significant in our results.

(iv) The DIC concentrations in the meltwater from the surface ice sheet were assumed to be zero. The meltwater derived from the surface Antarctic ice sheet is in contact with the atmosphere and absorbs atmospheric CO_2 before flowing to the SOc. Consequently, the DIC concentration in the meltwater was not zero. If the meltwater has S = 0 and T = 0 in complete equilibrium with an atmospheric CO_2 of 410 ppm at present, the meltwater will have a DIC of 36 μmol kg^{-1}, which is approximately 1.6% of the average level of DIC in seawater. The actual concentration of DIC in the meltwater must be lower than this value because it takes a long time to become saturated with atmospheric CO_2[91]. Therefore, it is reasonable to neglect the DIC in surface ice sheet meltwaters.

Chapter 4 The biological production of carbon, silica and nitrogen over the SO

4.1 Biological production in the SO and the global climate

Model simulations predict that the SO accounts for more than 40% of the total anthropogenic carbon dioxide (CO_2) uptake into the ocean, despite accounting for approximately 30% of the total ocean surface area[5]. The SO is currently considered an important region in the global biogeochemical cycles of carbon and nutrients[92,93]. It is recognized as one of the largest high-nutrient low-chlorophyll (HNLC) regions with low biological productivity despite nutrient abundance there[94]. During the Last Glacial Maximum (LGM, ~25,000 years ago), an increase in biological production in the SO may have reduced the atmospheric CO_2 concentration and contributed to global cooling[95].

Unfortunately, the present spatiotemporal distribution of net community production (NCP) as biological productivity over the SO, which equals to the downward export of carbon materials from the surface to the deep ocean[96], is still unclear owing to the sparseness shipboard observational data caused by observation difficulty resulting from severe weather and oceanographic conditions[17]. Recently, in the SO, accelerated mass loss of the Antarctic ice sheet may have promoted ocean stratification[24,97]. The strengthening of ice sheet melting of the Antarctic ice sheet may release iron and increase biological production in SO[98], consequently drawdown atmospheric CO_2 concentration[95,99]. Therefore, it is essential to elucidate the biological production spatiotemporal variation in the SO to understand the future climate change.

4.2 Previous studies

The existing approaches for estimating the downward export (DE) of carbon and nutrients are mainly based on satellite and shipboard observations. Satellite observations are superior for estimating detailed spatiotemporal distribution of biological production from sea surface chlorophyll-a concentrations[100]. However, satellite-based estimation in the SO may be underestimated as satellites can only observe a depth of a few meters from the sea surface and cannot observe the Subsurface Chlorophyll-a Maximum (SCM) at a depth of tens of meters in the SO[101]. The shipboard observation of the DE is based on methods that require stoichiometric ratios (such as the Redfield ratio) that are assumed to be constant over the entire ocean[16], including on-deck incubation[102], nitrate time-series[103], and the sediment trap measurement[104]. However, owing to the sparseness of shipboard observational data due to the severe weather and oceanographic conditions in the SO and the spatiotemporal variability of the stoichiometric ratio, it is difficult to obtain an accurate spatiotemporal DE in the SO. Recently, studies regarding DE estimation using Biogeochemical Argo floats (BGC-Argo, observation instrument with a ~10 days cycle for approximately 6 years[105]) have come into our horizon. But these studies have utilized only change in DO or nitrate with a stoichiometric ratio, leading to uncertainties in DE estimation[21].

To overcome the problems of sparseness of observational data and stoichiometric ratio dependency, I attempted to utilize the parameterization technique to expand the data required to reconstruct the DIC, nitrate (N) and silicate (Si) spatiotemporal distribution to estimate the DE. To achieve these, I first try to introduce the non-linear regression model, Neural Network (NN) parameterization based on the high-accuracy hydrographic parameters of T, S, DO, and Pr from the GLODAPv2[17]. Then, I applied the NN parameterization to T, S, DO, and Pr measured by BGC-Argo working over the SO. Based on the change in the parameterization prediction of DIC, N and Si, I attempted to estimate the spatiotemporal high-resolution distribution of DE of these chemicals in the SO.

4.3 Quantification of biological production with neural network parameterization

Data used in this study

The BGC-Argo data used for constructing the spatiotemporal high-resolution mapping of DIC were sourced from the Japan Agency for Marine-Earth Science and Technology (JAMSTEC) of the SO (south of 30° S) from 2004 to 2019. Information on BGC-Argo, wherein I utilized the data, is depicted in Fig. 4.1.

Due to the BGC-Argo DO sensor drift, it was essential to correct the BGC-Argo DO data to the high-accuracy shipboard DO observational data. I utilized the monthly World Ocean Atlas 2018 (WOA18) dataset as the high-accuracy shipboard DO and S observational data to compare with BGC-Argo DO and S data at depths below the mixed layer (the mixed layer depth is estimated when the temperature gradient from the surface exceeds 0.5 °C)[38]. Additionally, I did not use the BGC-Argo if measurement period was less than one year because I can't find the annual periodicity. I obtained 154 valid BGC-Argo data with the above steps and then standardized it according to the WOA18 data depth levels.

The increase in anthropogenic CO_2 leads to a decrease in atmospheric oxygen concentration (maximum of 4 ppm year^{-1})[106], leading to a possible temporal difference between the WOA18 and BGC-Argo DO data. The WOA18 DO data are climatological data based on observations from 1955 to 2017 (the median year is 1986), and the BGC-Argo data used were from 2004 to 2019 (the median year was 2013). The 27-year difference in the period between the WOA18 and BGC-Argo data used here (2013–1986 = 27) resulted in a decrease in atmospheric oxygen concentration of 108 ppm, equivalent to 0.05% of the current atmospheric oxygen concentration (~209,000 ppm). Assuming water temperature of –1.8 °C and salinity of 34 in the SO, this reduction in the atmospheric oxygen concentration would lead to a decrease of 0.2 μmol kg^{-1} (0.05%) of the maximum saturated oxygen concentration of 370 μmol kg^{-1}. However, the precision of the GLODAPv2 DO data used in my construction of DIC parameterization is ~1%[9], which would lead to an error of approximately 4 μmol kg^{-1} for the maximum saturated oxygen concentration. Therefore, the reduction in the maximum saturated oxygen concentration caused by the reduction in oxygen concentration during the 27-year difference in the period between the

WOA18 and BGC-Argo data could be neglected when compared to the error in the GLODAPv2 DO data.

Parameterizations of DIC, N and Si

I used the NN model to construct the parameterizations of DIC, N and Si. As the MLR model can only reconstruct linear relationship between the explanatory variables and the objective variable, it is unsuitable for the surface mixed layer where biological and physical processes are complex. Contrastingly, the NN model can reconstruct non-linear relationship that allows me to predict DIC, N and Si from surface to the deep ocean without much constraints[107].

However, it is difficult for me to check the validity of the explanatory variables chosen for constructing the parameterizations through the NN model. Here, I used MLR to evaluate whether each parameter could be applied to DIC parameterization, and verified the presence of multicollinearity between each parameter using the variance inflation factor (VIF)[24]. As a result, I obtained valid parameters including T, S, and Pr to reflect physical processes and AOU to reflect biological processes.

I constructed parameterizations of DIC, N and Si over the SO using T, S, AOU, and Pr data after 2000 from the GLODAPv2 with the back-propagation neural network model. When comparing the root mean square error (RMSE) between the MLR and NN methods, although the NN model RMSE is slightly larger than that of the MLR model (Fig. 4.2), NN model can reconstruct chemicals over the SO including the surface mixed layer.

Estimation of NCP and Restoration

As biological production consumes DIC, N and Si in seawater, I treat the consumed chemicals during the production period as DE, and the restored chemicals during the restore period as Restoration (RES). To obtain the DE and RES by applying NN parameterizations to the BGC-Argo data, I set standard depth levels (5, 10, 20, 30, 40, 50, 60, 70, 80, 90, 100, 125, 150, 175, and 200 m), and obtained spatiotemporal distribution of each chemical at each depth over the SO.

In this study, to obtain the DE and RES in the water column, I first utilized the chemical concentrations at 30 m depth as a benchmark to delineate the production and restoration period (production period: period from the annual minimum concentration (C_{min}) to the annual maximum concentration (C_{max}); restore period: period from C_{max} to C_{min})[100]. I computed the chemical variations for each standard depth level during the production and restore periods. I then integrated chemical variations with depth. The DE integration depth is set to be the critical depth, where the amount of chemical variation is zero (see the schematic in Fig. 4.3). For RES, the integration depth level was the same as that of the DE. Note that the DE and RES estimated in this study are defined by the net change of each chemical in each period and, in fact, be apparent values. As the BGC-Argo cannot move autonomously and the flow motion is almost the same as that of seawater (Lagrangian motion)[108], I assume that the data collected by the same BGC-Argo are approximately in the same water column.

My method can account for DE at the SCM that are unobservable to satellites, which leads to potentially more significant total DE values in my study than in previous studies[20,101,109,110] (see Table 4.1). However, it is not be able to obtain hydrographic data from BGC-Argo for the Antarctic continental coast and areas where BGC-Argo has not floated due to the bathymetry of the SO coast and sea ice coverage[105]. To generate spatiotemporal high-resolution distribution of DE and RES in the SO, all reconstructed DE and RES data were extended to a common 1°×1° latitude-longitude grid south of 30°S with the weight average algorithm. However, compared with *in situ* NCP observations[111], the weighted average algorithm in this study may have uncertainty along the Antarctic coast because of the inability to reconstruct the real biological production along the Antarctic coast.

4.4 Results and discussion

Downward export mapping in the SO

I obtained the DE spatiotemporal distributions of DIC, N and Si for the first time, encompassing the entire SO by combining the NN-based parameterizations with BGC-Argo data (Fig. 4.4). As for the DIC and N, I found that DE is higher in the western boundary of all oceans (Fig. 4.4), as the westerly winds may bring micronutrients such as iron from Patagonia, southern Australia, New Zealand, and some islands located in the westerlies to the surface ocean and fertilize the phytoplankton blooms in the SO[112-114]. When I focus on the distribution of Si, high DE is found around the Antarctica (south of ~50˚S), which can be explained by the high degree of silicification of diatoms in that region due to the lack of iron[13]. By extending the BGC-Argo data to cover the entire SO, I found that over the SO, the total DE (tDE, DE multiplied by ocean surface area) of DIC, N and Si reached 340.9 ± 22.2 Tmol year^{-1} (Tmol = 10^{12} mol), 39.7 ± 2.6 Tmol year^{-1} and 79.8 ± 5.2 Tmol year^{-1}, which accounts for about 33%, 26% and 62% of the global ocean export given by the previous studies, respectively[2]. The DE distribution of DIC (also can be regarded as NCP) over the SO from 2004 to 2019 demonstrates that the geographic heterogeneity of the NCP is generally ~20% larger than that of the NCP model simulations and primary production of the SO[101,109,110] (Table 4.1). This difference may be derived from the consideration of SCM in our study using critical depth as the DE integral depth.

Regional characteristics of DE in the SO

To characterize the DE at the meridional direction and the basin scales, I divided the SO into three front zones[115] and three ocean sectors as follows: Antarctic zone (AZ), the zone south of the polar front (PF); the zone between the PF and the Subtropical Front (STF) and the zone between the STF and 30˚S; Indian sector: 20–150°E; Pacific sector: 150°E–60°W and Atlantic sector: 60°W–20°E (Fig. 4.5). As for the meridional characteristic, higher tDE of DIC and N was found between the PF and the STF due to the confluence of nutrient-rich sub-Antarctic waters with nutrient-poor subtropical waters and the mixing of cold and warm currents causing the seawater to mix up and down, interacting with westerly wind augmentation leading to sufficient nutrients[110]. Extremely higher tDE of Si was found in the AZ compare with other two zones. The AZ is known as a region dominated by diatom[116]. And the high degree of diatom silicification there can explain the observed high tDE of Si.

As for each ocean sector, the Pacific has the highest tDE of DIC and N, followed by the Indian, and the Atlantic (Fig. 4.5d). However, the ranking of the three ocean sectors was reversed in terms of tDE per unit area (Table 4.2). Despite the Atlantic Sector having the smallest area, it has the largest and widest DE area of all the ocean sectors, extending along the South American continent coast (Fig. 4.4), resulting in a larger tDE per unit area in the Atlantic Sector (Table 4.2). This is probably due to the supply of iron and other nutrients from South American continent[113].

To verify the accuracy of the DE and RES gridding, I also computed tDE and tRES of DIC for each sector and the entire SO by multiplying the NCP and RES average unit area by the ocean area (Table 4.2). I found that these values are essentially the same as the tNCP and tRES calculated by gridding, which proves the reliability of the tNCP and tRES obtained by gridding for the entire SO (Fig. 4.4).

Temporal variability of Downward export in the SO

To reveal the variations in the DE in the SO over the past decades and to predict the future dynamics of the SO, I plotted the time-series of the 3 years running mean of the DE in the SO from 2007 to 2017 (Fig. 4.6a). Over the mid SO (between 45°S and 60°S, Fig. 4.7), which is controlled by strong westerlies and characterized by nutrient-rich deep water upwelling and intermediate water formation, I found a significant decrease of ~0.8% per year in the DE of DIC and ~2.5% per year in the DE of N and no significant trend in DE of Si (Fig. 4.6a). This decreasing trend in the DE is opposite to the increasing trend during LGM[95]. During the LGM, the drying of the air due to global cooling and the northward shift of westerlies in the southern hemisphere transported terrestrial-derived dust into the ocean, leading to iron fertilization and an increase in marine biological production in the SO, which resulted in the drawdown of atmospheric CO_2 by approximately 80 ppm lower than the modern preindustrial average. Conversely, modern SO is predominantly affected by global warming and the southward shift of the westerlies, leading to accelerated melting of glaciers in the coastal region with a shallower mixed layer and limited upwelling of nutrients, which consequently causes a decreasing trend in biological production in the mid SO[24,95,111]. Therefore, the significant decrease in the DE in the mid-SO may be caused by feedback to the westerlies southward shift and stronger ocean stratification[24]. RES of all chemicals demonstrated no significant trend from 2007 to 2017. The new finding of a declining trend in DE in this study could indicate a reduction in anthropogenic carbon and nitrogen sink in the ocean, potentially accelerating future global warming and consequently altering the ocean biogeochemical cycle.

It should be noted that the DE trends may contain a decadal oscillation[35]. Therefore, long-term and more extensive observations using BGC-Argo will be required in the future to determine the significance of these trends.

Chapter 5 The decoupling between silica and nitrogen from SO to a global scale

5.1 The implication of the decoupling between silica and nitrogen

The Intermediate Water (IW) of the SO, serves as the major conduit of nutrients for the marine biological production in global low-latitude surface waters[6]. Without the nutrient transport from the IW, the biological production in the rest of global ocean would be reduced up to a quarter of its original level. With the meridional overturning circulation of the ocean, the nutrient-rich Circumpolar Deep Water (CDW) brings the nutrients accumulated for several hundred years into the surface SO, and after the uptake of phytoplankton (mainly diatoms) there, the remaining nutrients will be distributed globally along with the formation of the IW and the Bottom Water (BW)[6,117].

As an important macronutrient required by diatoms as dominant phytoplankton in the SO, silica in the SO has been attracting a lot of attention. Like other nutrients, dissolved silica (Si) in the SO is supplied to the surface SO by the upwelling of CDW, and then redistributed to the global ocean through the formation of IW as well as BW and the following northward flow. Recent modeling studies[117] indicate that the SO is experiencing a net input of Si, which raises a new question: where have these additional inputs of Si into the SO finally gone? To answer this question, Si* has been proposed which allows us to understand directly the unique behavior of Si compared to nitrogen[6]. In the surface SO (especially north of the Polar front (PF)), Si* shows significantly low values. Meanwhile, when I focus on the meridional concentration gradient of Si and N, the decreasing gradient of Si is much larger than that of N between the PF and the subantarctic front (SAF). This suggests that more Si is being removed from the SO surface water due to the lack of iron, and therefore less Si than N is being exported, which may be a limiting factor for biological productivity in the rest of global ocean. In addition, the SO, as the largest HNLC region in the global ocean, has received much attention for its potential biological productivity and its impact on global atmospheric CO_2 level. Current studies generally believe that the great supply of dust-borne iron to the ocean during the LGM period, which altered the Si and N utilization in the SO, led to an increase in marine biological productivity on a global scale and thus resulted in a drawdown in the atmospheric CO_2 level at that time[2]. However, due to the sparseness of extensive time-series observation of nutrients across the global ocean, global-scale studies of decoupling between Si and N have also primarily based on model simulations with stoichiometric ratios, which are often accompanied by large uncertainties due to variation in stoichiometric ratios and discrepancies between model simulations and realistic processes.

For solving the problem of sparse observational data in the SO, several breakthroughs have been made in recent studies[7,19,22,23]. Firstly, using parameterization technique can help us to expand the amount of nutrients observations and to reveal the variability of these substances in the ocean. This technique has been applied to the estimation of oceanic uptake of anthropogenic substances and to the assessment of freshwater in the Antarctic coastal waters, with promising results (Chapter 2&3). Secondly, by deploying the BGC-Argo into the ocean, I can obtain a global-scale hydrographic time-series dataset. However, since it can only obtain hydrological data, stoichiometric ratios are commonly used to estimate nutrient changes from DO changes. As mentioned above, stoichiometric ratios have spatiotemporal uncertainty, which can affect the estimation results. Here, to combine the advantages of the above two techniques, I newly develop a set of nutrient parameterizations based on neural network model that can better reconstruct the nonlinear relationship between nutrient and hydrographic data in the surface ocean and apply them to the global BGC-Argo data from 2003 to 2021 to directly obtain the time-series data of nutrients (c.f. Chapter 4.3). Based on the obtained time-series data, I present the global distribution of downward export and upward resupply of Si and N in the surface ocean and investigate the global distribution characteristics of the Si to N uptake ratio (Si/N).

5.2 Data used in this subject

Same with chapter 4, the observational data used for constructing the parameterizations of Si and N were sourced from GLODAPv2 over the global ocean from 2000 to 2020 (Fig. 5.2) [17]. The quality of data on chemicals such as carbon species and nutrients after 2000 was controlled using certified reference materials [73]. Therefore, high-accuracy data for these chemicals began to be obtained mainly after 2000. Here, the global ocean is divided into seven regions: 1, SO; 2, Equatorial Pacific; 3, Equatorial Atlantic; 4, Northern Indian Ocean; 5, North Pacific; 6, North

Atlantic; 7, Subarctic Atlantic, and I constructed parameterizations for each region, respectively. As for the BGC-Argo data used in this chapter, I collected 106,905 profiles from 370 BGC-Argo during 2003 to 2021 (Fig. 5.3).

5.3 Results and discussion

Downward export, restore and removal

I obtained the global distribution of downward export (DE), restoration (RES) and removal for Si and N by combining the neural network parameterizations of Si and N with the time series hydrographic data from Argo (c.f. Chapter 4.3). DE represents the amount of chemical exported to the deep ocean from the surface water (above the critical depth) for one year, and RES represents the amount of material supplied from the deep ocean to the surface water for one year. To investigate the balance between material export and supply in surface water for one year, I defined the difference between DE and RES as removal, which represents the net removal or net supply in surface water for one year.

I found that the DE of Si shows a clear spatial distribution feature (Fig. 5.4). The SO has the highest DE (up to a mean of -1.5 mol m^{-2} $year^{-1}$ in the Antarctic Zone (AZ)). Higher DE values are also found in the equatorial Pacific (-0.35 mol m^{-2} $year^{-1}$), North Pacific (-0.26 mol m^{-2} $year^{-1}$), and North Indian Ocean (-0.29 mol m^{-2} $year^{-1}$) and show a decreasing trend towards the north. In contrast, the DE of N does not show significant spatial characteristics, with averages between -0.37 to -0.26 mol m^{-2} $year^{-1}$ for each basin. The SO is characterized by high nutrient and low biological productivity in its surface layer due to the lack of iron supply. In addition, diatoms which dominate the SO tend to utilize more Si in this environment, since diatoms require iron for the synthesis of enzymes which necessary for N utilization[118]. The above two reasons lead to the result that the downward export of Si shows much higher values in the surface SO, especially in AZ south of Polar front (PF), compared to N. The meridional overturning circulation transports surface water in the SO northward through the intermediate layer to low-latitude regions as well as to mid- and high-latitude regions in the northern hemisphere. These intermediate waters rise to the surface at the equatorial regions as well as in the North Pacific, leading to the observed higher DE in these waters[119].

The distribution of the RES of Si is similar to that of the DE with a high north-south decreasing trend also observed in the SO, which raises the question that there must be imbalance between the RES and the DE to allow us to observe the decrease gradient of Si in the surface SO. Therefore, I investigate this imbalance through the distribution of removal (Fig. 5.4e&f; Fig. 5.5b). High negative removal values of Si, representing a net removal of Si from the surface water, are found in the waters off the Antarctic Peninsula as well as in the equatorial Pacific. The removal of N, on the other hand, shows no significant negative values. I consider this net removal to be the direct cause of the meridional decreasing gradient of Si. In some regions, such as the northeastern Indian Ocean as well as the northwestern Pacific Ocean, I observe significant positive Si removal, i.e., a net Si supply is present in the surface water of these regions. Since both DE as well as RES in this study were estimated over approximately semiannual periods, considering such a time-scale nutrient supply process, I suggest that active seasonal entrainment is the main reason for the net nutrient supply presented in the surface water of these regions.

Decoupling between Si and N

I here directly evaluated the decoupling between Si and N behaviors in the global surface ocean through the DE ratios of Si and N (Fig. 5.5f). To make it easily viewable, I used log scale to show Si/N. In the Pacific and Indian Ocean sectors, I observe Si/N greater than 1 in AZ as well as around the equatorial regions. This indicates that in these regions Si is more utilized by organisms at the surface and then exported to the deep ocean. In the previous section, when I discussed the distribution of downward export, I mentioned that due to the formation of the intermediate water, the surface water of the SO is transported northward and rises again to the surface at the equator as well as in the northern hemisphere[120]. This transport of water masses makes the equatorial as well as high latitude waters of the Northern Hemisphere also reflect a higher Si/N. Si/N reaches a maximum of ~8:1 in the AZ but drops to ~2:1 when it reaches the equatorial Pacific, which agrees with several previous studies[121-123]. If the equatorial surface waters are mainly controlled by the intermediate water from SO, the Si/N in the equatorial surface waters are expected to show higher values closer to those of the SO surface waters. I suggest that the reason for the lower-than-expected Si/N in equatorial surface waters is that Si has been removed substantially in the surface SO, which results in insufficient Si in low latitude upwelling waters to supply higher Si utilization[121]. In addition, the formation of NPIW in the North Pacific partially controls the biological production in equatorial surface water, which also reduces Si/N in equatorial surface water[124]. Si/N in the North Pacific, another upwelling region, shows values close to 1. Recent studies have shown that atmospheric dust and water transported from marginal seas (such as the sea of Okhotsk) can supply iron to the western North Pacific[125,126]. In combination with the partial supply of nutrient-rich intermediate water to the surface of the North Pacific for Si and N. This results in diatoms in the North Pacific exhibiting a normal Si to N utilization ratio of ~1:1 due to an adequate supply of Si, N, and iron[125-127]. Si/N of less than 1 is observed locally in the Polar front zone (PFZ), which is caused by the fact that Si in the surface water is depleted south of the PFZ, but N is remaining (silica leakage)[6,128].

The Atlantic is similar to the Pacific Ocean in that it also transports surface water from the SO northward through the subduction of intermediate waters as well as through upwelling[2]. However, unlike the Pacific Ocean, almost all the waters north of the SO show Si/N below 1, and the equatorial as well as subarctic waters where the intermediate waters rise are no exception. By observing the distribution of nutrients in the surface water of the Atlantic, I believe that the deficiency of Si is the main cause of this phenomenon. The newly formed nutrient-poor NADW in the North Atlantic flows southward, blocking nutrient exchange between the intermediate water and nutrient-rich bottom water, which results in lower nutrient concentrations in the Atlantic intermediate water than in the Pacific intermediate water (Fig. 5.5a) [119]. In contrast to Si, except the internal supply from the ocean, N can be supplied through external process such as nitrogen fixation and riverine input. The above reasons lead to the lower Si/N in the Atlantic.

The SO has long been considered the most significant ocean for this decoupling of Si and N, and it plays an important role in the biological production of the rest of global oceans. Here, I quantitatively show the detailed spatial distribution of the decoupling of Si and N from the SO to the subarctic seas. For Si, the SO has a higher potential for downward export due to the accumulation of a large amount of Si supplied from the deep ocean. Due to the depletion of nutrient in the surface water, the downward export is low in the oceans north of the SO but shows an increase in the downward export in parts of the ocean supplied by Si from the ocean interior (e.g., equatorial Pacific as well as the North Pacific). For N, although the SO also has a large amount of N, the downward export in the SO and the oceans north of it show almost the same value due to the deficiency of Fe. On the other hand, the distribution of Si/N shows us clearly the dominance of Si and N in different oceans. Especially, a contrast in Si/N is formed in the southern and northern Atlantic Ocean, i.e., Si/N in the AZ reaches ~8:1 while it becomes ~0.1:1 in the subarctic Atlantic. I found that the factors affecting the dominance of Si and N include mainly iron supply, Si and N concentrations and biological community composition[116,122]. The SO is recognized as a diatom-dominated ocean and has an abundance of nutrients in the surface[116], but the lack of iron and the high sinking speed of biogenic Si makes the SO show the high Si/N[118,122]. In contrast, although diatoms are also seasonally present in the North Atlantic, the fact that Si is hardly supplied from outside the ocean and N can be imported to the ocean through nitrogen fixation[129,130] or riverine input limits diatom growth and promotes the flourishing of organisms that primarily use N, resulting in the Si/N of only 0.1:1.

This subject is the first to evaluate the different biological uptake patterns of Si and N in the global ocean through an observation-based approach. And with the increase of Argo observations in the future, the prediction of the trend of Si and N decoupling in the global ocean by my method will also become possible. This will help us to grasp the future capacity of the ocean to absorb atmospheric CO_2 and global climate change.

Chapter 6 Conclusions

In this study, I have achieved the following goals:

I have successfully developed a new parameterization technique that can be used to elucidate the oceanic material cycle.

Using this technique, I have:

1. Estimated N_{ex} uptake in the SO.
2. Estimated ice-sheet-derived freshwater input in the Antarctic marginal regions.
3. Elucidated the biological production of carbon, nitrogen, and silica in the SO and its impact on the global ocean.

These results update our current understanding of the relationship between the SO and climate change and provide new insights for future ocean observations.

As for the future perspective, with the development of ocean in-situ observation, the accuracy of the methods used in this study can be further examined. And with the more BGC-Argo data collected in the future, broader and longer-term estimations of biological production in the ocean are expected to be achieved. The results of chapter 4 found that the C/N downwelling export ratio in the SO tends to increase at a rate of about 3% per year between 2007 and 2017. Taking a longer-term view of these changes in stoichiometric ratios is expected to provide further understanding of their impact on climate change in the SO.

Acknowledgement

In the end of this thesis, I’d like to appreciate those who helped and supported me during my doctor course. Thank my parents for your economic and spirit supports. Thank Prof. Yutaka Watanabe and all the teachers of Biogeochemistry course for your guidance and encouragement. Thank Dr. Bofeng Li and Ms. Yamauchi, for your advice and help for my study. Thank my wife Ms. Zhishan Sun for your accompany. Without each of you, this thesis could not be finished. Thank you all of you!

References

1 Marshall, J. & Speer, K. Closure of the meridional overturning circulation through Southern Ocean upwelling. *Nature Geoscience* **5**, 171-180, doi:10.1038/ngeo1391 (2012).

2 Sarmiento, J. L. & Gruber, N. *Ocean Biogeochemical Dynamics*. (Princeton University Press, 2006).

3 Myhre, G. *et al.* in *Climate Change 2013: The Physical Science Basis. Contribution of Working Group I to the Fifth Assessment Report of the Intergovernmental Panel on Climate Change* (eds T.F. Stocker *et al.*) Ch. 8, 659–740 (Cambridge University Press, 2013).

4 Gruber, N. *et al.* The oceanic sink for anthropogenic CO(2) from 1994 to 2007. *Science* **363**, 1193-1199, doi:10.1126/science.aau5153 (2019).

5 Khatiwala, S. *et al.* Global ocean storage of anthropogenic carbon. *Biogeosciences* **10**, 2169-2191, doi:10.5194/bg-10-2169-2013 (2013).

6 Sarmiento, J. L., Gruber, N., Brzezinski, M. A. & Dunne, J. P. High-latitude controls of thermocline nutrients and low latitude biological productivity. *Nature* **427**, 56-60, doi:10.1038/nature02127 (2004).

7 Pan, X. L., Li, B. F. & Watanabe, Y. W. The Southern Ocean with the largest uptake of anthropogenic nitrogen into the ocean interior. *Sci Rep* **10**, 8838, doi:10.1038/s41598-020-65661-2 (2020).

8 Vaughan, D. G. *et al.* in *Climate Change 2013: The Physical Science Basis. Contribution of Working Group I to the Fifth Assessment Report of the Intergovernmental Panel on Climate Change* (eds T.F. Stocker *et al.*) Ch. 4, 317–382 (Cambridge University Press, 2013).

9 Schmidtko, S., Heywood, K. J., Thompson, A. F. & Aoki, S. Multidecadal warming of Antarctic waters. *Science* **346**, 1227-1231, doi:10.1126/science.1256117 (2014).

10 Rignot, E., Jacobs, S., Mouginot, J. & Scheuchl, B. Ice-shelf melting around Antarctica. *Science* **341**, 266-270, doi:10.1126/science.1235798 (2013).

11 Hirano, D. *et al.* Strong ice-ocean interaction beneath Shirase Glacier Tongue in East Antarctica. *Nat Commun* **11**, 4221, doi:10.1038/s41467-020-17527-4 (2020).

12 Silvano, A. Changes in the Southern Ocean. *Nature Geoscience* **13**, 4-5, doi:10.1038/s41561-019-0516-2 (2020).

13 Brzezinski, M. A., Dickson, M.-L., Nelson, D. M. & Sambrotto, R. Ratios of Si, C and N uptake by microplankton in the Southern Ocean. *Deep Sea Research Part II: Topical Studies in Oceanography* **50**, 619-633, doi:10.1016/s0967-0645(02)00587-8 (2003).

14 Munk, W. Ocean science. Ocean freshening, sea level rising. *Science* **300**, 2041-2043, doi:10.1126/science.1085534 (2003).

15 Rignot, E. *et al.* Four decades of Antarctic Ice Sheet mass balance from 1979-2017. *Proc Natl Acad Sci U S A* **116**, 1095-1103, doi:10.1073/pnas.1812883116 (2019).

16 Aoki, S. *et al.* Freshening of Antarctic Bottom Water Off Cape Darnley, East Antarctica. *Journal of Geophysical Research: Oceans* **125**, doi:10.1029/2020jc016374 (2020).

17 Olsen, A. *et al.* GLODAPv2.2019 – an update of GLODAPv2. *Earth System Science Data* **11**, 1437-1461, doi:10.5194/essd-11-1437-2019 (2019).

18 Rye, C. D. *et al.* Rapid sea-level rise along the Antarctic margins in response to increased glacial discharge. *Nature Geoscience* **7**, 732-735, doi:10.1038/ngeo2230 (2014).

19 Arteaga, L. A., Pahlow, M., Bushinsky, S. M. & Sarmiento, J. L. Nutrient Controls on Export Production in the Southern Ocean. *Global Biogeochemical Cycles* **33**, 942-956, doi:10.1029/2019gb006236 (2019).

20 Johnson, K. S., Plant, J. N., Dunne, J. P., Talley, L. D. & Sarmiento, J. L. Annual nitrate drawdown observed by SOCCOM profiling floats and the relationship to annual net community production. *Journal of Geophysical Research: Oceans* **122**, 6668-6683, doi:10.1002/2017jc012839 (2017).

21 Kishi, S. *et al.* The Prominent Spring Bloom and Its Relation to Sea‐Ice Melt in the Sea of Okhotsk, Revealed by Profiling Floats. *Geophysical Research Letters* **48**, doi:10.1029/2020gl091394 (2021).

22 Li, B., Watanabe, Y. W. & Yamaguchi, A. Spatiotemporal distribution of seawater pH in the North Pacific subpolar region by using the parameterization technique. *Journal of Geophysical Research: Oceans* **121**, 3435-3449, doi:10.1002/2015jc011615 (2016).

23 Li, B. F., Watanabe, Y. W., Hosoda, S., Sato, K. & Nakano, Y. Quasi‐Real‐Time and High‐Resolution Spatiotemporal Distribution of Ocean Anthropogenic CO2. *Geophysical Research Letters* **46**, 4836-4843, doi:10.1029/2018gl081639 (2019).

24 Pan, X. L., Li, B. F. & Watanabe, Y. W. Intense ocean freshening from melting glacier around the Antarctica during early twenty-first century. *Sci Rep* **12**, 383, doi:10.1038/s41598-021-04231-6 (2022).

25 Ahmad, H. Machine Learning Applications in Oceanography. *Aquatic Research*, 161-169, doi:10.3153/ar19014 (2019).

26 Nakaoka, S. *et al.* Estimating temporal and spatial variation of ocean surface pCO2 in the North Pacific using a self-organizing map neural network technique. *Biogeosciences* **10**, 6093-6106, doi:10.5194/bg-10-6093-2013 (2013).

27 Yasunaka, S. *et al.* Mapping of sea surface nutrients in the North Pacific: Basin-wide distribution and seasonal to interannual variability. *Journal of Geophysical Research: Oceans* **119**, 7756-7771, doi:10.1002/2014jc010318 (2014).

28 Duce, R. A. *et al.* Impacts of atmospheric anthropogenic nitrogen on the open ocean. *Science* **320**, 893-897, doi:10.1126/science.1150369 (2008).

29 Gruber, N. & Galloway, J. N. An Earth-system perspective of the global nitrogen cycle. *Nature* **451**, 293-296, doi:10.1038/nature06592 (2008).

30 Capone, D. G., Bronk, D. A., Mulholland, M. R. & Carpenter, E. J. *Nitrogen in the Marine Environment*. （Elsevier, 2008).

31 Jickells, T. D. *et al.* A reevaluation of the magnitude and impacts of anthropogenic atmospheric nitrogen inputs on the ocean. *Global Biogeochemical Cycles*, doi:10.1002/2016gb005586 (2017).

32 Kim, I. N. *et al.* Chemical oceanography. Increasing anthropogenic nitrogen in the North Pacific Ocean. *Science* **346**, 1102-1106, doi:10.1126/science.1258396 (2014).

33 Panassa, E. *et al.* Variability of nutrients and carbon dioxide in the Antarctic Intermediate Water between 1990 and 2014. *Ocean Dynamics* **68**, 295-308, doi:10.1007/s10236-018-1131-2 (2018).

34 Woosley, R. J., Millero, F. J. & Wanninkhof, R. Rapid anthropogenic changes in CO2and pH in the Atlantic Ocean: 2003-2014. *Global Biogeochemical Cycles* **30**, 70-90, doi:10.1002/2015gb005248 (2016).

35 Watanabe, Y. W., Li, B. F. & Wakita, M. Long-Term Trends of Direct and Indirect Anthropogenic Effects on Changes in Ocean pH. *Geophysical Research Letters* **45**, 9106-9113, doi:10.1029/2018gl078084 (2018).

36 Lauvset, S. K. *et al.* A new global interior ocean mapped climatology: the 1° × 1° GLODAP version 2. *Earth System Science Data* **8**, 325-340, doi:10.5194/essd-8-325-2016 (2016).

37 Olsen, A. *et al.* The Global Ocean Data Analysis Project version 2 (GLODAPv2) – an internally consistent data product for the world ocean. *Earth System Science Data* **8**, 297-323, doi:10.5194/essd-8-297-2016 (2016).

38 de Boyer Montégut, C. Mixed layer depth over the global ocean: An examination of profile data and a profile-based climatology. *Journal of Geophysical Research* **109**, doi:10.1029/2004jc002378 (2004).

39 Emery, W. J. Water Types and Water Masses. in Ocean circulation. *Water Types and Water Masses*, 1556–1567, doi:10.1016/b0-12-227090-8/00279-7 (2003).

40 Switzer, A. C. Mapping nitrate in the global ocean using remotely sensed sea surface temperature. *Journal of Geophysical Research* **108**, doi:10.1029/2000jc000444 (2003).

41 Ishizu, M. & Richards, K. J. Relationship between oxygen, nitrate, and phosphate in the world ocean based on potential temperature. *Journal of Geophysical Research: Oceans* **118**, 3586-3594, doi:10.1002/jgrc.20249 (2013).

42 Anderson, L. A. & Sarmiento, J. L. Redfield ratios of remineralization determined by nutrient data analysis. *Global Biogeochemical Cycles* **8**, 65-80, doi:10.1029/93gb03318 (1994).

43 Stramma, L., Schmidtko, S., Levin, L. A. & Johnson, G. C. Ocean oxygen minima expansions and their biological impacts. *Deep Sea Research Part I: Oceanographic Research Papers* **57**, 587-595, doi:10.1016/j.dsr.2010.01.005 (2010).

44 Schlitzer, R. *Ocean Data View*, <https://odv.awi.de, 2020> (2020).

45 Gregg, W. W., Conkright, M. E., Ginoux, P., O'Reilly, J. E. & Casey, N. W. Ocean primary production and climate: Global decadal changes. *Geophysical Research Letters* **30**, doi:10.1029/2003gl016889 (2003).

46 Carter, L., McCave, I. N. & Williams, M. J. M. in *Antarctic Climate Evolution Developments in Earth and Environmental Sciences* 85-114 (2008).

47 Thompson, D. W. J. *et al.* Signatures of the Antarctic ozone hole in Southern Hemisphere surface climate change. *Nature Geoscience* **4**, 741-749, doi:10.1038/ngeo1296 (2011).

48 Menviel, L. *et al.* Southern Hemisphere westerlies as a driver of the early deglacial atmospheric CO(2) rise. *Nat Commun* **9**, 2503, doi:10.1038/s41467-018-04876-4 (2018).

49 Peck, V. L., Allen, C. S., Kender, S., McClymont, E. L. & Hodgson, D. A. Oceanographic variability on the West Antarctic Peninsula during the Holocene and the influence of upper circumpolar deep water. *Quaternary Science Reviews* **119**, 54-65, doi:10.1016/j.quascirev.2015.04.002 (2015).

50 Liu, X. *et al.* Enhanced nitrogen deposition over China. *Nature* **494**, 459-462, doi:10.1038/nature11917 (2013).

51 Oita, A. *et al.* Substantial nitrogen pollution embedded in international trade. *Nature Geoscience* **9**, 111-115, doi:10.1038/ngeo2635 (2016).

52 Rignot, E. *et al.* Four decades of Antarctic Ice Sheet mass balance from 1979-2017. *Proc. Natl. Acad. Sci. U.S.A.* **116**, 1095-1103, doi:10.1073/pnas.1812883116 (2019).

53 Church, J. A. *et al.* in *Climate Change 2013: The Physical Science Basis. Contribution of Working Group I to the Fifth Assessment Report of the Intergovernmental Panel on Climate Change* (eds T.F. Stocker *et al.*) Ch. 13, 1137–1216 (Cambridge University Press, 2013).

54 Rintoul, S. R. *et al.* Ocean heat drives rapid basal melt of the Totten Ice Shelf. *Sci. Adv.* **2**, e1601610, doi:10.1126/sciadv.1601610 (2016).

55 Hirano, D. *et al.* Strong ice-ocean interaction beneath Shirase Glacier Tongue in East Antarctica. *Nat. Commun* **11**, 4221, doi:10.1038/s41467-020-17527-4 (2020).

56 Mizobata, K., Shimada, K., Aoki, S. & Kitade, Y. The Cyclonic Eddy Train in the Indian Ocean Sector of the Southern Ocean as Revealed by Satellite Radar Altimeters and In Situ Measurements. *Journal of Geophysical Research: Oceans* **125**, doi:10.1029/2019jc015994 (2020).

57 Dinniman, M. *et al.* Modeling Ice Shelf/Ocean Interaction in Antarctica: A Review. *Oceanography* **29**, 144-153, doi:10.5670/oceanog.2016.106 (2016).

58 Saenko, O. A., Fyfe, J. C., Zickfeld, K., Eby, M. & Weaver, A. J. The Role of Poleward-Intensifying Winds on Southern Ocean Warming. *Journal of Climate* **20**, 5391-5400, doi:10.1175/2007jcli1764.1 (2007).

59 Liu, Y. *et al.* Ocean-driven thinning enhances iceberg calving and retreat of Antarctic ice shelves. *Proc. Natl. Acad. Sci. U.S.A.* **112**, 3263-3268, doi:10.1073/pnas.1415137112 (2015).

60 Aoki, S., Rintoul, S. R., Ushio, S., Watanabe, S. & Bindoff, N. L. Freshening of the Adélie Land Bottom Water near 140° E. *Geophysical Research Letters* **32**, doi:10.1029/2005gl024246 (2005).

61 Johnson, G. C., Purkey, S. G. & Bullister, J. L. Warming and Freshening in the Abyssal Southeastern Indian Ocean. *J. Clim.* **21**, 5351-5363, doi:10.1175/2008jcli2384.1 (2008).

62 Purkey, S. G. & Johnson, G. C. Antarctic Bottom Water Warming and Freshening: Contributions to Sea Level Rise, Ocean Freshwater Budgets, and Global Heat Gain. *J. Clim.* **26**, 6105-6122, doi:10.1175/jcli-d-12-00834.1 (2013).

63 Rhein, M. *et al.* in *Climate Change 2013: The Physical Science Basis. Contribution of Working Group I to the Fifth Assessment Report of the Intergovernmental Panel on Climate Change* (eds T.F. Stocker *et al.*) Ch. 3, 255–316 (Cambridge University Press, 2013).

64 Adusumilli, S., Fricker, H. A., Medley, B., Padman, L. & Siegfried, M. R. Interannual variations in meltwater input to the Southern Ocean from Antarctic ice shelves. *Nat Geosci* **13**, 616-620, doi:10.1038/s41561-020-0616-z (2020).

65 Silvano, A. *et al.* Freshening by glacial meltwater enhances melting of ice shelves and reduces formation of Antarctic Bottom Water. *Sci Adv* **4**, eaap9467, doi:10.1126/sciadv.aap9467 (2018).

66 Aoki, S. *et al.* Reversal of freshening trend of Antarctic Bottom Water in the Australian-Antarctic Basin during 2010s. *Sci. Rep.* **10**, 14415, doi:10.1038/s41598-020-71290-6 (2020).

67 Hellmer, H. H., Huhn, O., Gomis, D. & Timmermann, R. On the freshening of the northwestern Weddell Sea continental shelf. *Ocean Science* **7**, 305-316, doi:10.5194/os-7-305-2011 (2011).

68 Jacobs, S. S., Giulivi, C. F. & Mele, P. A. Freshening of the Ross Sea during the late 20th century. *Science* **297**, 386-389, doi:10.1126/science.1069574 (2002).

69 Silvano, A. *et al.* Freshening by glacial meltwater enhances melting of ice shelves and reduces formation of Antarctic Bottom Water. *Sci. Adv.* **4**, eaap9467, doi:10.1126/sciadv.aap9467 (2018).

70 Pan, X. L., Li, B. F. & Watanabe, Y. W. The Southern Ocean with the largest uptake of anthropogenic nitrogen into the ocean interior. *Sci. Rep.* **10**, 8838, doi:10.1038/s41598-020-65661-2 (2020).

71 Clement, D. & Gruber, N. The eMLR(C*) Method to Determine Decadal Changes in the Global Ocean Storage of Anthropogenic CO2. *Global Biogeochem. Cycles* **32**, 654-679, doi:10.1002/2017gb005819 (2018).

72 Olbers, D. G., Viktor V; Seiß, Guntram; Schröter, Jens. Hydrographic Atlas of the Southern Ocean in original file formats. *PANGAEA*, doi:10.1594/PANGAEA.750658 (2010).

73 Dickson, A. G., Sabine, C.L. and Christian, J.R. Guide to best practices for ocean CO_2 measurements. *PICES spec. publ.* **191** (2007).

74 Weiss, R. F. The solubility of nitrogen, oxygen and argon in water and seawater. *Deep-Sea Res. Oceanogr. Abstr.* **17**, 721-735, doi:10.1016/0011-7471(70)90037-9 (1970).

75 Hastie, T., Tibshirani, R. & Friedman, J. H. *The Elements of Statistical Learning: Data Mining, Inference, and Prediction*. (Springer, 2009).

76 Fushiki, T. Estimation of prediction error by using K-fold cross-validation. *Stat. Comput.* **21**, 137-146, doi:10.1007/s11222-009-9153-8 (2009).

77 Nakayama, Y., Menemenlis, D., Zhang, H., Schodlok, M. & Rignot, E. Origin of Circumpolar Deep Water intruding onto the Amundsen and Bellingshausen Sea continental shelves. *Nat. Commun* **9**, 3403, doi:10.1038/s41467-018-05813-1 (2018).

78 Bingham, R. G. *et al.* Inland thinning of West Antarctic Ice Sheet steered along subglacial rifts. *Nature* **487**, 468-471, doi:10.1038/nature11292 (2012).

79 Ohshima, K. I. *et al.* Antarctic Bottom Water production by intense sea-ice formation in the Cape Darnley polynya. *Nature Geoscience* **6**, 235-240, doi:10.1038/ngeo1738 (2013).

80 Wen, J. *et al.* Basal melting and freezing under the Amery Ice Shelf, East Antarctica. *Journal of Glaciology* **56**, 81-90, doi:10.3189/002214310791190820 (2017).

81 Williams, G. D. *et al.* The suppression of Antarctic bottom water formation by melting ice shelves in Prydz Bay. *Nat. Commun* **7**, 12577, doi:10.1038/ncomms12577 (2016).

82 Noble, T. L. *et al.* The Sensitivity of the Antarctic Ice Sheet to a Changing Climate: Past, Present, and Future. *Reviews of Geophysics* **58**, doi:10.1029/2019rg000663 (2020).

83 Steig, E. J., Ding, Q., Battisti, D. S. & Jenkins, A. Tropical forcing of Circumpolar Deep Water Inflow and outlet glacier thinning in the Amundsen Sea Embayment, West Antarctica. *Annals of Glaciology* **53**, 19-28, doi:10.3189/2012AoG60A110 (2017).

84 Raphael, M. N. *et al.* The Amundsen Sea Low: Variability, Change, and Impact on Antarctic Climate. *Bulletin of the American Meteorological Society* **97**, 111-121, doi:10.1175/bams-d-14-00018.1 (2016).

85 Nicholls, K. W. *et al.* A ground-based radar for measuring vertical strain rates and time-varying basal melt rates in ice sheets and shelves. *Journal of Glaciology* **61**, 1079-1087, doi:10.3189/2015JoG15J073 (2017).

86 Marshall, G. J. Trends in the Southern Annular Mode from Observations and Reanalyses. *J. Clim.* **16**, 4134-4143, doi:10.1175/1520-0442(2003)016<4134:Titsam>2.0.Co;2 (2003).

87 Stammerjohn, S. E., Martinson, D. G., Smith, R. C., Yuan, X. & Rind, D. Trends in Antarctic annual sea ice retreat and advance and their relation to El Niño–Southern Oscillation and Southern Annular Mode variability. *J. Geophys. Res.* **113**, doi:10.1029/2007jc004269 (2008).

88 Akazawa Fumihiko *et al.* Argo float data and metadata from Global Data Assembly Centre (Argo GDAC). *SEANOE*, doi:10.17882/42182 (2020).

89 Talley, L. D. *et al.* Southern Ocean Biogeochemical Float Deployment Strategy, With Example From the Greenwich Meridian Line (GO-SHIP A12). *J Geophys Res Oceans* **124**, 403-431, doi:10.1029/2018JC014059 (2019).

90 Gruber, N. *et al.* The oceanic sink for anthropogenic CO_2 from 1994 to 2007. *Science* **363**, 1193-1199, doi:10.1126/science.aau5153 (2019).

91 Lewis, E. R. W., D. W. R. Program Developed for CO_2 System Calculations. United States. doi:10.15485/1464255 (1998).

92 Gruber, N. *et al.* Oceanic sources, sinks, and transport of atmospheric CO2. *Global Biogeochemical Cycles* **23**, n/a-n/a, doi:10.1029/2008gb003349 (2009).

93 Takahashi, T. *et al.* Global sea–air CO2 flux based on climatological surface ocean pCO2, and seasonal biological and temperature effects. *Deep Sea Research Part II:*

Topical Studies in Oceanography **49**, 1601-1622, doi:10.1016/s0967-0645(02)00003-6 (2002).

94 Boyd, P. W. *et al.* Mesoscale iron enrichment experiments 1993-2005: synthesis and future directions. *Science* **315**, 612-617, doi:10.1126/science.1131669 (2007).

95 Sigman, D. M. & Boyle, E. A. Glacial/interglacial variations in atmospheric carbon dioxide. *Nature* **407**, 859-869, doi:10.1038/35038000 (2000).

96 Stanley, R. H. R., Kirkpatrick, J. B., Cassar, N., Barnett, B. A. & Bender, M. L. Net community production and gross primary production rates in the western equatorial Pacific. *Global Biogeochemical Cycles* **24**, n/a-n/a, doi:10.1029/2009gb003651 (2010).

97 Shadwick, E. H., Tilbrook, B. & Currie, K. I. Late-summer biogeochemistry in the Mertz Polynya: East Antarctica. *Journal of Geophysical Research: Oceans* **122**, 7380-7394, doi:10.1002/2017jc013015 (2017).

98 Duprat, L. P. A. M., Bigg, G. R. & Wilton, D. J. Enhanced Southern Ocean marine productivity due to fertilization by giant icebergs. *Nature Geoscience* **9**, 219-221, doi:10.1038/ngeo2633 (2016).

99 Martinez-Garcia, A. *et al.* Iron fertilization of the Subantarctic ocean during the last ice age. *Science* **343**, 1347-1350, doi:10.1126/science.1246848 (2014).

100 Behrenfeld, M. J. & Falkowski, P. G. Photosynthetic rates derived from satellite-based chlorophyll concentration. *Limnology and Oceanography* **42**, 1-20, doi:10.4319/lo.1997.42.1.0001 (1997).

101 Li, Z., Lozier, M. S. & Cassar, N. Linking Southern Ocean Mixed - Layer Dynamics to Net Community Production on Various Timescales. *Journal of Geophysical Research: Oceans* **126**, doi:10.1029/2021jc017537 (2021).

102 Bender, M. *et al.* A comparison of four methods for determining planktonic community production1. *Limnology and Oceanography* **32**, 1085-1098, doi:10.4319/lo.1987.32.5.1085 (1987).

103 MacCready, P. & Quay, P. Biological export flux in the Southern Ocean estimated from a climatological nitrate budget. *Deep Sea Research Part II: Topical Studies in Oceanography* **48**, 4299-4322, doi:10.1016/s0967-0645(01)00090-x (2001).

104 Trull, T. W., Bray, S. G., Manganini, S. J., Honjo, S. & François, R. Moored sediment trap measurements of carbon export in the Subantarctic and Polar Frontal zones of the Southern Ocean, south of Australia. *Journal of Geophysical Research: Oceans* **106**, 31489-31509, doi:10.1029/2000jc000308 (2001).

105 Bittig, H. C. *et al.* A BGC-Argo Guide: Planning, Deployment, Data Handling and Usage. *Frontiers in Marine Science* **6**, doi:10.3389/fmars.2019.00502 (2019).

106 Langenfelds, R. L. *et al.* Partitioning of the global fossil CO2sink using a 19-year trend in atmospheric O2. *Geophysical Research Letters* **26**, 1897-1900, doi:10.1029/1999gl900446 (1999).

107 Kalantary, S., Jahani, A. & Jahani, R. MLR and ANN Approaches for Prediction of Synthetic/Natural Nanofibers Diameter in the Environmental and Medical Applications. *Sci Rep* **10**, 8117, doi:10.1038/s41598-020-65121-x (2020).

108 Xing, X., Wells, M. L., Chen, S., Lin, S. & Chai, F. Enhanced Winter Carbon Export Observed by BGC - Argo in the Northwest Pacific Ocean. *Geophysical Research Letters* **47**, doi:10.1029/2020gl089847 (2020).

109 Arteaga, L., Haëntjens, N., Boss, E., Johnson, K. S. & Sarmiento, J. L. Assessment of Export Efficiency Equations in the Southern Ocean Applied to Satellite - Based Net Primary Production. *Journal of Geophysical Research: Oceans* **123**, 2945-2964, doi:10.1002/2018jc013787 (2018).

110 Chang, C. H., Johnson, N. C. & Cassar, N. Neural network-based estimates of Southern Ocean net community production from in situ O<sub>2</sub> / Ar and satellite observation: a methodological study. *Biogeosciences* **11**, 3279-3297, doi:10.5194/bg-11-3279-2014 (2014).

111 Lin, Y. *et al.* Decline in plankton diversity and carbon flux with reduced sea ice extent along the Western Antarctic Peninsula. *Nat Commun* **12**, 4948, doi:10.1038/s41467-021-25235-w (2021).

112 Graham, R. M., De Boer, A. M., van Sebille, E., Kohfeld, K. E. & Schlosser, C. Inferring source regions and supply mechanisms of iron in the Southern Ocean from satellite chlorophyll data. *Deep Sea Research Part I: Oceanographic Research Papers* **104**, 9-25, doi:10.1016/j.dsr.2015.05.007 (2015).

113 Johnson, K. S., Chavez, F. P. & Friederich, G. E. Continental-shelf sediment as a primary source of iron for coastal phytoplankton. *Nature* **398**, 697-700, doi:10.1038/19511 (1999).

114 Paparazzo, F. *et al.* Patagonian Dust as a Source of Macronutrients in the Southwest Atlantic Ocean. *Oceanography* **31**, 33-39, doi:10.5670/oceanog.2018.408 (2018).

115 Chapman, C. C., Lea, M.-A., Meyer, A., Sallée, J.-B. & Hindell, M. Defining Southern Ocean fronts and their influence on biological and physical processes in a changing climate. *Nature Climate Change* **10**, 209-219, doi:10.1038/s41558-020-0705-4 (2020).

116 Mendes, C. R. B. *et al.* Cross-front phytoplankton pigments and chemotaxonomic groups in the Indian sector of the Southern Ocean. *Deep Sea Research Part II: Topical Studies in Oceanography* **118**, 221-232, doi:10.1016/j.dsr2.2015.01.003 (2015).

117 Tréguer, P. J. The Southern Ocean silica cycle. *Comptes Rendus Geoscience* **346**, 279-286, doi:10.1016/j.crte.2014.07.003 (2014).

118 DeMaster, D. J. The accumulation and cycling of biogenic silica in the Southern Ocean: revisiting the marine silica budget. *Deep Sea Research Part II: Topical Studies in Oceanography* **49**, 3155-3167, doi:10.1016/s0967-0645(02)00076-0 (2002).

119 Sigman, D. M. *et al.* The Southern Ocean during the ice ages: A review of the Antarctic surface isolation hypothesis, with comparison to the North Pacific. *Quaternary Science Reviews* **254**, doi:10.1016/j.quascirev.2020.106732 (2021).

120 Dugdale, R. C. & Wilkerson, F. P. Silicate regulation of new production in the equatorial Pacific upwelling. *Nature* **391**, 270-273, doi:10.1038/34630 (1998).

121 Brzezinski, M. A., Dumousseaud, C., Krause, J. W., Measures, C. I. & Nelson, D. M. Iron and silicic acid concentrations together regulate Si uptake in the equatorial Pacific Ocean. *Limnology and Oceanography* **53**, 875-889, doi:10.4319/lo.2008.53.3.0875 (2008).

122 M. Franck, V., Brzezinski, M. A., Coale, K. H. & Nelson, D. M. Iron and silicic acid concentrations regulate Si uptake north and south of the Polar Frontal Zone in the Pacific Sector of the Southern Ocean. *Deep Sea Research Part II: Topical Studies in Oceanography* **47**, 3315-3338, doi:10.1016/s0967-0645(00)00070-9 (2000).

123 Yasunaka, S., Mitsudera, H., Whitney, F. & Nakaoka, S.-i. Nutrient and dissolved inorganic carbon variability in the North Pacific. *Journal of Oceanography* **77**, 3-16, doi:10.1007/s10872-020-00561-7 (2020).

124 Bibby, T. S. & Moore, C. M. Silicate:nitrate ratios of upwelled waters control the phytoplankton community sustained by mesoscale eddies in sub-tropical North Atlantic and Pacific. *Biogeosciences* **8**, 657-666, doi:10.5194/bg-8-657-2011 (2011).

125 Mahowald, N. M. *et al.* Atmospheric global dust cycle and iron inputs to the ocean. *Global Biogeochemical Cycles* **19**, n/a-n/a, doi:10.1029/2004gb002402 (2005).

126 Nishioka, J. *et al.* A review: iron and nutrient supply in the subarctic Pacific and its impact on phytoplankton production. *Journal of Oceanography* **77**, 561-587, doi:10.1007/s10872-021-00606-5 (2021).

127 Nishioka, J. *et al.* Iron supply to the western subarctic Pacific: Importance of iron export from the Sea of Okhotsk. *Journal of Geophysical Research* **112**, doi:10.1029/2006jc004055 (2007).

128 Hauck, J., Lenton, A., Langlais, C. & Matear, R. The Fate of Carbon and Nutrients Exported Out of the Southern Ocean. *Global Biogeochemical Cycles* **32**, 1556-1573, doi:10.1029/2018gb005977 (2018).

129 Tang, W., Li, Z. & Cassar, N. Machine Learning Estimates of Global Marine Nitrogen Fixation. *Journal of Geophysical Research: Biogeosciences* **124**, 717-730, doi:10.1029/2018jg004828 (2019).

130 Luo, Y. W., Lima, I. D., Karl, D. M., Deutsch, C. A. & Doney, S. C. Data-based assessment of environmental controls on global marine nitrogen fixation. *Biogeosciences* **11**, 691-708, doi:10.5194/bg-11-691-2014 (2014).

Tables

Table 2.1. Constraint conditions for parameterization of N_p in the SO.

Constraints		Remarks
Bottom depth	> 1500 m	Removing continental shelf
Nitrate concentration	> 0.2 µmol kg^{-1}	
Mixed layer depth	$\Delta T > 0.5$ °C [a]	$\Delta T \leq 0.5$ °C was not used
Salinity	34 – 35	
Water masses	Except NADW [b], SASW [c]	NADW: $34.8 < S < 35$ 1.5 °C < T < 4 °C SASW: T > 8 °C

[a] Mixed layer depth is defined as the depth at which temperature (T) changes by a given threshold value (ΔT; here, $\Delta T = 0.5$ °C) relative to the temperature at the surface [23].

[b] North Atlantic Deep Water

[c] Subantarctic Surface Water; in this study, we only removed the northern part of SASW in the Pacific sector.

Table 2.2. Summary of the parameterization in our study for nitrate (N_p) in the SO.

Parameter	*F* [a]	*B* [b]	Standardized β [c]	VIF [d]
Intercept	–	394.3	0	–
DO	903,917	-9.208×10^{-2}	–0.70	1.23
T	1,426,953	–1.534	–0.80	1.26
S	213,532	–9.862	–0.37	1.63
Pr	4,830	2.029×10^{-4}	0.06	1.63

[a] *F*-value with a significant level of $\alpha = 0.05$; significant when *F*-value over 2.4

[b] Regression coefficient

[c] Standardized regression coefficient

[d] Variance Inflation Factor; indicates no multicollinearity when VIF is below 10

Table 2.3. Mean Absolute Deviation (MAD) of difference between N_{obs} and N_p in three independent cruises along the Pacific, Indian, and Atlantic sectors in the SO during the period from 2000 to 2016.

Region	Cruise	n [a]	MAD (μmol kg^{-1})
Pacific Sector	320620140320	1,306	0.37
Indian Sector	33RR20070204	2,022	0.47
Atlantic Sector	06AQ20141202	223	0.64
RMSE of N_p (μmol kg^{-1})		0.80	

[a] Number of data points

Table 2.4. Total water column inventory of ΔN_{ex} in the SO. From the surface to 5,900-m depth south of 30°S during the 1990s – 2010s (Tg-N year^{-1}) (Pacific Sector: 150°E – 60°W; Indian Sector: 20°E – 150°E; Atlantic Sector: 60°W – 20°E). The uncertainty is the value of the standard error divided by the average of each sector (see Table 2.5 for detail).

Period	Pacific Sector	Indian Sector	Atlantic Sector	Southern Ocean
1990s–2000s	25±1	−4±1	17±1	38±2
2000s–2010s	24±1	100±2	−22±1	102±3
1990s–2010s	24±1	42±1	0.02±0	67±1

Table 2.5. Uncertainty of the estimation of ΔN_{ex} water column inventory in the SO.

Period		Pacific Sector	Indian Sector	Atlantic Sector	Southern Ocean
	grid number	5,309	4,365	2,802	12,476
1990s–2000s	average	0.0044	0.0009	0.0055	0.3652
	SE	0.00016	0.00021	0.00022	0.01628
	uncertainty	4%	22%	4%	4%
2000s–2010s	average	0.0042	0.0230	0.0069	0.9354
	SE	0.00016	0.00036	0.00033	0.02455
	uncertainty	4%	2%	5%	3%
1990s–2010s	average	0.0043	0.0107	0.0061	0.6186
	SE	0.00016	0.00028	0.00027	0.01189
	uncertainty	4%	3%	4%	2%

[a] Grid number in each sector when calculated the ΔN_{ex} water column inventory.

[b] Average of the inventory value of each grid point in unit of Tg-N year^{-1}.

[c] Standard error of the inventory value of each grid point in unit of Tg-N year^{-1}.

[d] Uncertainty of the ΔN_{ex} water column inventory, which is calculated by SE/average in each sector.

Table 3.1. Constraint conditions for DIC parameterizations.

Region	Constraints		Remarks
open SO	Bottom depth	> 1500 m	
	AOU	Remove deeper than 1000m & AOU< 165 μmol kg^{-1}	
	Salinity	34 – 35	
	Water masses	Remove NADW [a],	NADW: $34.8 < S < 35$ 1.5 °C < T < 4 °C
		SASW [b]	SASW: T > 8 °C [70]
coastal SO (SOc)	Bottom depth	≤ 1500 m	
	Salinity	34 – 35	

[a] North Atlantic Deep Water

[b] Sub-Antarctic Surface Water. In this study, we only removed SASW in the Pacific sector.

Table 3.2. Summary of parameterizations of DIC in this study.

Region	Parameter	F [a]	B [b]	Standardized β [c]	VIF [d]
open SO (DIC$_{open}$)	Intercept	–	1024	–	–
	AOU	375,574	0.5857	0.53	2.09
	T	464,617	– 8.452	– 0.5	1.54
	S	29,712	33.38	0.15	2
	Pr	5,505	1.798×10^{-3}	0.05	1.51
coastal SO (DIC$_{coastal}$)	Intercept	–	43.75	–	–
	AOU	4,964	0.3833	0.64	2.64
	T	722	– 4.817	– 0.19	1.54
	S	4,080	62.43	0.5	1.95

[a] F-value with a significance level of $\alpha = 0.05$; significant when F-value over 2.4.

[b] Regression coefficient

[c] Standardized regression coefficient

[d] Variance Inflation Factor; indicates no multicollinearity when VIF is below 10

Table 3.3. Mean Absolute Deviation (MAD) of difference between DIC_{obs} and DIC_{open} in three independent cruises along the Atlantic, Indian, and Pacific sectors in the open SO.

Region	**Cruise**	**n** [a]	**MAD_{open} (μmol kg^{-1})**
Atlantic Sector	06AQ20071128	111	5.06
Indian Sector	09AR20160111	97	2.48
Pacific Sector	49NZ20170208	141	3.24
RMSE of DIC_{open} (μmol kg^{-1})	6.08		

[a] Number of data points

Table 3.4. Result of the *k*-fold cross-validation of $DIC_{coastal}$.

Testing set	**n_test** [a]	**Longitude**	**Parameterization**	**n_train** [b]	**RMSE (μmol kg^{-1})**	**$MAD_{coastal}$ (μmol kg^{-1})**
1	200	178°W – 55°W	DIC = –11.25 – 5.149×T + 64.02×S + 0.3850×AOU	1859	4.75	4.23
2	200	55°W – 53°W	DIC = 29.06 – 5.050×T + 62.85×S + 0.3836×AOU	1859	4.74	3.91
3	200	53°W – 44°W	DIC = –7.260 – 5.028×T + 63.91×S + 0.3792×AOU	1859	4.57	4.92
4	200	44°W – 31°E	DIC = 49.32 – 4.786×T + 62.29×S + 0.3762×AOU	1859	4.76	3.74
5	200	31°E – 70°E	DIC = 34.09 – 4.893×T + 62.71×S + 0.3859×AOU	1859	4.98	2.59
6	200	70°E – 139°E	DIC = 59.60 – 4.654×T + 61.97×S + 0.3868×AOU	1859	4.80	3.95
7	200	139°E – 140°E	DIC = 79.95 – 4.828×T + 61.38×S + 0.3881×AOU	1859	4.92	3.13
8	200	140°E – 143°E	DIC = 78.71 – 4.620×T + 61.42×S + 0.3851×AOU	1859	4.90	3.30
9	200	143°E – 144°E	DIC = 82.38 – 4.503×T + 61.32×S + 0.3817×AOU	1859	4.97	2.99
10	259	144°E – 168°E	DIC = 52.92 – 4.650×T + 62.18×S + 0.3818×AOU	1800	4.95	2.77
Average					4.83	3.55

[a] Number of data in each testing set

[b] Number of data in each training set

Table 3.5. Rates of glacier-derived freshening（‰ year^{-1}) between each period during 1926 to 2016.

Region	Area (km^2)	P1–P2 [a]	P2–P3	P3–P4	P4–P5	P5–P6	P6–P7
Atlantic	9.8×10^5	-0.01 ± 0.01[c]	0.09 ± 0.04	-0.09 ± 0.05	0.05 ± 0.02	0.07 ± 0.03	-0.08 ± 0.04
Indian	8.6×10^5	0.11 ± 0.06	0.01 ± 0.01	0 ± 0	0.04 ± 0.02	-0.02 ± 0.01	0.02 ± 0.01
Pacific	1.4×10^6	0.01 ± 0	-0.19 ± 0.1	-0.09 ± 0.04	0.22 ± 0.11	0.28 ± 0.14	0 ± 0
SOc [b]	3.3×10^6	0.03 ± 0.01	-0.05 ± 0.03	-0.06 ± 0.03	0.12 ± 0.06	0.14 ± 0.07	-0.02 ± 0.01

[a] P1: 1926–1955, P2: 1956–1965, P3: 1966–1975, P4: 1976–1985, P5: 1986–1997, P6: 1998–2006, P7: 2007–2016

[b] Rates over the SOc are shown as the area weight average of the three sectors.

[c] Error shows the uncertainty of 50% derived from the RMSE of the parameterizations and the propagation of errors arising in the subsequent calculations.

Table 3.6. Comparison of the rate of glacier-derived freshening (R_g) and overall freshening (R_{all}) in the SOc during 1960 ~ 2016.

Location	**Sector**	**Period**	**R_g (‰ year^{-1})**	**R_{all} [a] (‰ year^{-1})**
AP [b]	Atlantic	1979-1996	0.2	0.24
AP	Atlantic	1996-2016	-0.1	-0.21
WS [c]	Atlantic	1973-1989	0.03	0.09
150°E	Indian	2002-2013	0.11	0.3
90°E	Indian	1978-1996	-0.03	-0.2
CD [d]	Indian	1978-2006	0.02	0.04
RS_west [e]	Pacific	1996-2011	0.22	0.21
RS_east [f]	Pacific	1994-2007	0.09	0.07
ABS	Pacific	1960-2000	0	-0.03

[a] R_{all} is calculated from salinity trend based on an average salinity of 34.3 in the SOc (Eq. S12)

[b] Antarctic Peninsula

[c] Weddell Sea

[d] Ross Sea west

[f] Ross Sea east

Table 4.1. Comparison of tNCP (tDE of DIC) between this study and the previous studies.

References	Method	Period	Location	tNCP (Pg-C $year^{-1}$)
This subject	Neural network-based parameerization and BGC-Argo	2004–2019	South of 30°S	4.1 ± 0.3
Arteaga et al. (2018) [24]	Carbon export efficiency models and satellite observation*	2005–2016	South of 30°S	2.7 ± 0.6
Li et al. (2021) [25]	VGPM, BGC-Argo and NCP model*	1997–2020	South of 35°S	3.91 ± 0.16
Chang et al. (2014) [26]	Neural network-based self-organizing map (SOM)*	1998–2009	South of 30°S	3.5
Johnson et al. (2017) [49]	Annual nitrate drawdown measured by BGC-Argo	2009–2016	South of 50°S	1.3

* Satellite data-based method

Table 4.2. Comparison of the regional amount of NCP (DE of DIC) and RES of DIC in each sector of the SO. The uncertainties in these estimations are 6.5%.

Region	Location	Ocean surface area ($10^{12}m^2$)	[a] NCP (mol-C m^{-2} $year^{-1}$)	[b] RES (mol-C m^{-2} $year^{-1}$)	[c] tNCP’ (Tmol-C $year^{-1}$)	[d] tRES’ (Tmol-C $year^{-1}$)
SO	South of 30˚S	110	3.1 ± 0.2	2.7 ± 0.2	341 ± 22	297 ± 22
Indian sector	20˚E – 150˚E	37	2.9 ± 0.2	2.7 ± 0.2	107 ± 7	100 ± 7
Pacific sector	150˚E – 60˚W	47	2.9 ± 0.2	2.5 ± 0.2	136 ± 9	118 ± 9
Atlantic sector	60˚W – 20˚E	26	3.6 ± 0.2	3.0 ± 0.2	93 ± 5	78 ± 5

[a] NCP of unit area.

[b] RES of unit area.

[c] total NCP in each region, calculated by NCP of unit area multiplied ocean surface area.

[d] total RES in each region, calculated by RES of unit area multiplied ocean surface area.

Figures

Fig. 1.1

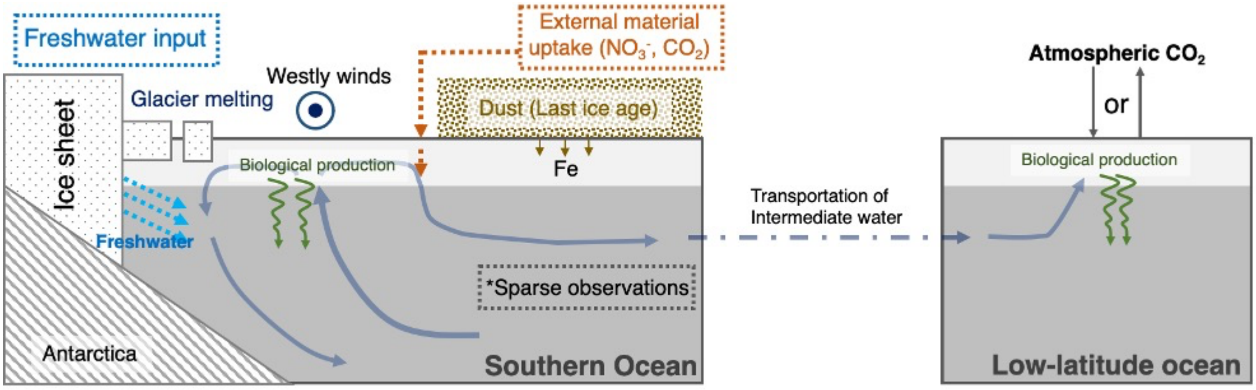

Fig. 1.1 Schematic of the processes occur in the SO. Freshwater exchange between the Antarctic ice sheet and the SO, external materials uptake and atmospheric CO_2 uptake are shown in this figure.

Fig. 2.1

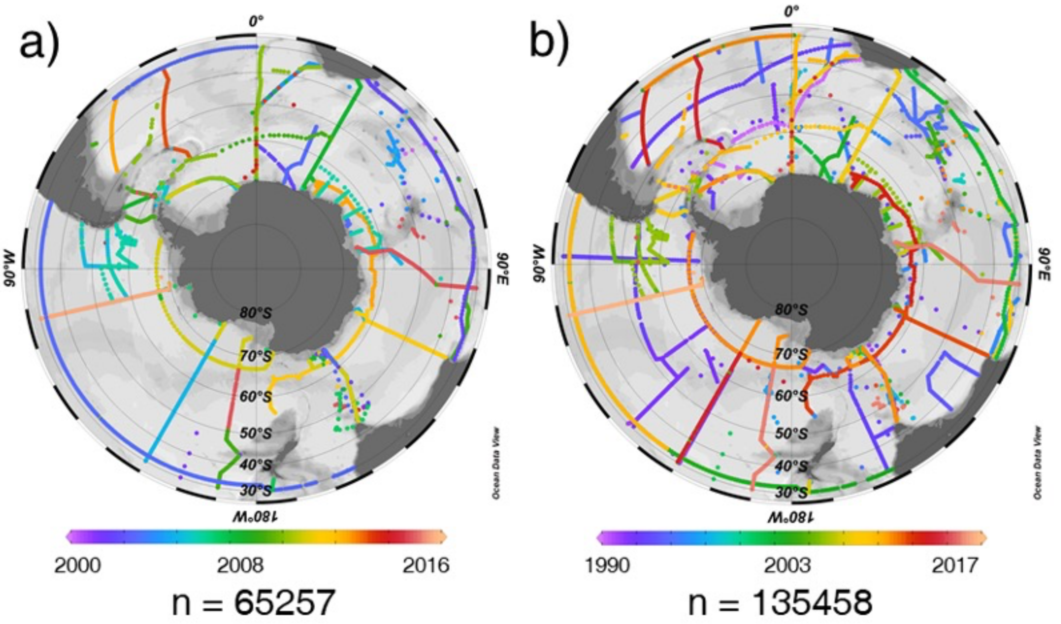

Fig. 2.1 Map of cruise data used in this study. The color shows the date of each cruise. The notation ‘n’ indicates the number of data points. (**a**) Cruise data during the period from 2000 to 2016 used for constructing the parameterization in this study. (b) Cruise data used for estimating ΔN_{ex}.

Fig. 2.2

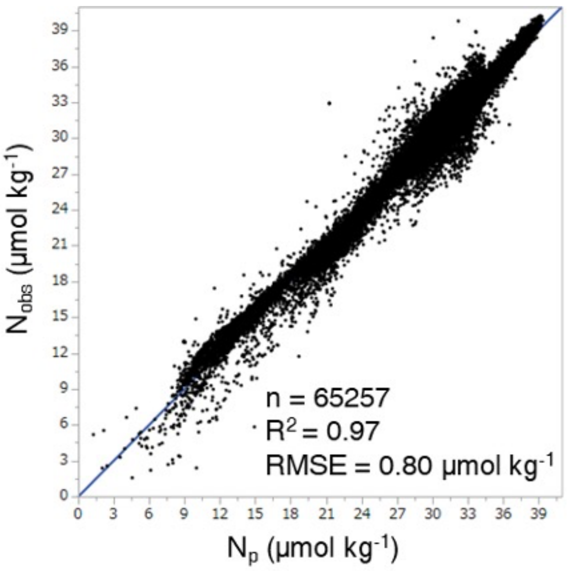

Fig. 2.2 Relationship between predicted nitrate (N_p) and observed nitrate (N_{obs}) from 0 – 6,000m south of 30°S during the period from 2000 to 2016 in the SO. The notation 'n' indicates the number of data points; R^2 indicates the coefficient of determination; RMSE indicates the root-mean-square error. The number of data used in the Pacific sector, Indian sector, and Atlantic sector are 29,391, 22,566, and 13,300, respectively. (Pacific Sector: 150° E–60°W; Indian Sector: 20°E–150°E; Atlantic Sector: 60°W–20°E).

Fig. 2.3

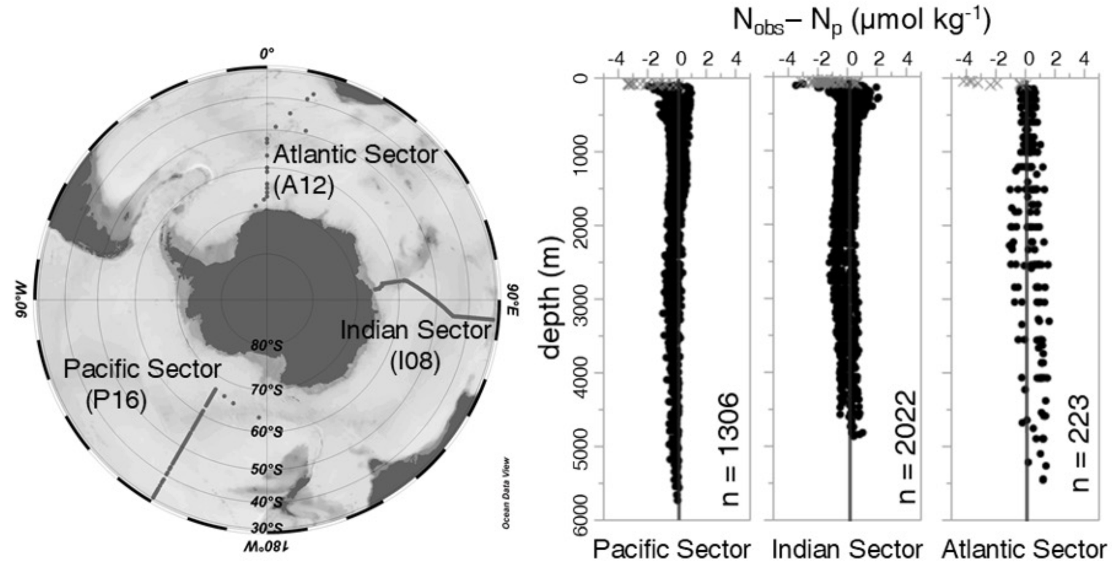

Fig. 2.3 The differences between N_{obs} and N_p ($N_{obs} - N_p$) for the data used in the three independent cruises; P16 (2014) for the Pacific sector; I08 (2007) for the Indian sector; A12 (2014) for the Atlantic sector. Grey crosses indicate data within 100 m from the surface.

Fig. 2.4

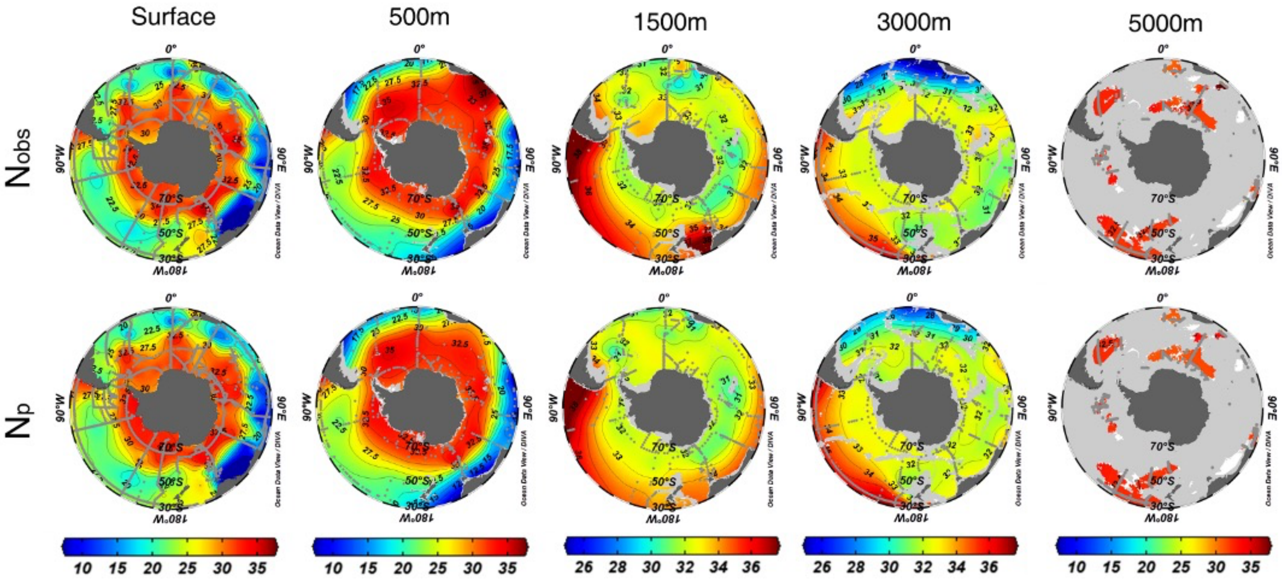

Fig. 2.4 Comparison between the distributions of N_{obs} (upper) and N_p (below) in the SO of 30°S south at surface (bottom of the mixed layer), 500 m, 1,500 m, 3,000m and 5,000m south of 30°S between 2000 and 2016. Color of the map shows the nitrate concentration in unit of μmol kg^{-1}. Gray dots show the position of observed data used for the parameterization.

Fig. 2.5

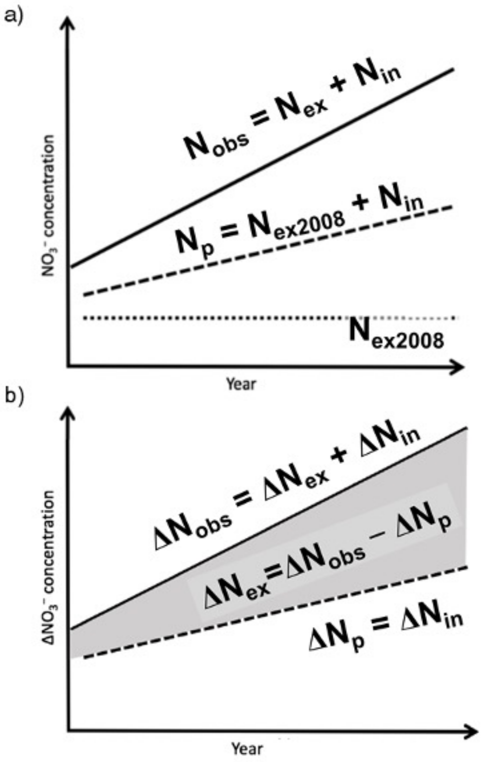

Fig. 2.5 Schematic illustrations of our method to estimate ΔN_{ex}. In (**a**), the solid line indicates the observed nitrate value (N_{obs}); the dashed line indicates the predicted nitrate value (N_p); the short-dashed line indicates the N_{ex} in 2008 (N_{ex2008}), which can be assumed to be a constant with time. In (**b**), the solid line indicates the change in N_{obs} (ΔN_{obs}) between arbitrary different years; the dashed line indicates the change in N_p (ΔN_p) between arbitrary different years; the shadow area shows the difference between ΔN_{obs} and ΔN_p, which is the change in N_{ex} (ΔN_{ex}) between arbitrary different years.

Fig. 2.6

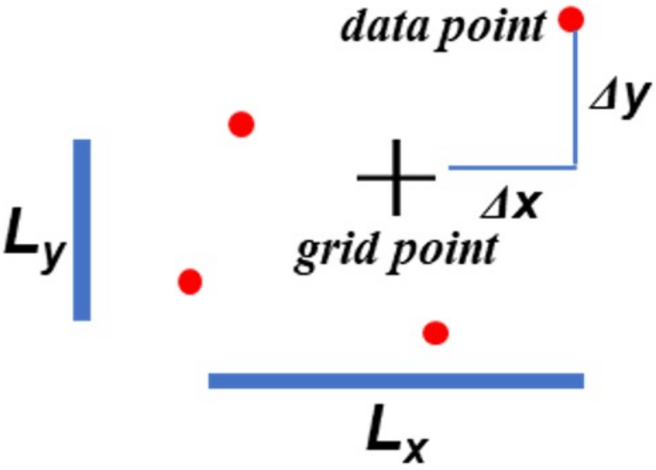

Fig. 2.6 Weighted averaging of data values at a grid point, redrawn based on ODV User’s Guide Version 5.2.0, Fig. 16-2.

Fig. 2.7

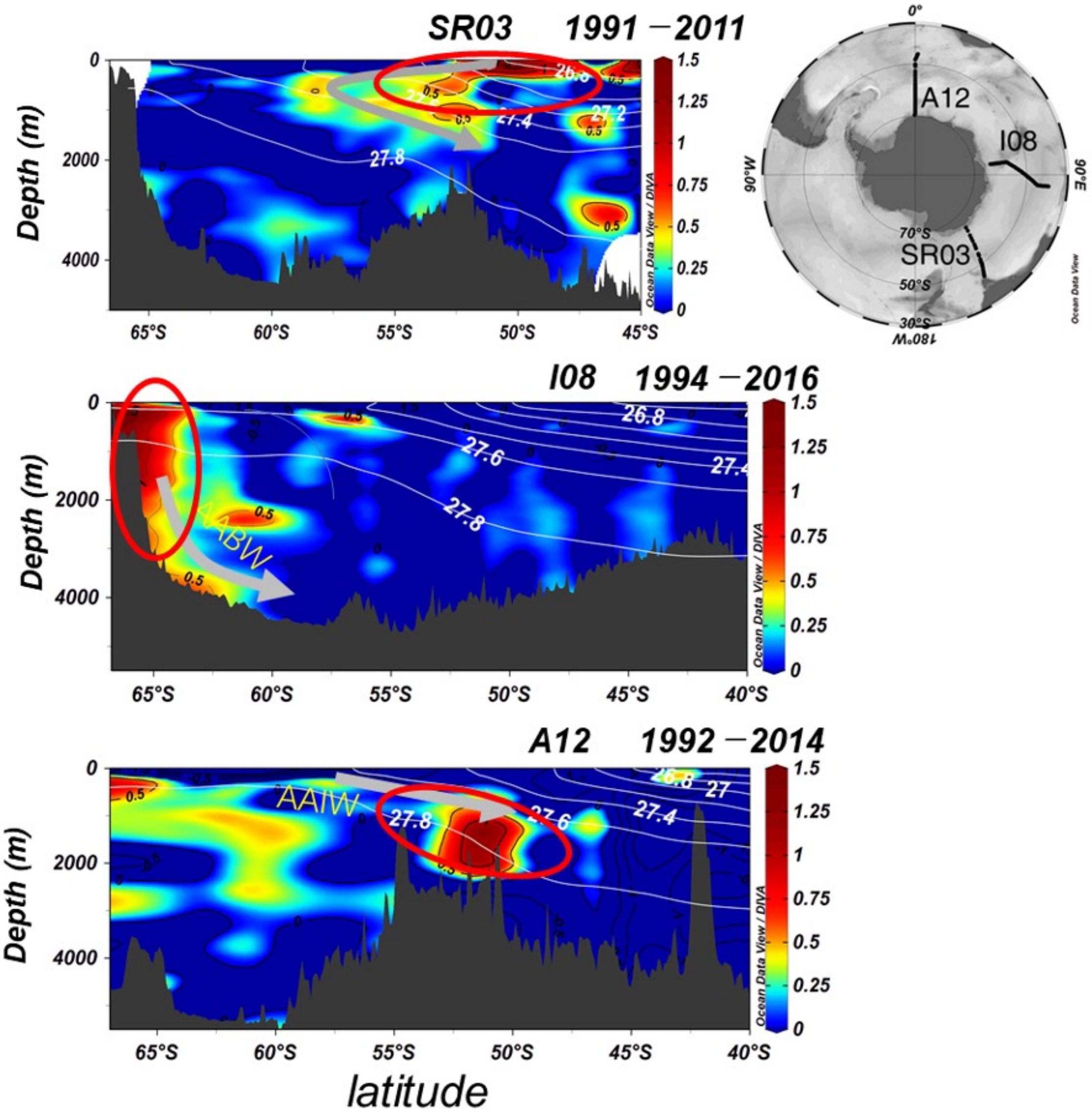

Fig. 2.7 Cross section distributions of ΔN_{ex} in SR03 (top), I08 (middle), and A16 (bottom) from the 1990s to the 2010s. White solid lines indicate the potential density of seawater. Grey arrows show the supposed trajectory of ΔN_{ex} inflow. Red circles emphasize the regions where N_{ex} increased remarkably.

Fig. 2.8

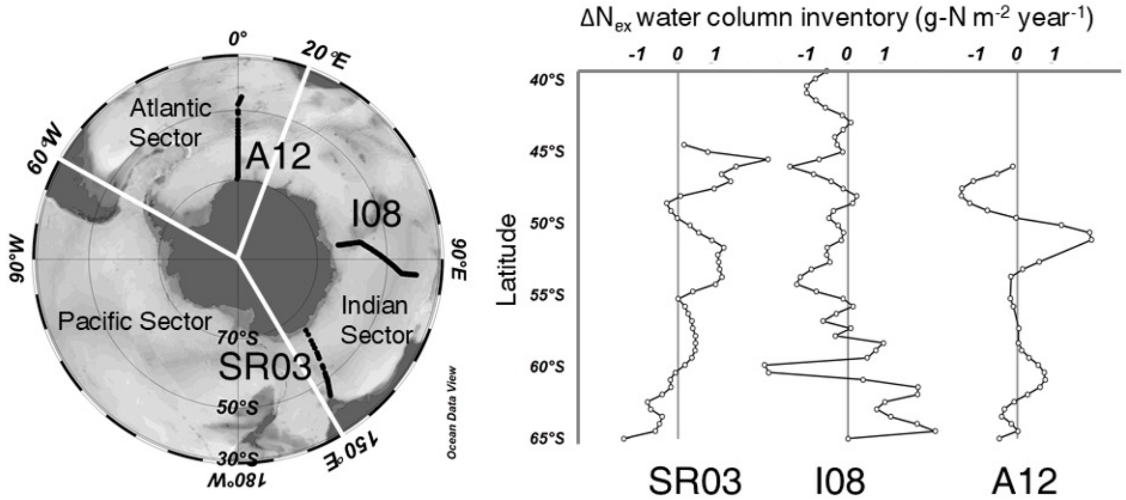

Fig. 2.8 Meridional distributions of water column inventory of ΔN_{ex} along three lines in the SO. SR03 (left, from 1991 to 2011), I08 (middle, from 1994 to 2016), and A12 (right, from 1992 to 2014), as the annual rate of water column inventory of **Δ**N_{ex} during the period from the 1990s to the 2010s, in units of g-N m^{-2} $year^{-1}$. The inventories were determined by integrating from the surface to the sea floor. White lines separate the three sectors of the SO (the Pacific sector, the Indian sector, and the Atlantic sector).

Fig. 2.9

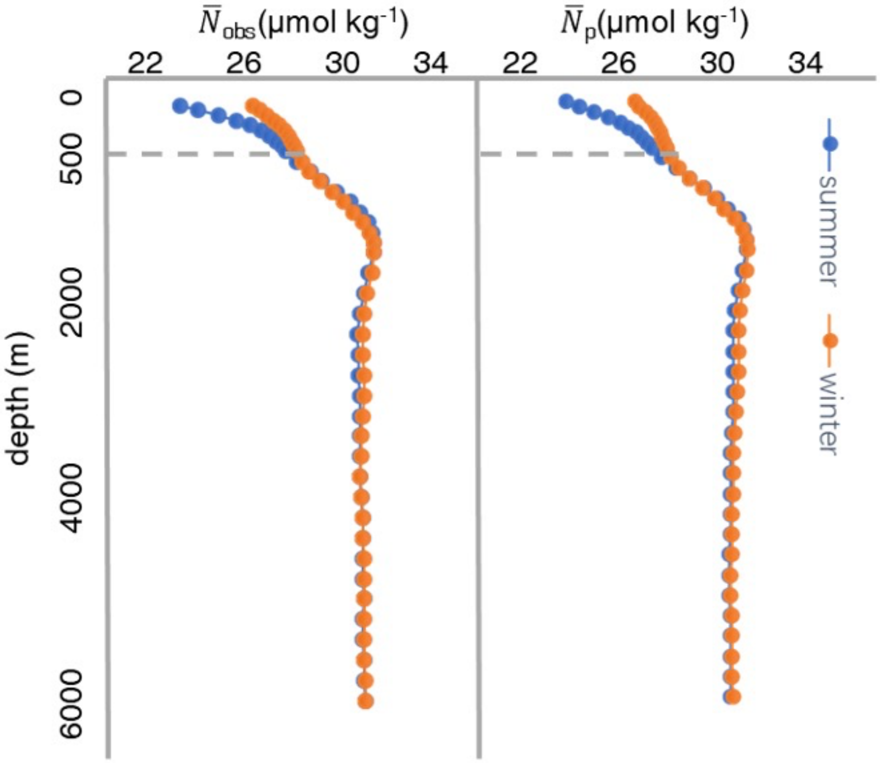

Fig. 2.9 Vertical distributions of average N_{obs} and N_p for summertime (blue circle) and wintertime (orange circle) based on the data from the 1990s to the 2010s south of 30°S. Differences between summertime and wintertime indicate seasonal variations.

Fig. 2.10

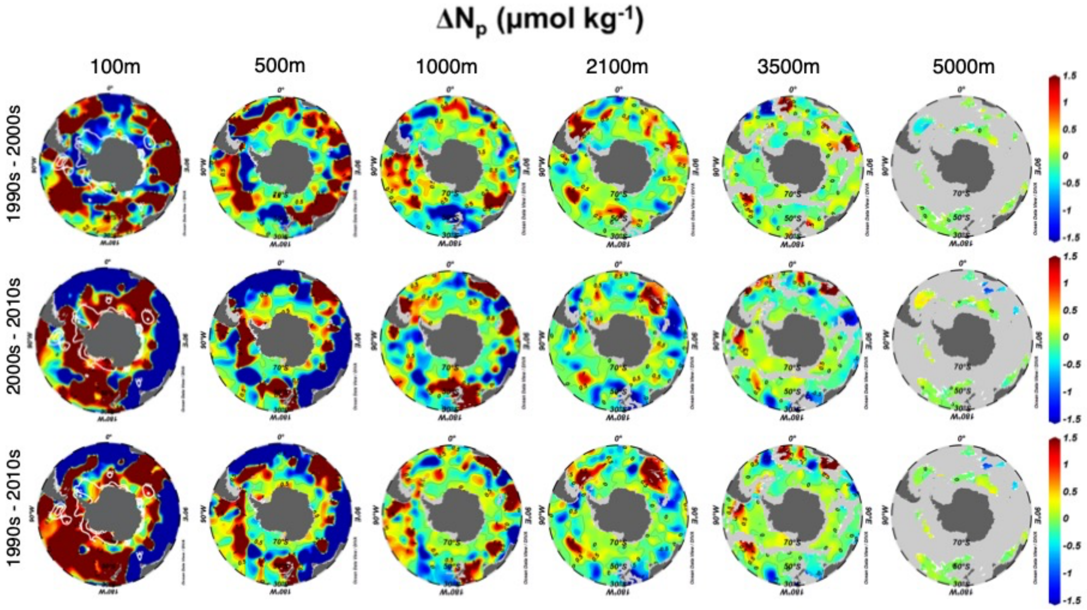

Fig. 2.10 Horizontal distributions of the decadal change in N_p in the SO. Shown were ΔN_p from the 1990s to the 2000s (top row), 2000s to 2010s (middle row), and 1990s to 2010s (bottom row) at different depths, in units of μmol kg^{-1}. Grey areas show the sea floors. White contour lines indicate the regions where the mixed layer is deeper than 100m.

Fig. 2.11

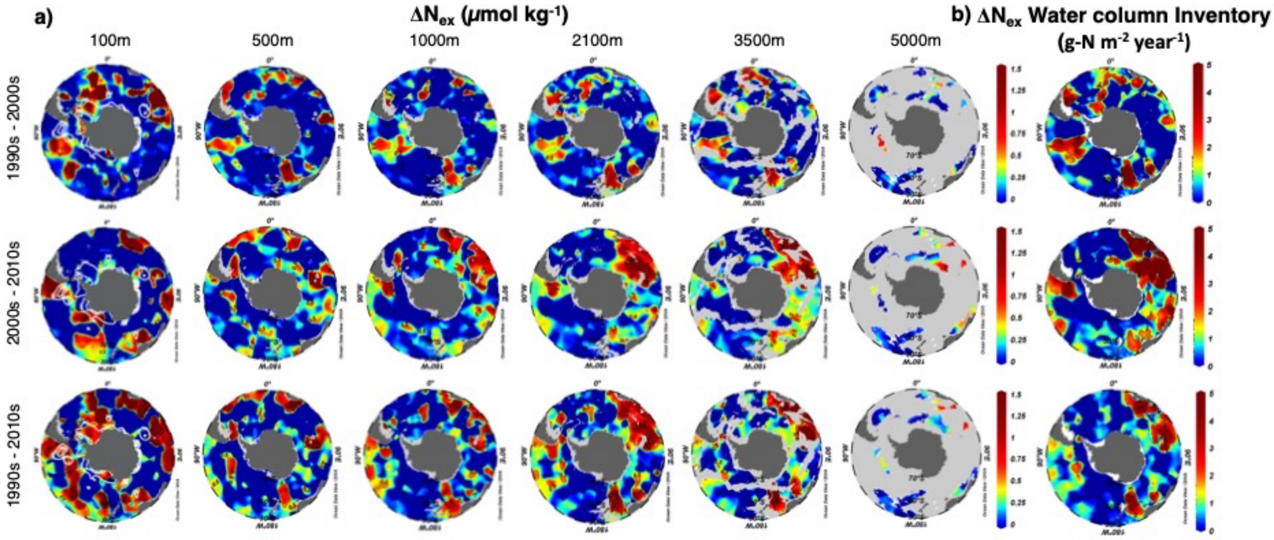

Fig. 2.11 Horizontal distributions of the decadal change in N_{ex} in the SO. Shown along with the annual rate of change in the SO south of 30°S. (**a**) The decadal change in N_{ex} during the period from the 1990s to the 2000s (top row), 2000s to 2010s (middle row), and 1990s to 2010s (bottom row) at different depths. Scale was fixed from 0 to 1.5 μmol kg^{-1} to emphasize the increase in N_{ex}. Grey areas show the sea floors. (**b**) Total water column inventories of ΔN_{ex} as the annual rate of change in N_{ex} over the same periods as in (a), in units of g-N m^{-2} year^{-1}. Inventories were determined by integrating ΔN_{ex} from the surface to the depth of 5,900m. White contour lines indicate the regions where the mixed layer is deeper than 100m.

Fig. 3.1

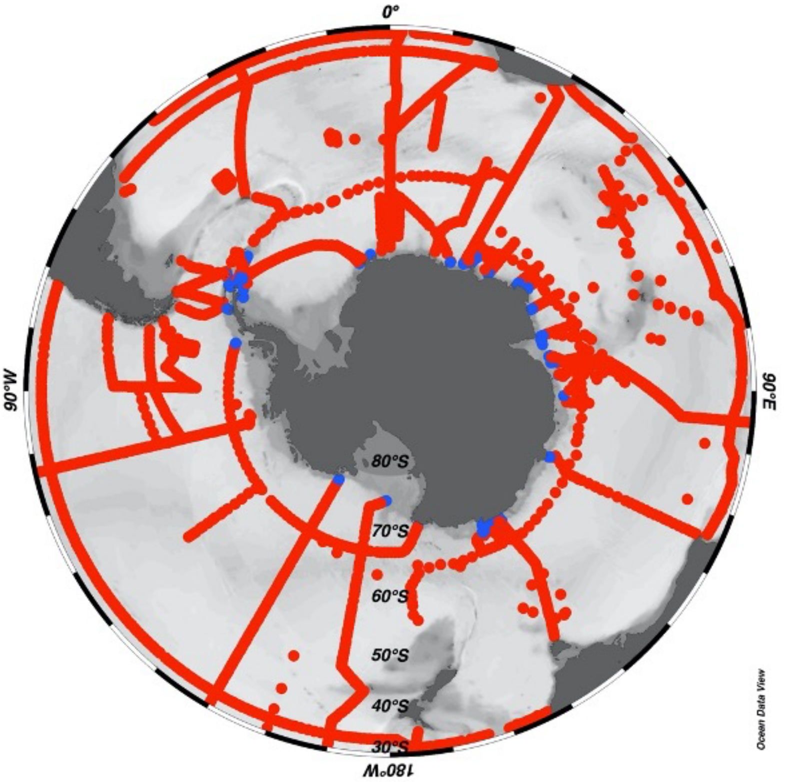

Fig. 3.1 Map of cruise data used for constructing DIC parameterizations. The data for DIC$_{open}$ and DIC$_{coastal}$ are shown by red and blue points, respectively. Data were obtained for the period of 2000 to 2017. This figure was drawn using *Ocean Data View 5.3.0 (https://odv.awi.de)*[44].

Fig. 3.2

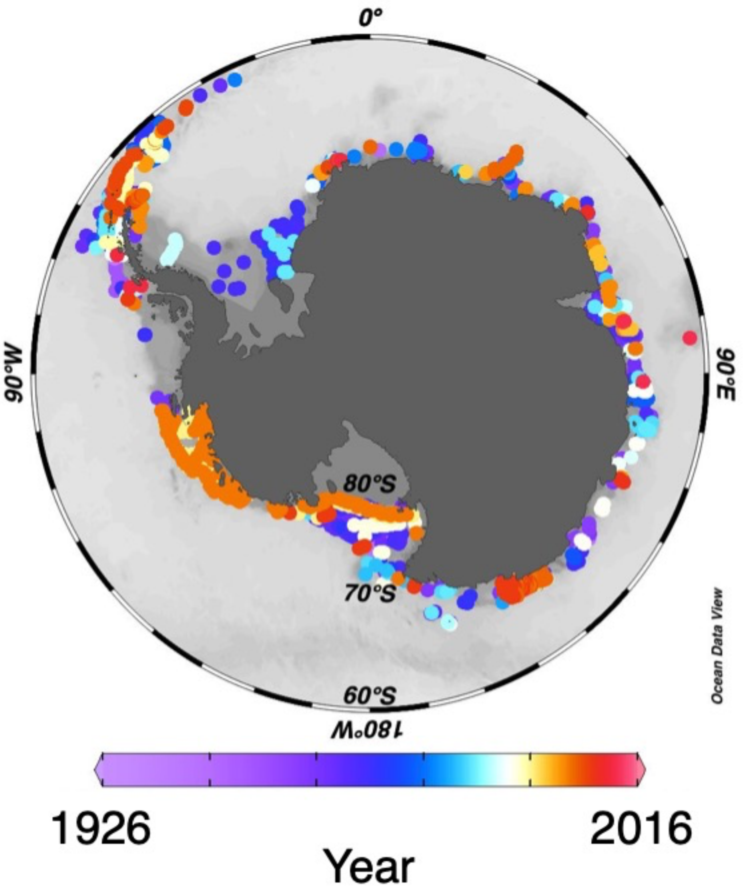

Fig. 3.2 Map of cruise data used for estimating the time-series of freshening in the SOc. Colour bar indicates the date of each cruise. This figure was drawn using *Ocean Data View 5.3.0 (https://odv.awi.de)* [44].

Fig. 3.3

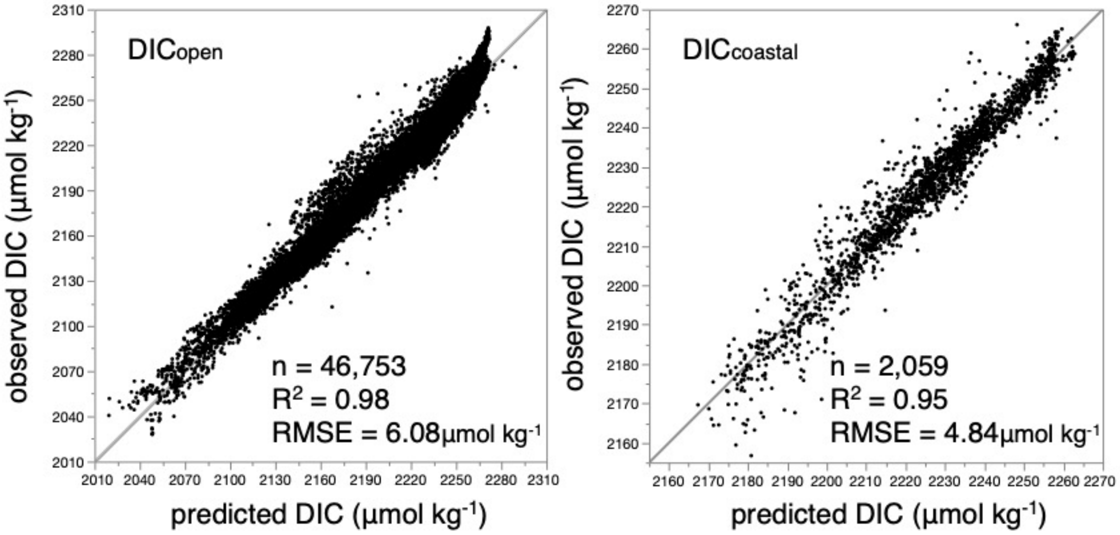

Fig. 3.3 Relationships between DIC_{pre} and DIC_{obs} in the open SO and the SOc. n indicates the number of data points; R^2 indicates the coefficient of determination; and RMSE indicates the root-mean-square error.

Fig. 3.4

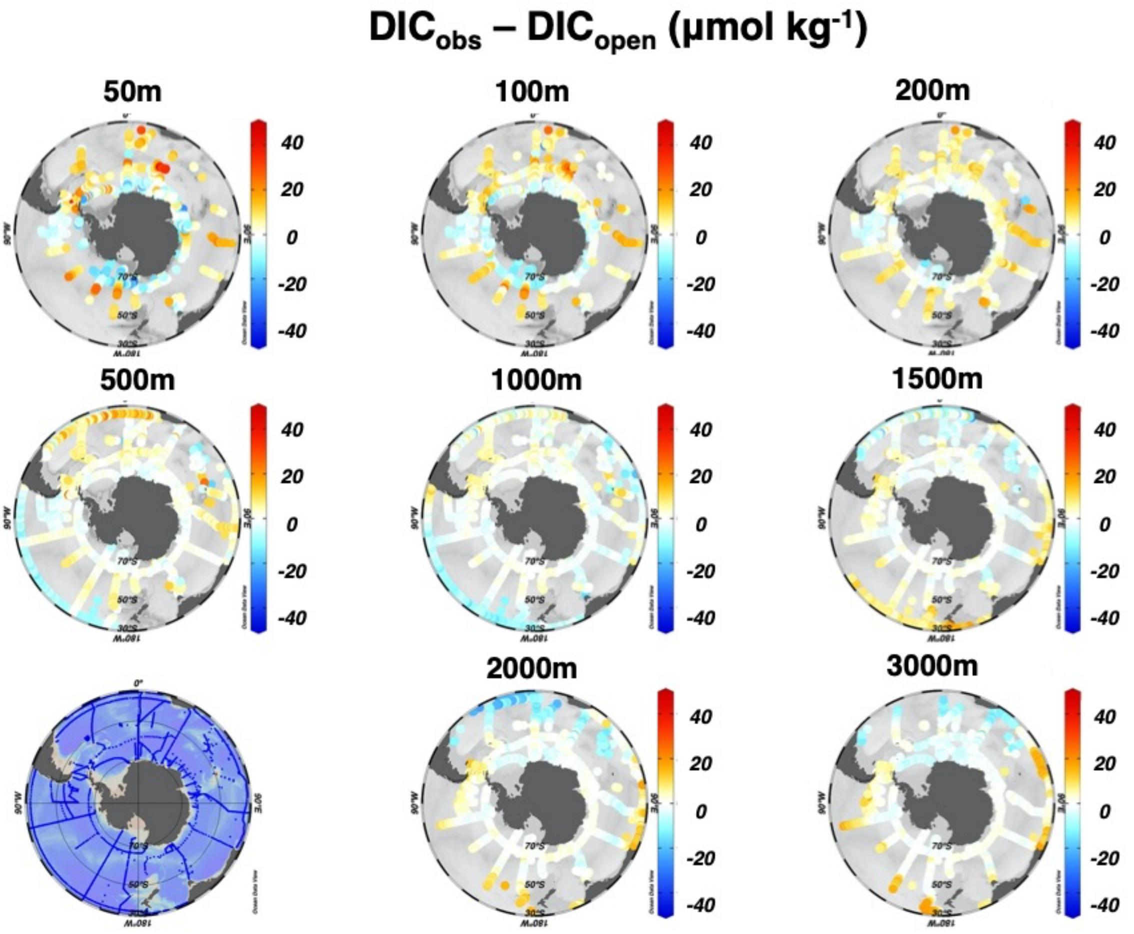

Fig. 3.4 Self-validation of DIC_{open}. Colours of data points indicate the differences between the observed DIC (DIC_{obs}) and the predicted DIC in the open SO (DIC_{open}). We showed these difference in several depths: 50, 100, 200, 500, 1000, 1500, 2000, and 3000 m. These figures were drawn using *Ocean Data View 5.3.0 (https://odv.awi.de)* [44].

Fig. 3.5

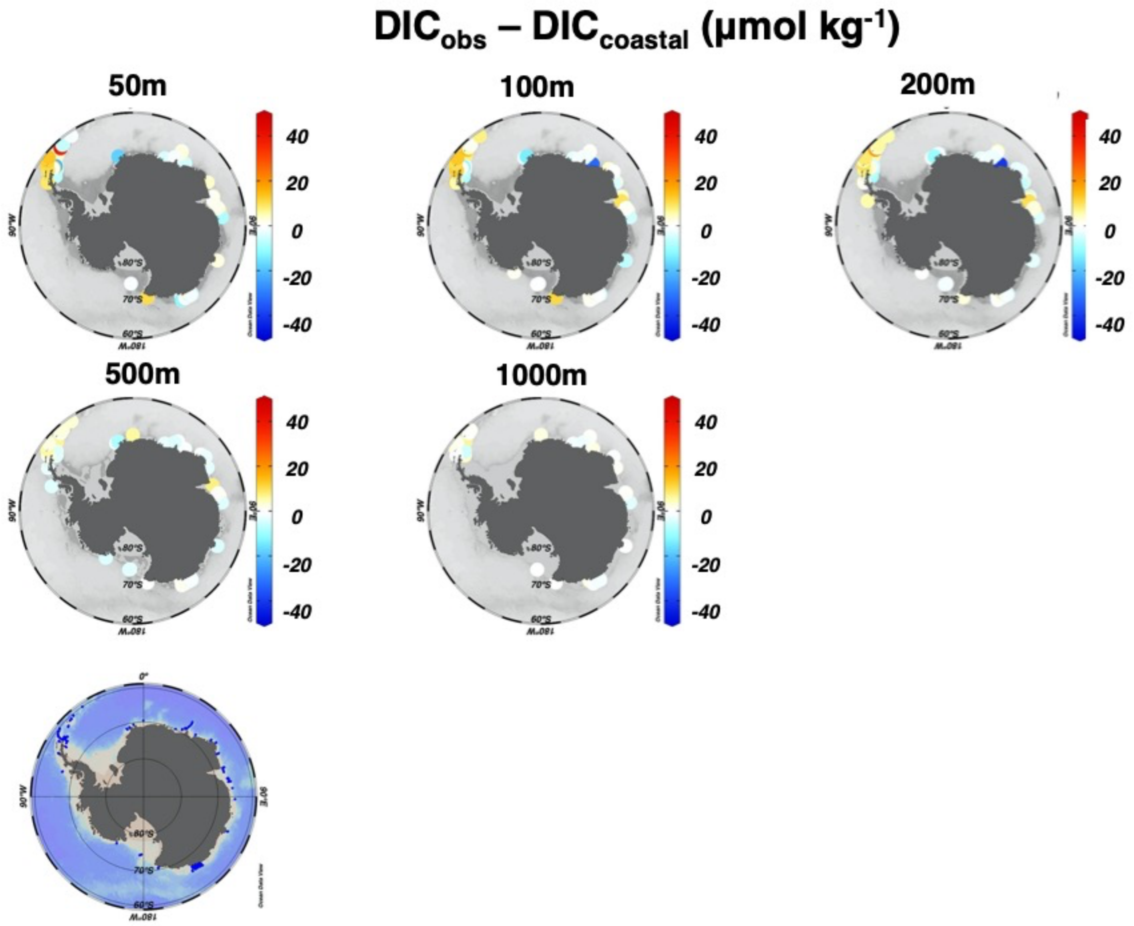

Fig. 3.5 Self-validation of DIC$_{coastal}$. Colours of data points indicate the differences between the observed DIC (DIC$_{obs}$) and predicted DIC in the SOc (DIC$_{coastal}$). We showed these difference in several depths: 50, 100, 200, 500, and 1000 m. These figures were drawn using *Ocean Data View 5.3.0 (https://odv.awi.de)* [44].

Fig. 3.6

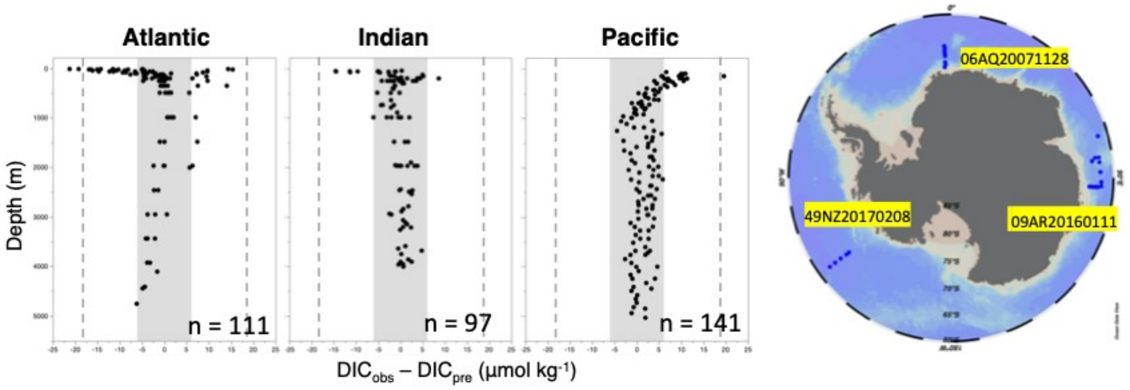

Fig. 3.6 Independent validation for open SO parameterization. Differences between $\mathrm{DIC_{obs}}$ and $\mathrm{DIC_{pre}}$ ($\mathrm{DIC_{obs}}$ – $\mathrm{DIC_{pre}}$) are calculated by using data from three independent cruises: 06AQ20071128 (Atlantic sector); 09AR20160111 (Indian sector); 49NZ20170208 (Pacific sector). Grey shadings indicate the range of ± 1 RMSE. Grey dashed lines indicate the range of ± 3 RMSE. The map on the right side shows the location of the three cruises. Map was drawn using *Ocean Data View 5.3.0 (https://odv.awi.de)* [44].

Fig. 3.7

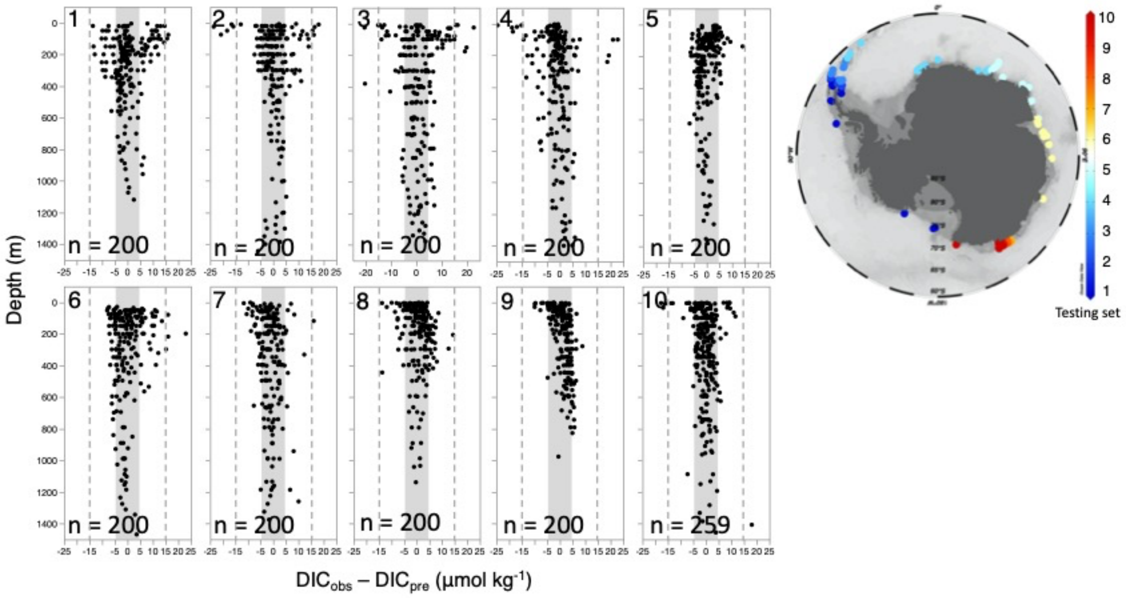

Fig. 3.7 *k*-fold cross-validation for SOc parameterization. We divided the observational data set in the SOc into 10 testing sets and conducted cross-validations 10 times [75,76]. Grey shadings indicate the range of ± 1 RMSE. Grey dashed lines indicate the range of ± 3 RMSE. The map in the right side shows the location of the testing sets with colour scale. Map was drawn using *Ocean Data View 5.3.0 (https://odv.awi.de)* [44].

Fig. 3.8

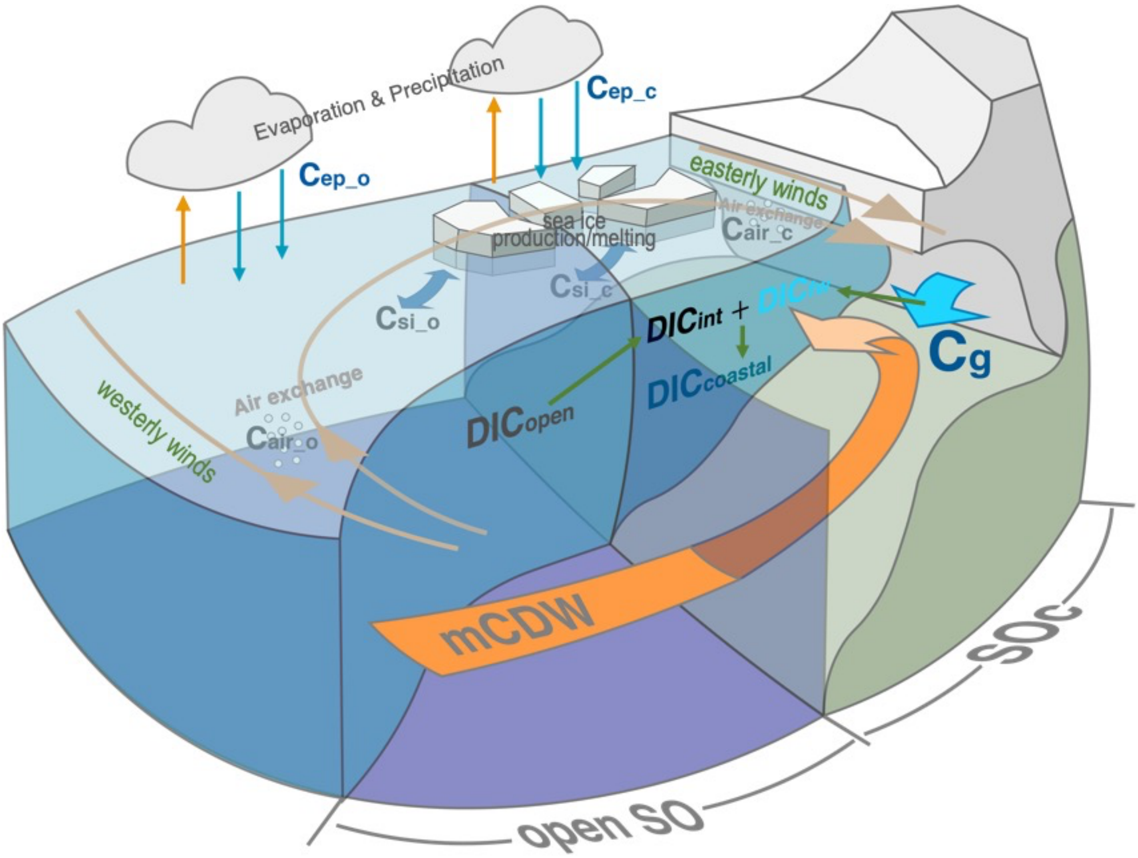

Fig. 3.8 Interactions among the open SO, SOc, and Antarctic glacier. Without any freshwater input from the Antarctic glacier, the initial seawater in the SOc entirely comes from the open SO with a DIC content of DIC_{int}. Warm modified CDW (mCDW) inflows from the open SO into the ice cavity southwardly, leading to ice shelf basal melt and freshwater release (with DIC = DIC_{fw}; shown by light blue arrows). The buoyant plume of freshwater together with mCDW rises to the surface. The mixture of freshwater and initial seawater makes the DIC concentration in the SOc become $DIC_{coastal}$. 'C' indicates the DIC components which is controlled by various external processes; subscripts 'o' and 'c' indicates processes of the open SO and the SOc, respectively; subscripts 'ep', 'si', 'air' and 'g' indicates evaporation & precipitation, sea ice, air-sea exchange, and glacier melting, respectively.

Fig. 3.9

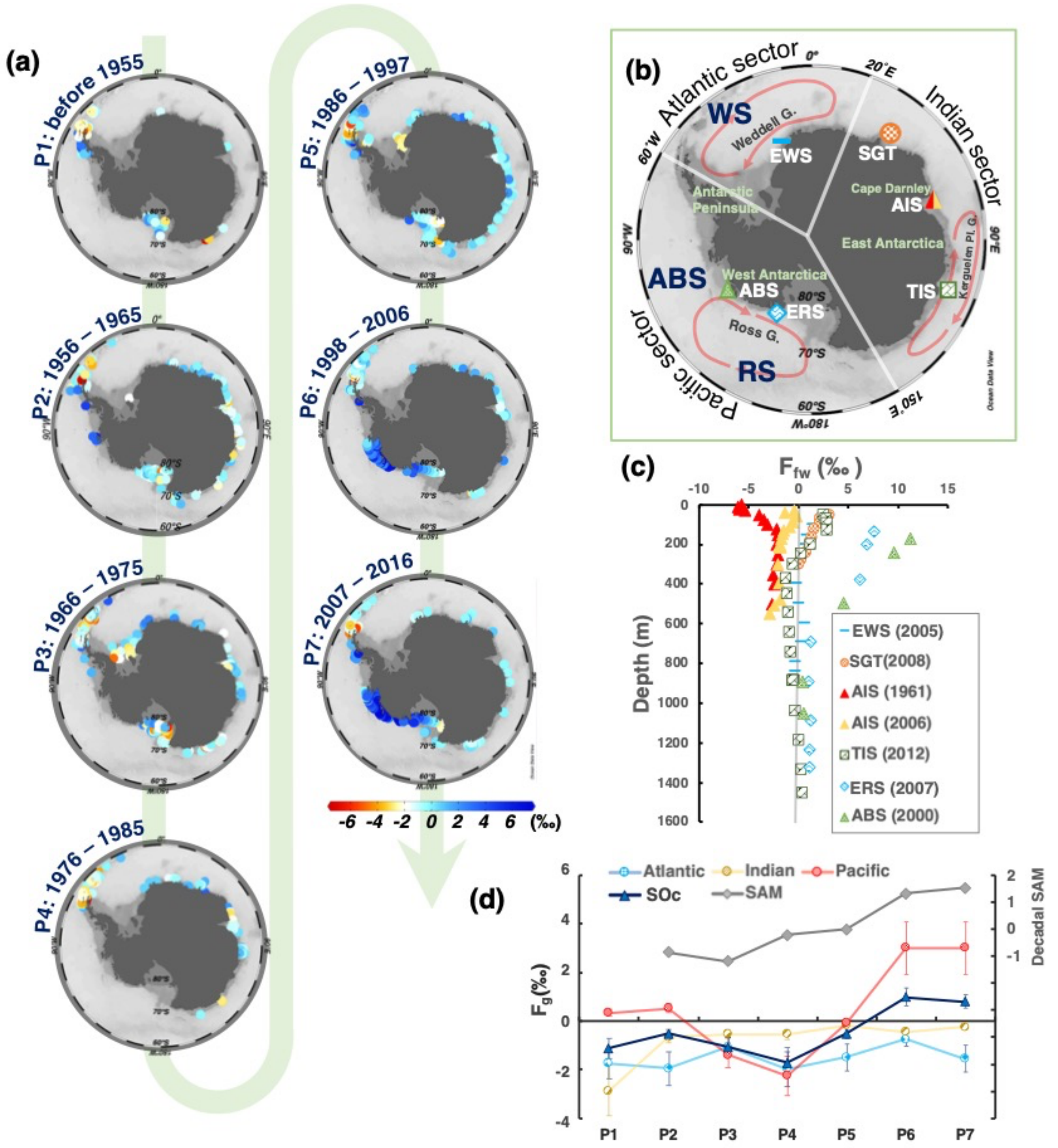

Fig. 3.9 Distributions of glacier-derived freshening over the SOc during 1926–2016. Freshening is represented by the fraction of melt freshwater (F_g, ‰). Positive values indicate freshwater released from the glacier into the SOc, strengthening the freshening. **(a)** Spatiotemporal distributions of freshening over the SOc. Values are shown as the average F_g in the vertical water column. **(b)** Map of the Antarctic and the SO south of 60° S. White lines separate the three sectors of the SOc (Atlantic Sector: 60° W–20° E; Indian Sector: 20° E–150° E; Pacific Sector: 150° E–60° W). Blue abbreviations indicate the following seas: WS, Weddell Sea; RS, Ross Sea; ABS, Amundsen, and Bellingshausen Sea. White abbreviations indicate the stations in

(c); EWS, Eastern Weddell Sea; SGT, Shirase Glacier Tongue; AIS, Amery Ice Shelf; TIS, Totten Ice Shelf; ERS, Eastern Ross Sea; ABS, Amundsen, and Bellingshausen Seas. **(c)** Vertical distribution of F_g in several stations shown in (b) (white abbreviations with symbols). **(d)** Decadal changes of F_g in the three sectors and the entire SOc during 1926–2016 (left axis). Error bars show the uncertainty of 36% derived from the propagation of error. The grey line indicates the decadal change of the Southern Annular Mode (SAM, right axis) [86]. Maps in this figure were drawn using *Ocean Data View 5.3.0 (https://odv.awi.de)* [44].

Fig. 3.10

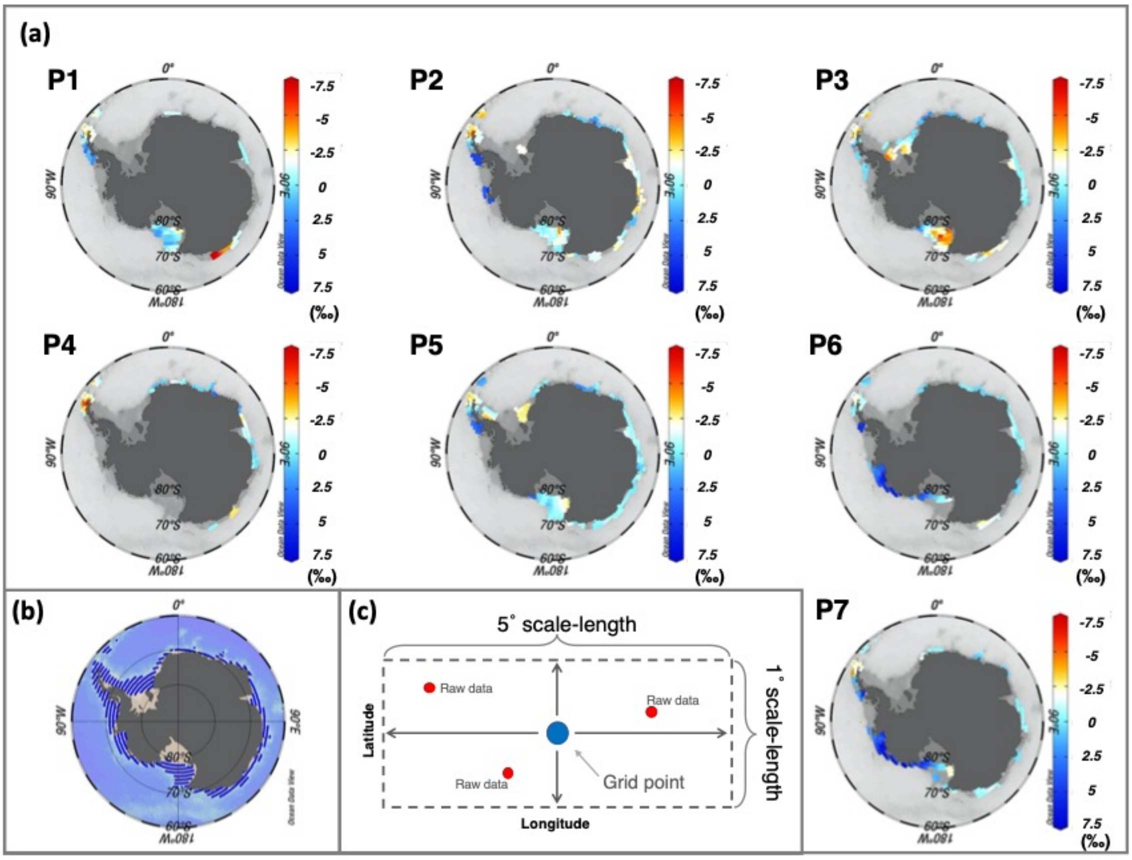

Fig. 3.10 Gridded data used to calculate the average F_g in each sector of the SOc. (a) Distributions of the gridded data during each period, which are interpolated from the raw data shown in Fig. 3.9a. **(b)** Map of the 1° x 1° grid used for interpolation. **(c)** Schematic of the interpolation algorithm used in this study. Here, we used the "weighted-average gridding" method given by Ocean Data View to perform the interpolation. Blue circle indicates the grid point and red circles indicate raw data. All raw data within a given range (gray dash line box) around one grid point were used to calculate the value on this grid point. The range here was set to be 5 degrees of longitude and 1 degree of latitude. See the user guide of Ocean Data View for detail. These figures were partly drawn using *Ocean Data View 5.3.0 (https://odv.awi.de)* [7].

Fig. 3.11

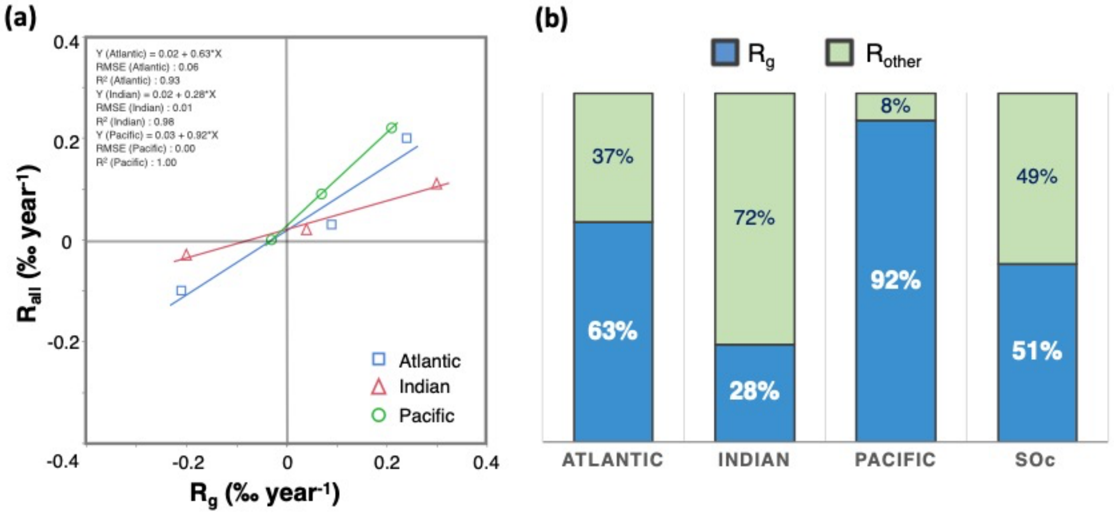

Fig. 3.11 Impact of glacier melting on the SOc. (a) Correlations between the rate of glacier-derived freshening (R_g) and overall freshening (R_{all}) in the SOc during 1960 ~ 2016. Blue open squares, red open triangles, and green open circles indicate data picked up from Atlantic, Indian and Pacific sectors of SOc, respectively. Solid lines are the correlation lines of each sector. Data used to plot this figure are given in Table 3.6. **(b)** Proportion of the rate of glacier-derived freshening (R_g, shown in blue) and freshening derived from other external processes (i.e. evaporation & precipitation and sea ice) (R_{other}, shown in green) in each sector and the entire SOc.

Fig. 3.12

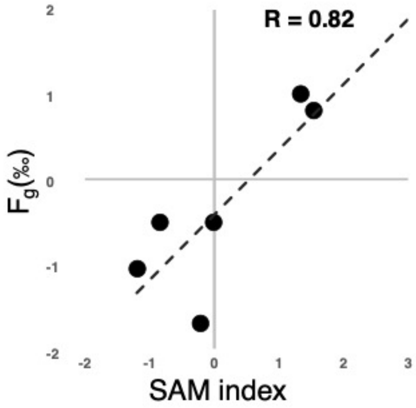

Fig. 3.12 Correlation of melt freshwater fraction in the SOc with SAM index. The dashed line indicates the regression line (c.f. Fig. 3.9d).

Fig. 3.13

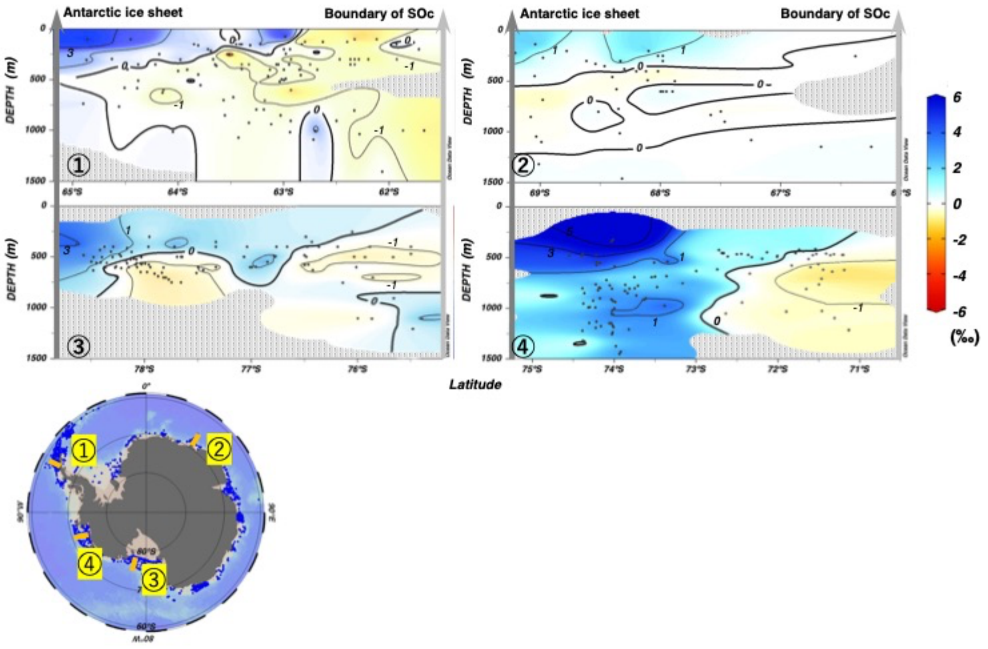

Fig. 3.13 Four north-south vertical sections of the freshwater fraction (F_g) estimated by this study around SOc. The positions of these sections are shown by orange lines in the lower left map. Data are used during the whole estimation period in this study (1926–2016). Black dots indicate data points. Bold solid lines indicate the contour of F_g equals to zero. Gray shadings indicate no observational data. Left side of each section is the Antarctic ice sheet. Right side of each section is the boundary of SOc, which indicates the location closest to the 1,500 m bottom depth where has observational data. F_g at the surface gradually decreases with increasing distance from the Antarctic ice sheet and decreases to nearly zero before reaching the boundary of SOc. For easy viewing, the bathymetries are not shown in these sections. These figures were drawn using *Ocean Data View 5.3.0 (https://odv.awi.de)* [44].

Fig. 4.1

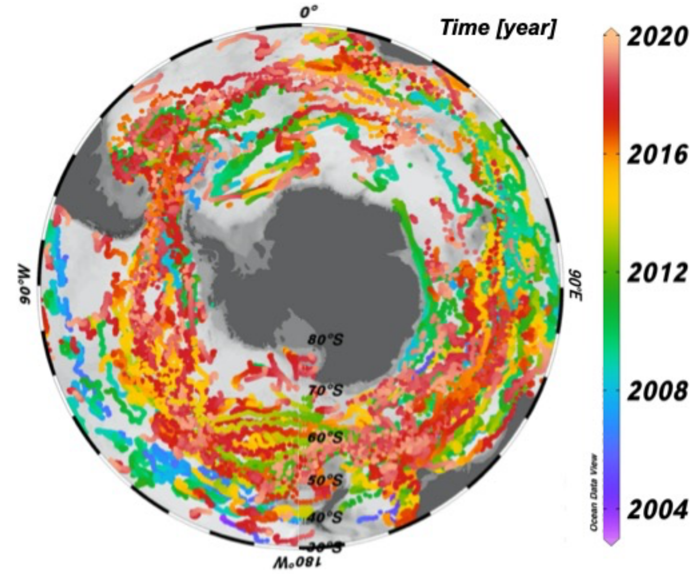

Fig. 4.1 BGC-Argo trajectories in the SO with trajectories in different years are depicted by colored dots from 2004 to 2019. The number of BGC-Argo is 154, with 27,039 vertical profiles. BGC-Argo: biogeochemical Argo float. This figure was drawn using Ocean Data View[44].

Fig. 4.2

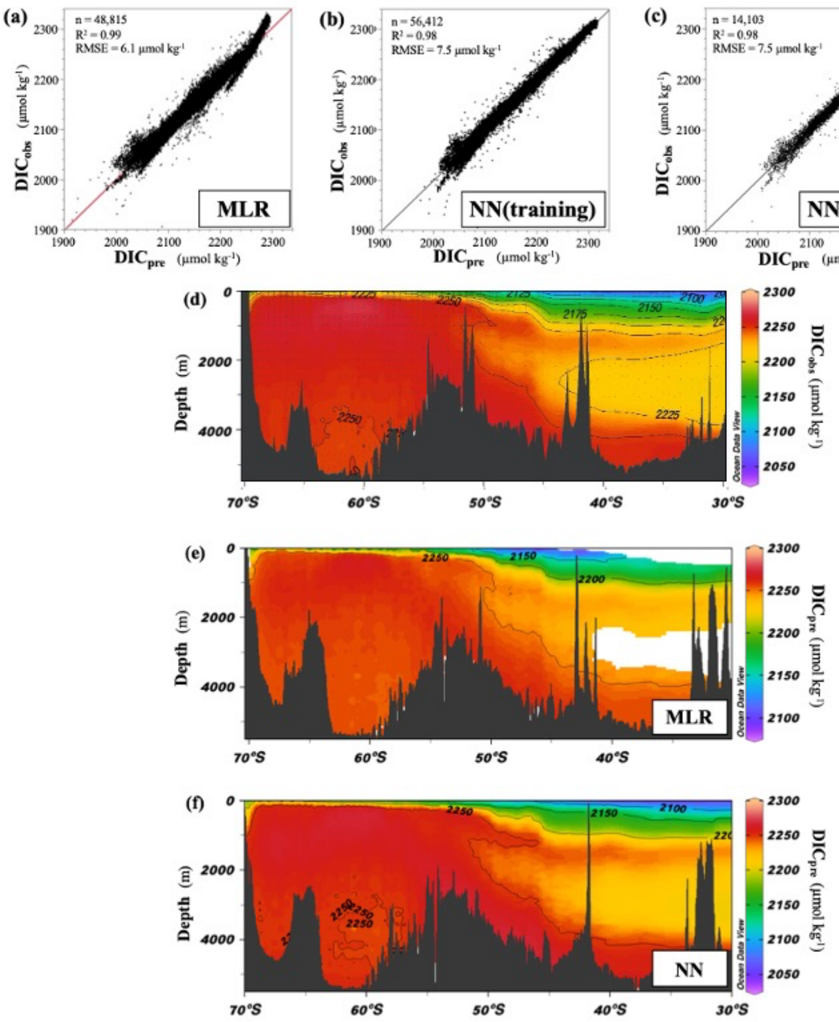

Fig. 4.2 Relationship between predicted (DIC_{pre}) (μmol kg^{-1}) and observed DIC (DIC_{obs}) (μmol kg^{-1}) from 0–6000 m in the SO. (a) DIC_{pre} of MLR versus DIC_{obs}. (b) DIC_{pre} of NN with training dataset versus DIC_{obs}, where “training dataset” means the dataset used to train NN for reconstructing DIC. (c) Same as (b), but DIC_{pre} of NN with testing, where “testing” means the dataset used to validate the result of NN training. (d) The vertical section of DIC_{obs} (μmol kg^{-1}) from 0–6000 m in the Atlantic sector of SO. (e) The vertical section of DIC_{pre} by the MLR method from 0–6000 m in the Atlantic sector of SO. The white areas in this figure indicate the areas where DIC cannot be reconstructed due to the constraints of the MLR method. (f) The vertical section of DIC_{pre} by the NN method from 0–6000 m in the Atlantic sector of SO. The notation “n” indicates the number of data points; R^2 indicates the coefficient of determination; RMSE indicates the root mean square error.

Fig. 4.3

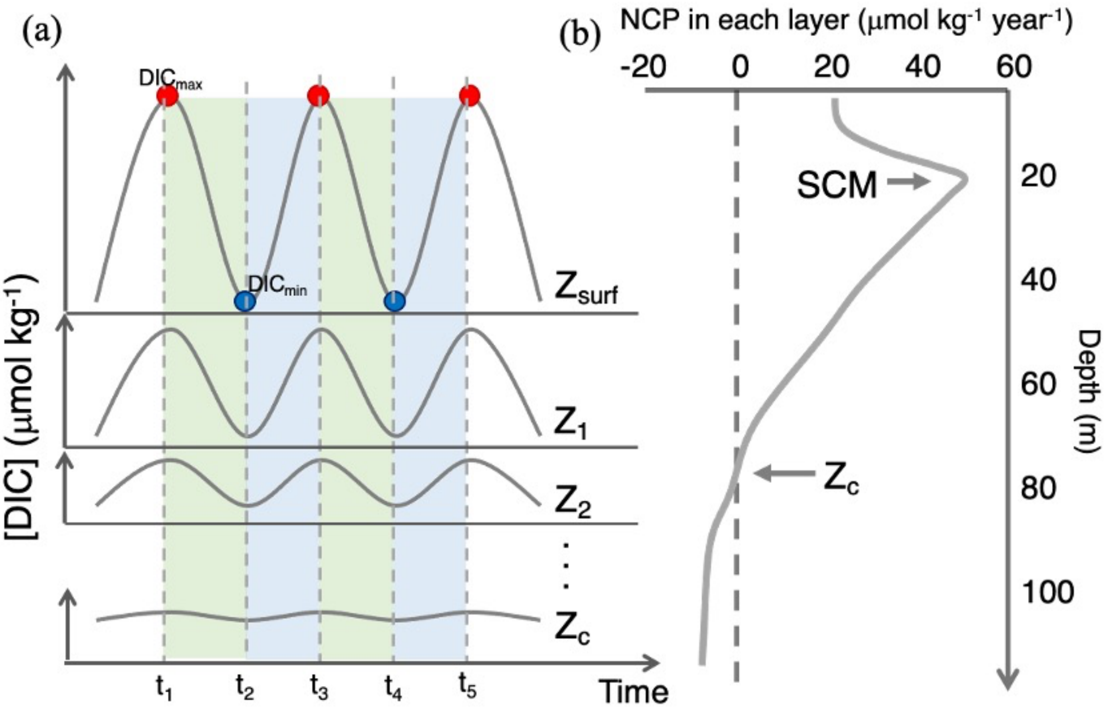

Fig. 4.3 Schematic figures for the definition of DE and RES in this study. (a) Time series of DIC concentration (DIC) in each standard layer. Z_{surf} indicates the surface depth, Z_1, Z_2 indicate deeper standardized depth determined in Supplementary text A1, and Z_c indicates the critical depth. The maximum and minimal values of the DIC cyclical variation in each layer are referred to as DIC_{max} and DIC_{min}, depicted by red and blue points. DE in each layer is defined as the decrease from DIC_{max} to DIC_{min}. (b) The vertical profiles of DE (regarded as NCP in this figure) in each layer. Z_c is defined as the depth where DE becomes zero or the minimal value. The SCM is also marked in this figure.

Fig.4.4

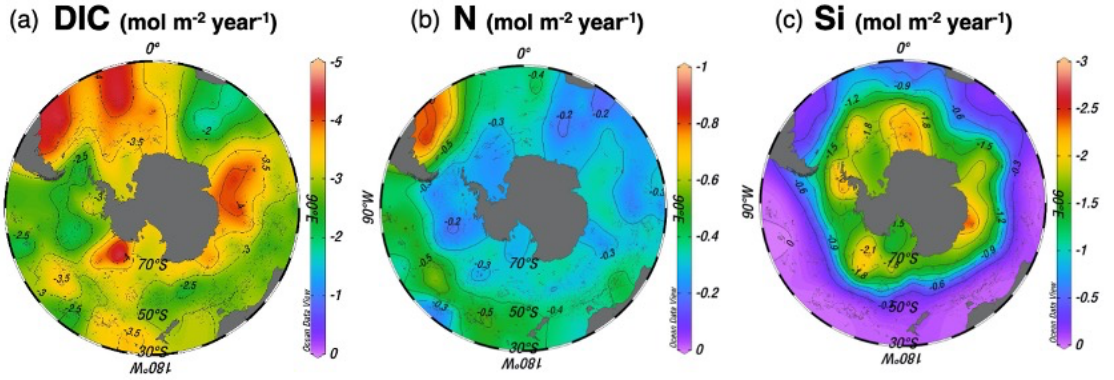

Fig. 4.4 Distribution of DE (mol-C m^{-2} year^{-1}) of (a) DIC, (b) N and (c) Si over the SO. Data from 154 BGC-Argo during 2004 – 2019. DE is shown in negative value in these figures. Black dots indicate the observed data points through the BGC-Argo trajectories during the biological production period. These figures were drawn using Ocean Data View[50].

Fig. 4.5

(a) Downward export between each front

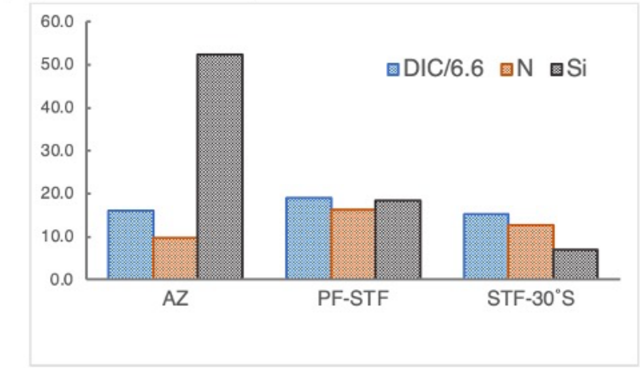

(b) Downward export in each sector

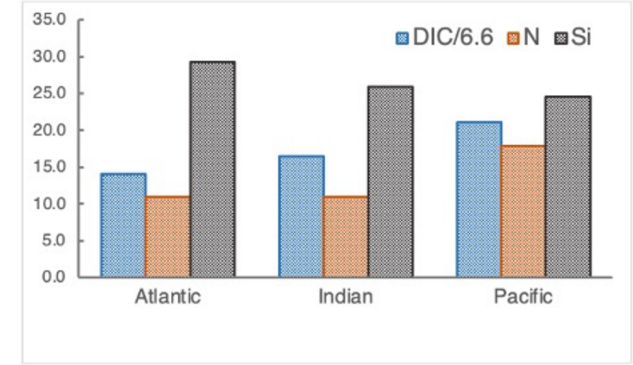

(c)

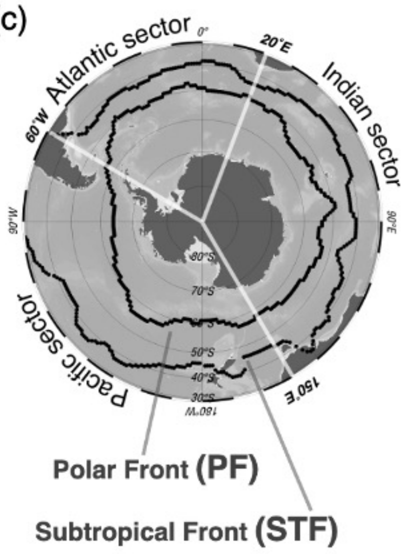

Fig. 4.5 Total DE (tDE, Tmol year^{-1}) for each front zone and sector in the SO. (a) tDE of DIC, N and Si in each front zone. (b) tDE of DIC, N and Si in each sector. (c) Map of the three front zones and three sectors of the SO. Front zones are divided by the Subtropical (STF) and the Polar Front (PF). Sectors are defined as the Indian (20° E –150° E), Pacific (150° E–60° W), and the Atlantic sector (60° W–20° E). DIC is shown as the value divided by the Redfield ratio of carbon and oxygen.

Fig. 4.6

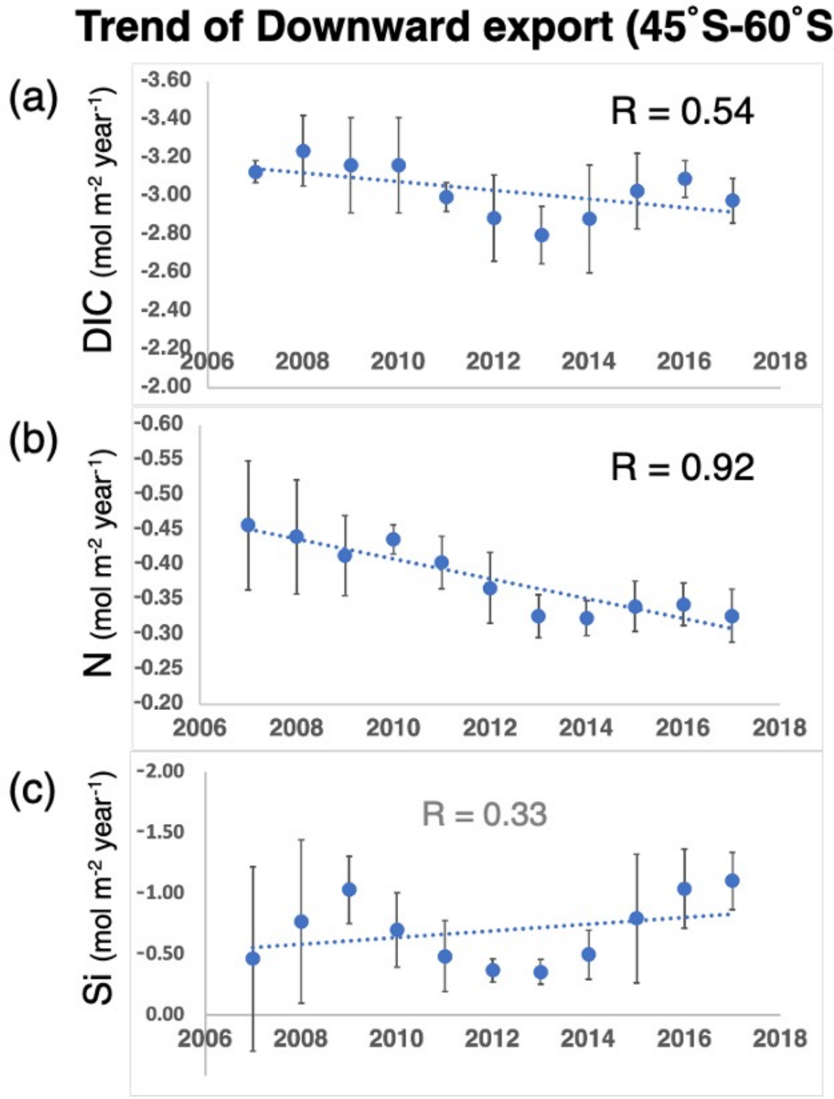

Fig. 4.6 Time-series of Downward export of (a) DIC, (b) N and (c) Si from 2007 to 2017 in the SO. The time series are calculated by 3 years running mean. Data used to estimate the time-series are depicted in Fig. 4.7. Dash lines are the regression line of each time series. Error bars show the standard deviation of the 3 years running mean. R is the correlation coefficient.

Fig. 4.7

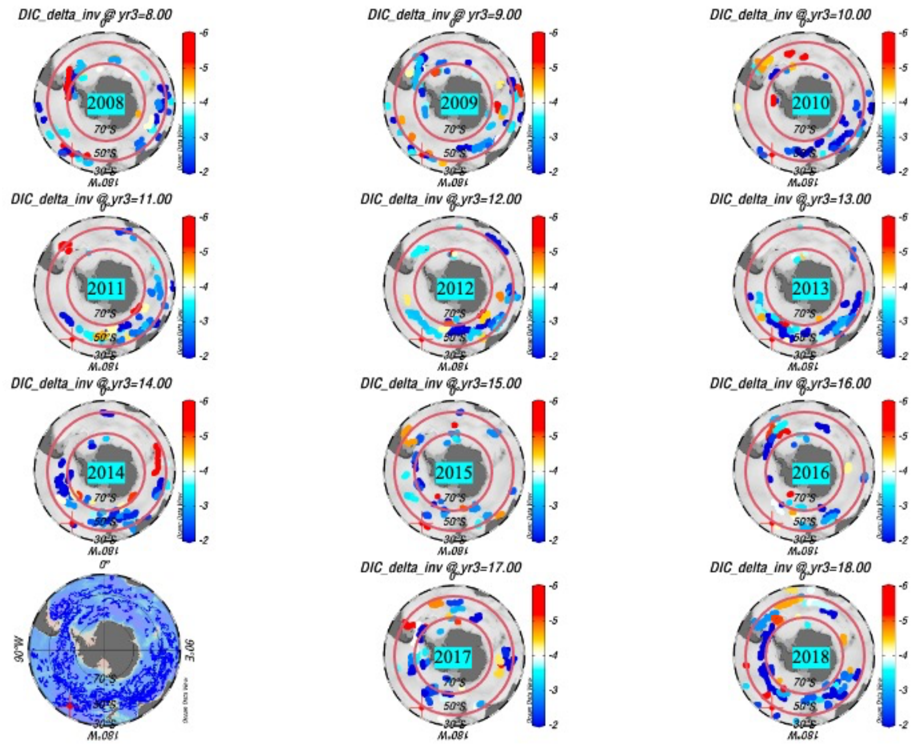

Fig. 4.7 Location and value of DE data in the SO from 2008 to 2018 (mol-C m^{-2} year^{-1}). The number of all DE estimated in this study is 484, and color dots indicate the observed BGC-Argo trajectories during the biological production period. Data distribution of each year. Because the data from 2008 to 2018 are distributed throughout the SO, and the BGC-Argo are mostly concentrated between the red circles (45˚S to 60˚S), we used the data between the red circles during 2008 to 2018 to obtain the NCP and RES time-series over the SO (Fig. 4.6a). These figures are drawn using Ocean Data View[44].

Fig. 5.1

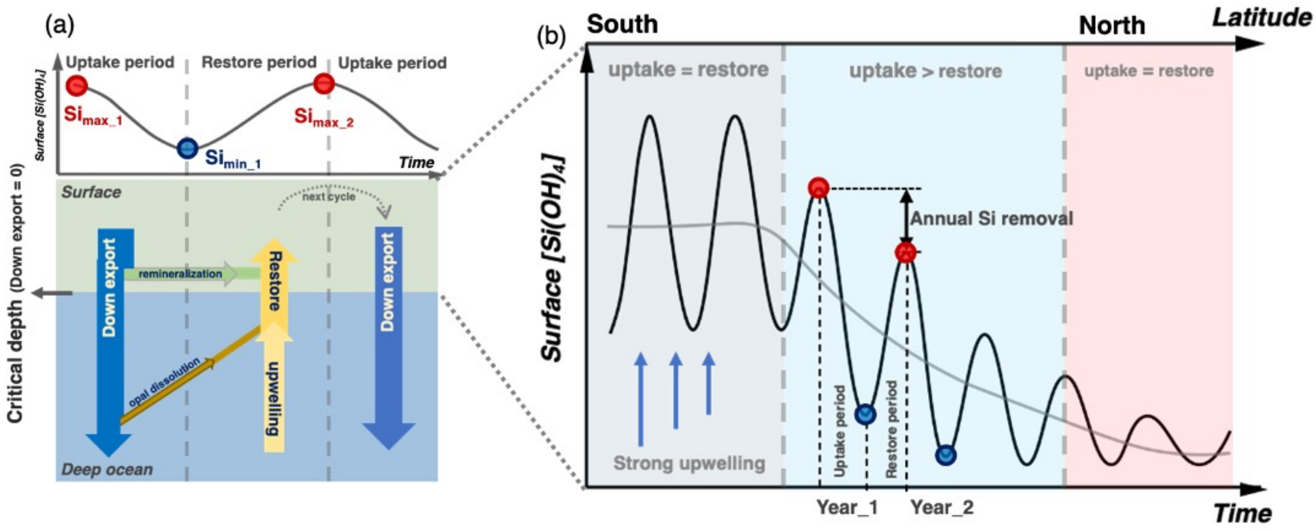

Fig. 5.1 Schematic of the nutrient dynamics in the ocean, here uses Si as an example. (a) Si cycle between the surface and the deep ocean. One year is separated into two periods. The uptake period when the surface Si concentration decrease, and the restore period when the surface Si concentration increase. Red point shows the Si concentration maximum ($\mathrm{Si}_{\mathrm{max}}$) and blue point shows the Si concentration minimum ($\mathrm{Si}_{\mathrm{min}}$). (b) Change of Si concentration in the surface layer with the movement of water mass from south to north. The unbalance between the decreasing and the increasing of Si is defined as annual Si removal, which indicates the net removal of Si from the surface layer.

Fig. 5.2

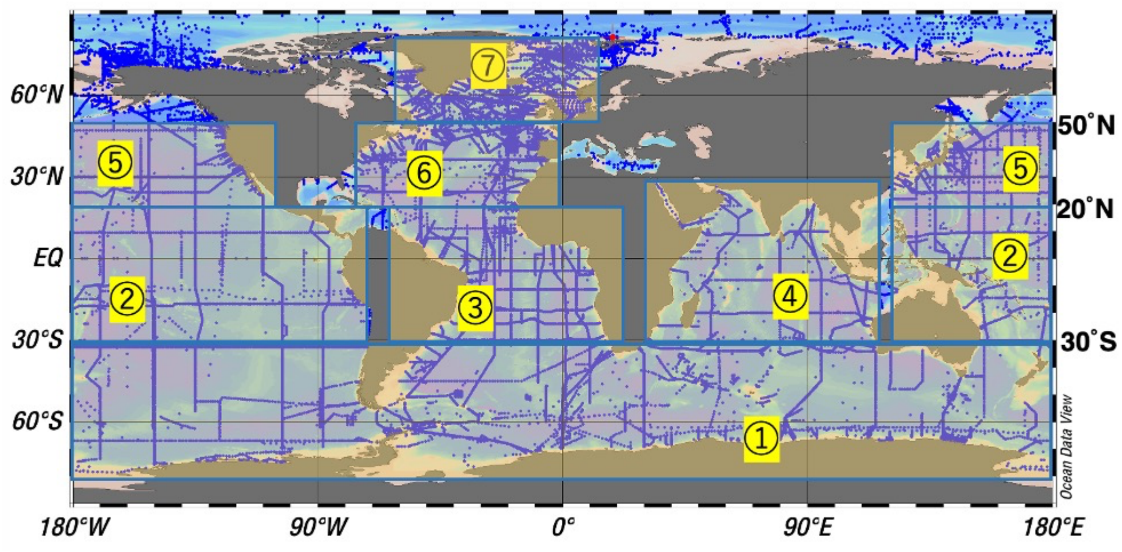

Fig. 5.2 Observed data used to construct parameterizations of Si and N over the global ocean. Here, the global ocean is divided into seven regions: 1, SO; 2, Equatorial Pacific; 3, Equatorial Atlantic; 4, Northern Indian Ocean; 5, North Pacific; 6, North Atlantic; 7, Subarctic Atlantic. Data are sourced from GLODAP_v2.

Fig. 5.3

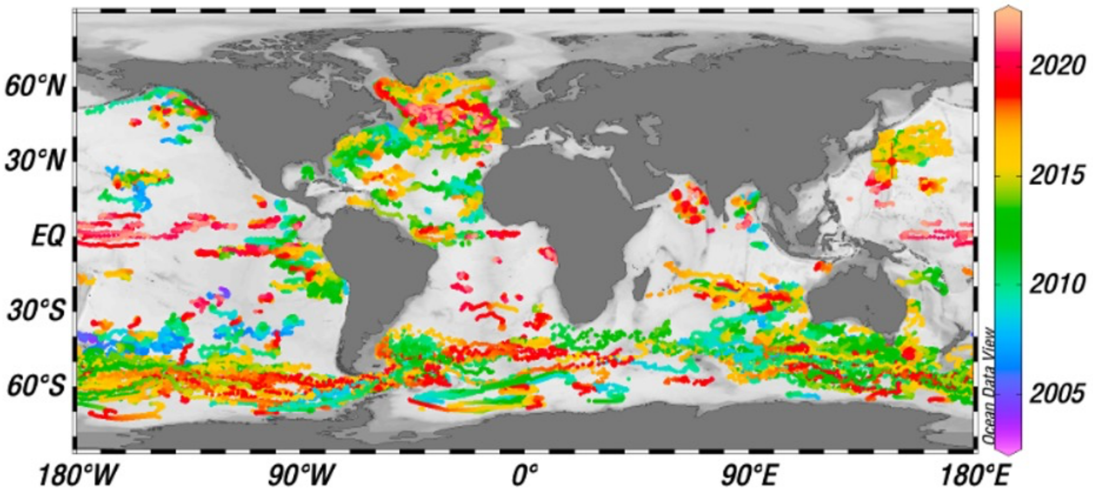

Fig. 5.3 Distribution of Bio-Argo profiles used in this study. Color bar indicates the date of each profile.

Fig. 5.4

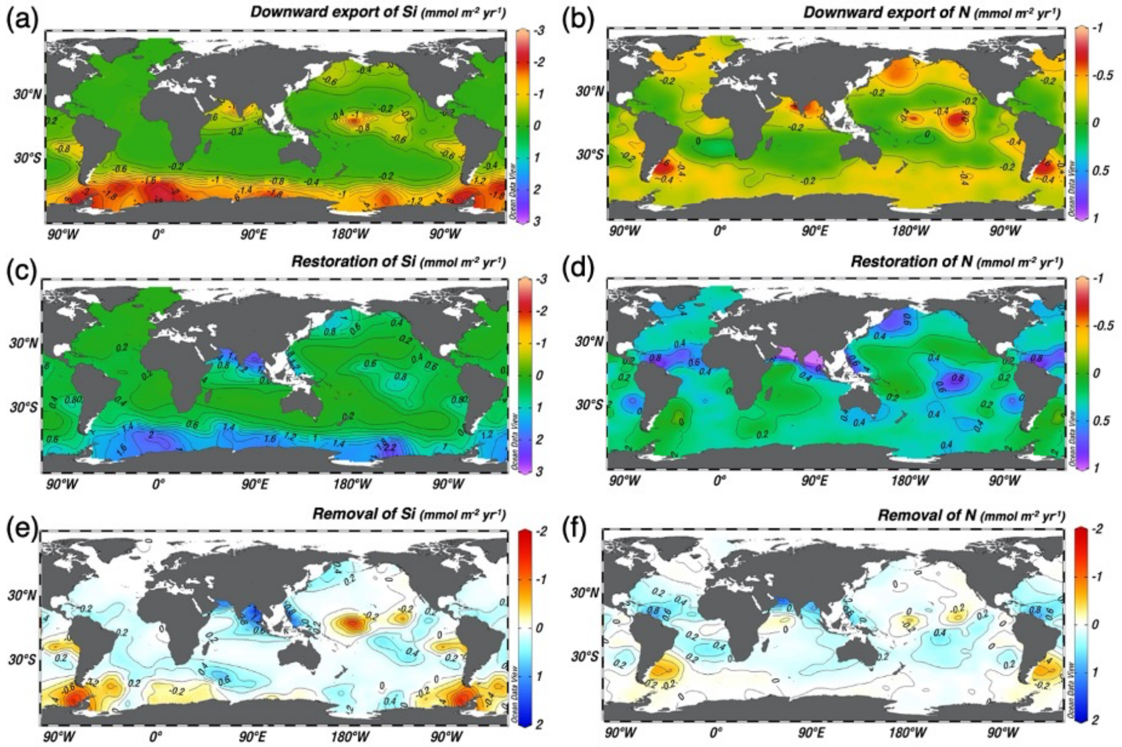

Fig. 5.4 Global distribution of Downward export of Si and N (a)&(b); Restoration of Si and N (c)&(d); Removal of Si and N (e)&(f).

Fig. 5.5

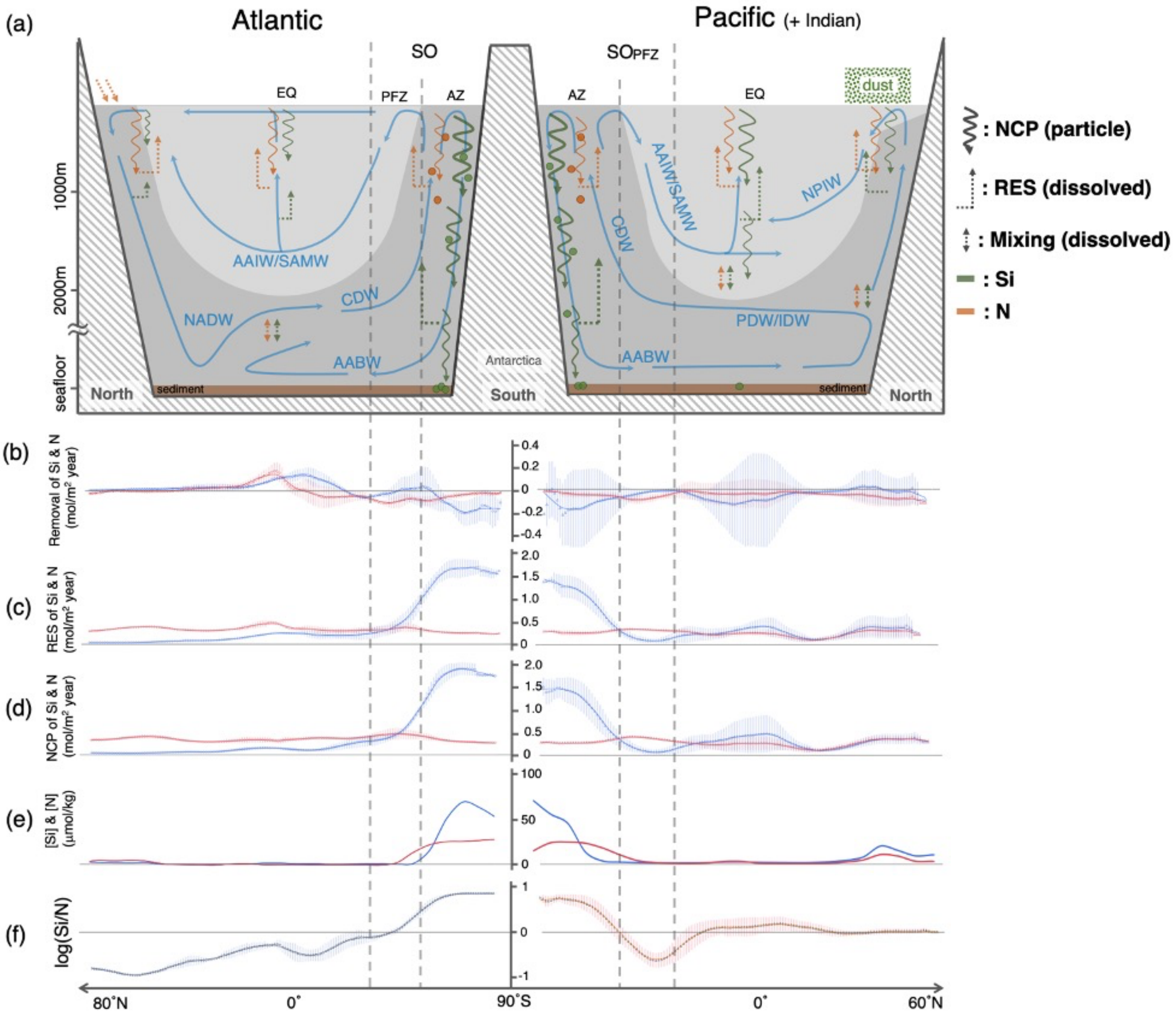

Fig. 5.5 (a)Schematic of meridional overturning circulation and nutrient cycles. (b)-(e) Average meridional distribution of removal, restoration, downward export and concentration of Si and N. Blue lines show Si and red lines show N. (f) Average meridional distribution of log (Si/N), where Si/N is the ratio of downward export of Si and N. Error bars show one standard deviation.